NAM

Impact of various modelling options on the onset of fault slip and the fault slip response using 2-dimensional Finite-Element modelling

P.A.J. van den Bogert

Datum August 2015

Editors Jan van Elk & Dirk Doornhof

General Introduction

The objective of this study was to develop a qualitative insight into the impact of various modelling parameters on the onset of fault slip and subsequent slip behavior, with the ambition to develop new seismological model hypotheses for testing against available and newly acquired seismic event data from the Groningen field.

This study addresses a limited number of modelling options, focusing on fault orientation and fault slip properties, as well as reservoir formation properties. A large number of sensitivities have been evaluated starting from a Base-case model that includes a single, straight fault with uniform properties, in a uniform linear-elastic subsurface. The following sensitivities have been investigated:

- elasticity parameters (Young's modulus and Poisson's ratio),
- in-situ stress orientation and magnitude,
- fault orientation and dip angle,
- reservoir thickness
- reservoir formation offset along the fault plane
- differential compaction

The results provide new insights into the relationship between various parameters that influence the onset of fault slip. In particular, it is found that offset of the depleting reservoir formation causes a distinctly different slip response after the onset of fault slip. The fault slip response of up-thrown blocks is distinctly different from down-thrown blocks, while also an offset smaller than the reservoir thickness causes a different slip response than formation offset larger than the reservoir thickness for down-thrown blocks.

The energy balance equation provides a framework to improved physical understanding of the partitioning factor using geomechanical concepts, which is a key factor in the current seismic hazard analysis approach for the Groningen field. The evaluation of the energy balance equation, which is new in petroleum geomechanics, reveals that fault slip and formation strain energy (compaction) are competing for the same energy source. This is the change of gravity energy of the subsurface and is determined by the subsidence of the overburden. This implies that energy is either dissipated by fault slip or stored as formation strain energy. It also implies that energy dissipated by fault slip is not available to radiate to the surface after a seismic event. Therefore, it is important that relevant energy storage and dissipation mechanisms are incorporated into a seismological model.

Furthermore, it is found that the conventional Mohr-circle approach to assess the stability of faults for petroleum industry applications does not provide a conservative estimate of the allowable reservoir pressure. This analytical method should therefore be replaced by an improved, yet pragmatic, approach based on the insights of this study.

NAM

Title	**Impact of various modelling options on the onset of fault slip and the fault slip reponse using 2-dimensional Finite-Element modelling**		**Date**	2015
			Initiator	NAM
Author(s)	P.A.J. van den Bogert	**Editors**	Jan van Elk Dirk Doornhof	
Organisation	Shell	**Organisation**	NAM	
Place in the Study and Data Acquisition Plan	Study Theme: Seismological Model Comment: Qualitative insight into the impact of various modelling parameters on the onset of fault slip and subsequent slip behaviour was investigated.			
Directliy linked research				
Used data				
Associated organisation	Shell			
Assurance	Internal Assurance only.			

Impact of various modelling options on the onset of fault slip and fault slip response using 2-dimensional Finite-Element modelling

Restricted

SR.15.11455

July 2015

Restricted **SR.15.11455**

Impact of various modelling options on the onset of fault slip and fault slip response using 2-dimensional Finite-Element modelling

by

P.A.J. van den Bogert (GSNL-PTU/E/Q)

Shell Global Solutions International B.V., Rijswijk

Further electronic copies can be obtained from the Global Information Centre.

Executive summary

The objective of this study is to develop a qualitative insight into the impact of various modelling parameters on the onset of fault slip and subsequent slip behaviour, with the ambition to develop new seismological model hypotheses for testing against available and newly acquired seismic event data from the Groningen field. Hypothesis testing in the Groningen field is hampered by the large uncertainty in hypocentre location of the seismic events, which is estimated between 500 and 1000 meter in the Groningen field. More accurate seismic event data is expected starting in 2015. Therefore, development of an explicit fault-based geomechanical model that can predict seismic event location with an acceptable level of confidence may proof hard to achieve in the near term.

This study addresses a limited number of modelling options, focussing on fault orientation and fault slip properties, as well as reservoir formation properties. A large number of sensitivities have been evaluated starting from a Base-case model that includes a single, straight fault with uniform properties, in a uniform linear-elastic subsurface. The following sensitivities have been investigated:

- elasticity parameters (Young's modulus and Poisson's ratio),
- in-situ stress orientation and magnitude,
- fault orientation and dip angle,
- reservoir thickness
- reservoir formation offset along the fault plane
- differential compaction

The results provide new insights into the relationship between various parameters that influence the onset of fault slip, beyond those presented in existing literature [3][5][6][7]. In particular, it is found that offset of the depleting reservoir formation causes a distinctly different slip response after the onset of fault slip. The fault slip response of up-thrown blocks is distinctly different from down-thrown blocks, while also an offset smaller than the reservoir thickness causes a different slip response than formation offset larger than the reservoir thickness for down-thrown blocks.

The energy balance equation provides a framework to improved physical understanding of the partitioning factor using geomechanical concepts, which is a key factor in the current seismic hazard analysis approach for the Groningen field [23]. The evaluation of the energy balance equation, which is new in petroleum geomechanics, reveals that fault slip and formation strain energy (compaction) are competing for the same energy source. This is the change of gravity energy of the subsurface and is determined by the subsidence of the overburden. This implies that energy is either dissipated by fault slip or stored as formation strain energy. It also implies that energy dissipated by fault slip is not available to radiate to the surface after a seismic event. Therefore, it is important that relevant energy storage and dissipation mechanisms are incorporated into a seismological model.

Furthermore, it is found that the conventional Mohr-circle approach to assess the stability of faults for petroleum industry applications does not provide a conservative estimate of the allowable reservoir pressure. This analytical method should therefore be replaced by an improved, yet pragmatic, approach based on the insights of this study.

Five hypotheses are articulated based on the results of this study. One is based on the onset of fault slip, two are based on the length and incremental length of the slip patch with reservoir depletion, one is based on the vulnerability of particular fault configurations to unstable (potentially seismogenic) fault slip, and one concerns the use of seismic event data to in relation to the stress path followed in the most critical point along the fault plane.

It is proposed to extend the current 2D static analysis approach to one that includes kinetic energy in a 2D dynamic rupture approach. The correlation of the seismic moment recorded in historical seismic event to one or more energy terms derived from geomechanical considerations seems most promising. For this purpose it is required to include kinetic energy into the energy balance equations.

Table of contents

List of Figures

List of Tables

1. Introduction

In an initial assessment [10], the reservoir depletion pressure required to trigger the onset of fault slip in the Groningen field has been estimated using an analytical approach and a triangulated description of 707 faults obtained from the available static model [18]. The approach was based on a Mohr-circle evaluation of the fault stress under virgin and depleted stress conditions. The virgin stress condition was obtained from available log data, LOT data, drilling information and experimental results (see [10] for details). The depleted stress condition was estimated using so-called stress-path coefficients. The fault stability under virgin and depleted stress condition was expressed by the Shear Capacity Utilisation (SCU) in a large number of points along the 707 faults. The SCU is the ratio between the actual shear stress in a point on the fault plane and the tolerable shear stress or shear stress capacity at that location. The results were compared with the available seismic event data, showing that faults with a large number of seismic events indeed have a high SCU. However, a large number of other fault locations with a high SCU, did not correspond with observed seismic events. Comparison between model results was hampered by the large uncertainty in hypocentre location of the seismic events, which was estimated between 500 and 1000 meter.

Previous work [3][5][6][7] has revealed that geometrical parameters and in particular the formation offset influences the onset of fault slip. Other work [14] has also found that stiffness contrast between reservoir and overburden is a key factor that discriminates fields with and without seismic events in the Netherlands. TNO [15] uses stiffness contrast as one of the parameters to assess the seismic hazard of individual fields in the Netherlands. This report addresses these aspects in an extensive sensitivity study. Besides the elastic formation parameters (Young's modulus and Poisson's ratio) and the formation offset across the fault, also in-situ stress, fault cohesion and friction angle, fault orientation (dip angle and dip azimuth) and reservoir formation thickness are considered.

To this end, a 2-dimensional model generator has been developed. A very fine-gridded 2D modelling environment has been chosen to capture the steep stress gradients along the fault plane, while restricting computer time. Dedicated software has been developed to efficiently run the large number of finite-element calculations and to conduct dedicated post-processing. The post-processing involves determination of the location of the onset of fault slip and the associated reservoir depletion pressure, the determination of the number, location and length of the slip patches as a function of depletion pressure as well as the so-called Relative Shear Displacement, and the dissipated energy by fault slip. Furthermore, additional output has been developed to evaluate the energy balance equation.

The main features of the developed 2D model generator are described in Chapter 2, including a description of the Base case. The geometrical parameters of the Base case and the in-situ stress condition are based on data from the Northern part of the Netherlands. The formation and fault properties have been selected in such a way that fault slip is triggered within the depletion range applied (0-30 MPa, 0-300 bar). Consequently, the reported values are not necessarily representative for the Groningen field conditions.

The aim of the current study is to develop a qualitative insight into the impact of various modelling parameters on the onset of fault slip and slip behaviour. Furthermore, it is the ambition to develop new seismological model hypotheses for testing against available and newly acquired seismic event data, in particular those from the Groningen field. However, this study addresses only a limited number of the known uncertainties, and new, more complex models will suffer from the same inaccuracy of available hypocentre locations. Therefore, a (more) positive comparison with current seismic data may proof hard to achieve. From a geomechanical modelling point view, this study assesses the performance of a number of modelling options by analysis of different response parameters, such as the Relative Shear Displacement and the

dissipated energy by fault slip. The objective is to determine which modelling options are important and which are not so important. Further study would be required in the spirit of David Wood's quote (below) as this study only addresses a limited number of modelling options. This implies that certain physical phenomena that are essential for the description of seismicity are not included in the current modelling. This study is regarded as a step towards the selection of the relevant geomechanical modelling options to contribute to an improved seismological model for the Groningen field, that leads to potential hypothesis for testing against available and newly acquired seismic data in further work.

The Base-case results are described in Chapter 3. The formation is evaluated for the stress and strain distributions before and after the onset of fault slip. The fault is evaluated in terms of the normal and shear stress distribution. The Relative Shear Displacement and the total length of the slip patches are given. Furthermore, the distribution of the released gravity energy over the various energy components is given. Furthermore, a comparison is made with the analytical solution used in the initial assessment [10].

In subsequent chapters, the impact of the elastic parameters on the onset of fault slip (Chapter 4) and on the energy distribution (Chapter 5) is discussed. Chapter 6 addresses the impact of in-situ stress and fault cohesion and friction angle on the onset of fault slip, while the influence of formation offset on the onset and on the slip response are extensively discussed in Chapter 7. In Chapter 8 and Chapter 9, the impact of reservoir formation thickness and fault orientation are covered. Finally, the main results are summarised and discussed in an integrated fashion in Chapter 10 followed by the conclusions and recommendations of this study in Chapter 11.

"A model is an appropriate simplification of reality. The skill in modelling is to spot the appropriate level of simplification to recognise those features which are important and those which are unimportant."

— *David Muir Wood*

2. Model description

A large number of sensitivity runs are presented in this report. This chapter described the Base-case model that is used as the reference model to discuss the impact of various modelling features on the simulated results. It is not intended to reflect any particular field condition. In section 2.2 the geometrical aspects of the Base case are described, in section 2.3 the in-situ stress and formation properties, and in section 2.4 the reservoir pore pressure under virgin and depleted conditions. First, the model features are discussed in Section 2.1.

2.1. Model features

A model generator has been built to evaluate the geometrical configuration outlined in Figure 2.1 using finite-element techniques. The configuration comprise of a dipping fault plane and 8 horizontal formation layers, 4 in the foot wall and 4 in the hanging wall. The shallowest Layer (1) on each side of the fault is considered the overburden, layers 2 and 3 are potential reservoir units that can be assigned a change of pore pressure, and the deepest Layer (4) is the under-burden. The thickness of each of the 8 formations can be specified independently. The vertical throw over the fault is defined by the difference in thickness of the overburden Layer (1) of the hanging wall and the foot wall. The True Vertical Depth of the surface and a surface load can be specified to simulate offshore conditions, if desired. Furthermore, the dip angle and dip azimuth γ_{dip} of the fault relative to North, as well as the maximum horizontal stress azimuth γ_{SHmax} is specified to install the desired initial stress orientation.

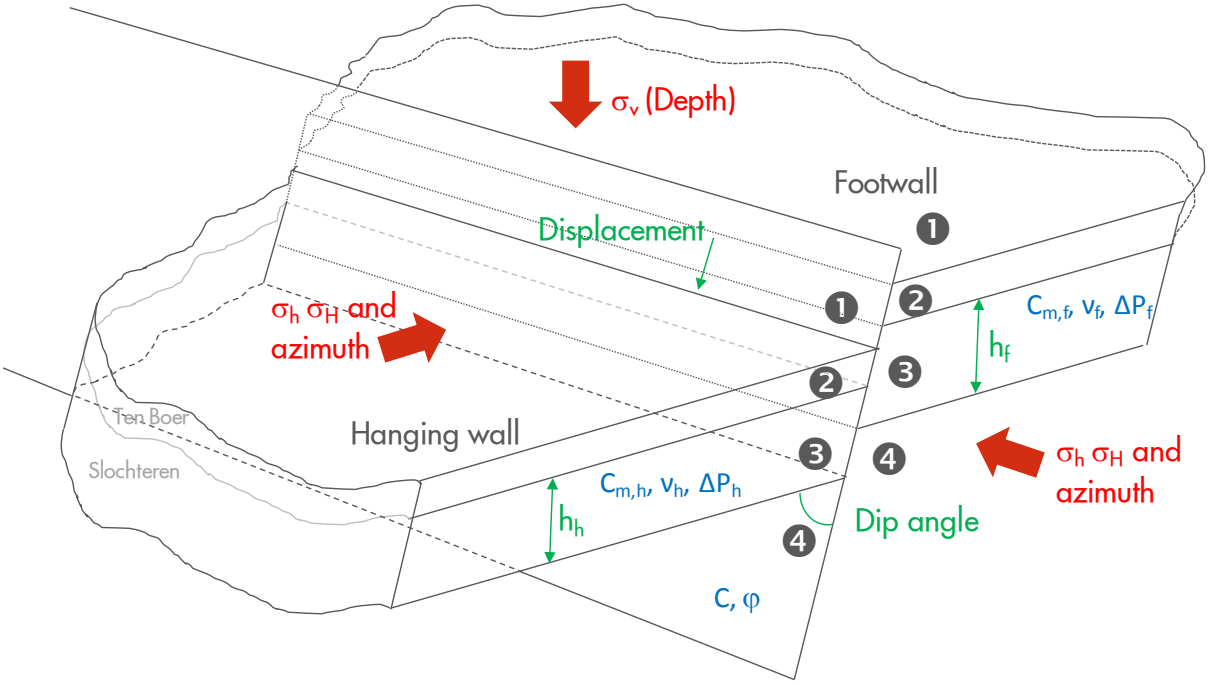

Figure 2.1: Outline of the model and its main parameters.

The material properties, in-situ stress and pore pressure can be specified for each of the 8 layers independently. The current model generator supports linear-elastic material behaviour, specified by Young's modulus and Poisson's ratio, but no poro-elastic behaviour. The total vertical stress is given by the density of each formation layer, whereas both horizontal total stress components are specified through as a multiplier (the so-called k_0 ratio) with the total vertical stress. The pore pressure is specified by a depth gradient from a given reference pressure and reference depth. An independent change of pore pressure can be specified to 4 formation layers, namely layers 2 and 3 on the hanging and foot wall side of the fault. This change of pore pressure is assumed to be uniform within the 4 formation layers. The pore pressure in the fault can be assigned equal to the

formation pore pressure at the left or right side of the fault. So, pressure communication is assumed between the formation and the fault, because this is the prevailing condition in the Groningen field.

The fault behaviour is described by a Mohr-Coulomb slip criterion, which is specified by a cohesion and friction angle. The post-failure behaviour is assumed "ideal plastic", which means that the shear stress carrying capacity of the fault remains constant after the onset of fault slip. A dilatancy angle is specified to describe the post-failure behaviour in the fault [22]. Further details of the model generator are provided in Appendix 1.

Fault slip behaviour is evaluated by a 2-dimenional (DIANA) plain strain finite-element model (Figure 2.2). One-dimensional interface elements simulate the behaviour of fault slip. The length of the interface elements is restricted to 1 m over the depleting layers 3 and 4 in order to calculate the development of critical stress conditions under the presence fault offset accurately. The size of the linear continuum elements next to the interface elements have a similar size and increase towards the boundaries of the model. The fault zone and the four formations on each side are recognised by the small element region in the middle of the model in Figure 2.2.

The top surface of the model has a zero stress boundary condition, while the normal displacements of the nodes along the two vertical sides and the bottom of the model are prohibited. The origin of the coordinate system is located in the middle of the top surface of the model, with the positive X-axis in horizontal direction to the right, and the positive Y-axis in vertical direction upwards. Hence, subsurface depth is negative. Furthermore, positive stress and strain correspond with elongation. Thus, compressive stress are negative in this report, unless otherwise stated.

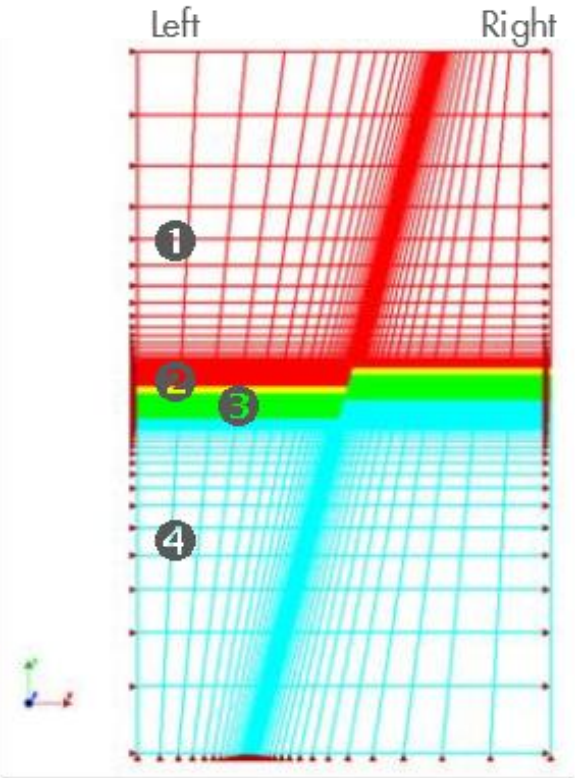

Figure 2.2: Example a generated finite-element mesh with a down-thrown (positive offset) reservoir formation on the left-hand side of the fault.

2.2. Base-case geometry

The analysis results reported in this study have been obtained from a model with a total width of 2000 m and the depth between 0 and 6000 m. The layering is based on the Groningen field, with Layer 2 in the model (Figure 2.3) representing the Z1 formation (ZEZ1) of the Permian Zechstein Group that consists of very stiff anhydrites and carbonates and are Layer 3 representing the depletion in the Ten Boer Member (ROCLT) and Slochteren Formation (ROSL). All overburden formations are represented by Layer 1 and all under-burden formations are captured in Layer 4. The thickness of each formation represents an average thickness derived from the Groningen subsurface model [18].

The impact of the formation offset, and other complexities are addressed in dedicated sensitivity studies and therefore not included in the Base-case. Table 2.1 summarises the numerical values of the Base-case geometrical parameters. The fault dip azimuth angle is taken 90 degrees with the maximum horizontal stress azimuth (see next section). This implies that the Base-case fault is exposed to the minimum horizontal stress.

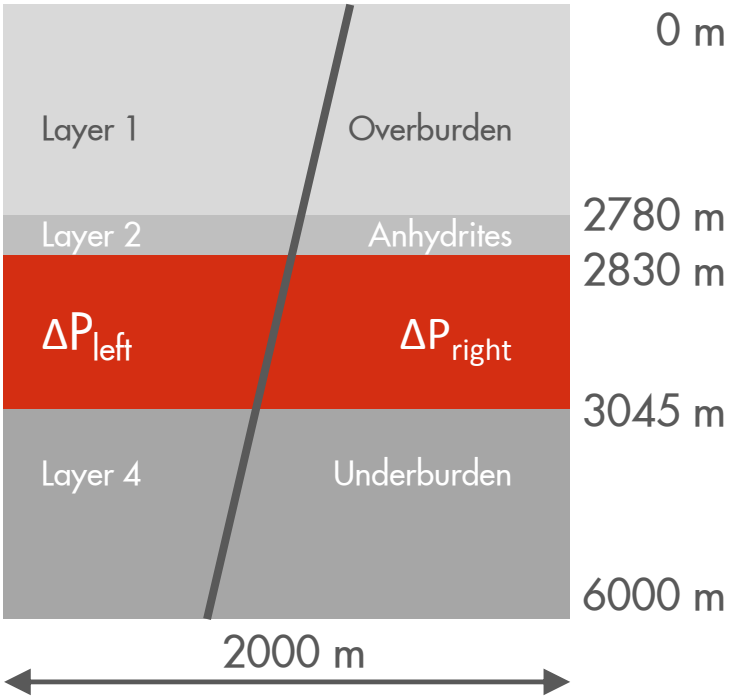

Figure 2.3: **Base-case model geometry (not to scale), in which Layer 3 represents the depletion on the Ten Boer and Slochteren formations.**

Table 2.1: **Formation thickness, offset and fault orientation along for the Base case.**

	Unit	Value
ZEZ1 depth	[m]	2780
ZEZ1 thickness	[m]	50
ROCLT & ROSL thickness	[m]	215
Formation offset	[m]	0
Fault dip with horizontal	[deg]	65
Fault dip azimuth North to East	[deg]	70 (250)

2.3. Base-case in-situ stress and formation properties

The in-situ stress has been taken from Van den Bogert and Van Eijs [10] and is summarised in Table 2.2, with the notification that these values are expected to change by onging field data analysis. The total vertical stress gradient has been converted into a formation density to facilitate incorporation into the 2D model. Furthermore, the two horizontal stress gradients have been converted into a maximum and minimum total horizontal stress ratio to the total vertical stress (k0-max and k0-min respectively). The azimuth angle of the maximum horizontal stress is 160 degrees from North to East. The results of the conversion are given in Table 2.3.

Table 2.2: Virgin in-situ stress condition at 2875 m TVD and Coulomb friction constants used for base-case stability evaluation of the geological faults.

Parameter	Gradient [bar/10m]	Pressure [bar]
Vertical stress	2.14	615
Min. Horizontal stress	1.60	460
Max. Horizontal stress	1.71	491
Max./Min. horizontal stress ratio	1.07	[-]
Max. horizontal stress azimuth	160	[deg]
Pore pressure (gas density)	0.18	350

Table 2.3: Density, horizontal in-situ stress condition and linear-elastic formation properties.

	Density	K_0-max	K_0-min	Young's modulus	Poisson's ratio
Unit	[kg/m3]	[-]	[-]	[GPa]	[-]
Layer 1 – Overburden	2172	0.795	0.748	10.	0.25
Layer 2 – ZEZ1	2450	0.795	0.748	10.	0.25
Layer 3 – ROCLT & ROSL	2450	0.795	0.748	10.	0.25
Layer 4 – Underburden	2700	0.795	0.748	10.	0.25

Identical values for Young's modulus and Poisson's ratio have been used for all model layers to remove any influence of these parameters on the stress and strain evolution along the fault plane and the onset of fault slip in the Base case. The impact of stiffness contrasts and the vertical and horizontal in-situ stress magnitudes are addressed in dedicated sections of this report.

2.4. Base-case pore pressure and reservoir depletion conditions

The initial pore pressure in the overburden Layer 1 is taken hydrostatically with a pressure gradient of 10 kPa/m (1.0 bar/10m). This is shown in Figure 2.4. Also, Layer 2 has been assigned this initial pore pressure gradient. The more saline aquifer in the under-burden Layer 4 has been given a somewhat elevated pressure gradient at 11.66 kPa/m. In reservoir Layer 3 a gas density of 1.8 g/cm^3 has been attained. Furthermore, the Gas-Water Contact has been set at 2995 m TVD at a pressure 35.2 MPa (352 bar). This pressure point has been used to construct the pressure-depth relationship in Layers 3 and 4 shown in Figure 2.4.

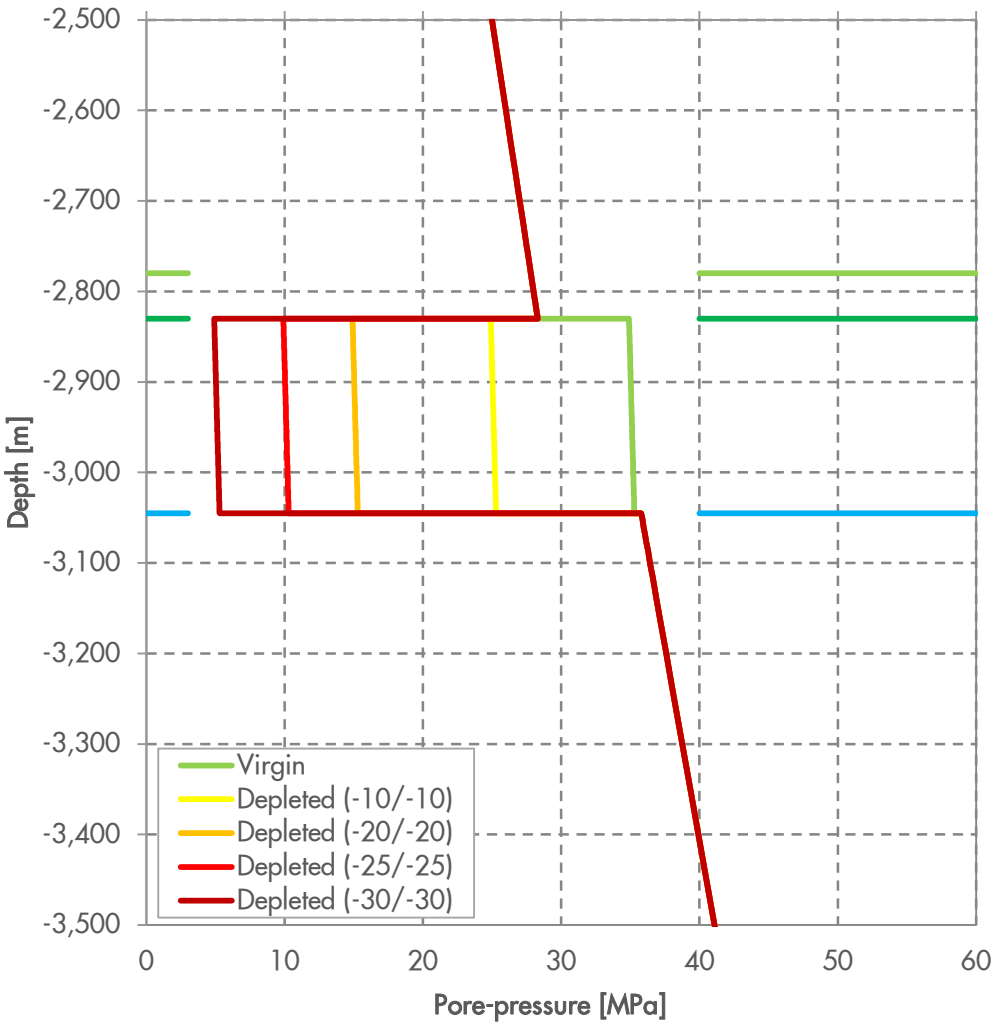

Figure 2.4: **The virgin pore pressure (MPa, green line) and the pressure after 10, 20, 25 and 30 MPa depletion as a function of depth (m TVD). The six horizontal lines indicate the depth of the interface between layers 1, 2, 3 and 4 on the left- and right-hand side of the fault.**

Uniform reservoir depletion has been simulated by lowering the pore pressure in formation Layer 3 on both sides of the fault. That is, the fault has been assumed to transmit and to equilibrate any pressure difference that might occur in the course of production. The pore pressure in the fault follows the depletion along those parts that is in contact with a depleting layer and maintains the virgin pressure in all other parts. Depletion is increased in steps of 1 MPa (10 bar) for all calculations in this report. The red line in Figure 2.4 represents a pressure change of -30 MPa (depletion) in reservoir Layer 3. No pressure depletion is prescribed in any of the other formation layers.

2.5. Base-case fault properties

The model described in section 2.1 features a Mohr-Coulomb friction law with ideal plasticity in the interface elements that simulate the fault slip behaviour [10]. The slip condition of a particular interface element is expressed by the Shear Capacity Utilisation (SCU), which is defined by

$$SCU = \frac{\tau}{\tau_{\max}} = \frac{\tau}{C + \sigma_n \tan\varphi}. \qquad (2.1)$$

Herein, σ_n is the local normal effective stress component, τ is the resultant shear stress component of the interface element, C is the cohesion and φ the friction angle representative for the fault plane. An interface element is not slipping if SCU<1, while SCU=1 indicates an interface element that has reached the shear stress carrying capacity τ_{max}. SCU>1 cannot occur. Any shear stress in excess of the local carrying capacity τ_{max} is re-distributed over neighbouring interface elements under the development of a so-called Relative Shear Displacement (RSD). The RSD expresses the displacement of one side of the element relative the other side along the interface [5]. The ideal plasticity assumption implies that the shear stress carrying capacity τ_{max} of the interface elements remains constant with increasing Relative Shear Displacement.

In the Base case, cohesion and friction angle for the interface elements that describe the fault behaviour is set to 7 MPa and 13 degrees respectively. These values have been used in a previous study [10] to ensure that onset of fault slip is simulated at a realistic reservoir depletion pressure in a wide range of values of the Poisson's ratio. The Poisson's ratio ν strongly influences the change of the horizontal stress in uniaxial compaction condition due to reservoir depletion [10]. The impact of cohesion and friction angle is addressed in dedicated sections of this report.

2.6. Finite-element model evaluations

The following aspects have been evaluated as a function of reservoir depletion for all cases in this study

- maximum Shear Capacity Utilisation (SCU) along the fault plane
- depletion pressure at the onset of fault slip
- number of slip patches
- total length of the slip patches
- maximum Relative Shear Displacement (RSD) along the fault plane

The SCU distribution along the fault plane is evaluated to find interface elements with SCU=1 after each depletion pressure increment of 1 MPa. Onset of fault slip is defined as the depletion level at which SCU=1 for at least one interface element. A slip patch is defined as a un-interupted section of the fault for which SCU=1. The length of the slip patch is calculated from the sum of the length of the interface elements with SCU=1. For all cases reported, also the number of slip patches is determined with increasing depletion level. Also, the RSD distribution along the fault plane and its maximum value is extracted from the calculation results.

Furthermore, the energy balance equation is evaluated as a function of reservoir depletion, with the objective to understand the relationship between different forms of energy in the modelled system. The DIANA finite-element model described in section 2.1 comprise of two constituent parts, namely the 2D continuum elements representing the formations and the 1D interface elements representing the fault. The energy of the continuum elements is decomposed into the strain energy W_ε of the porous medium and energy of the pore (fluid) system W_p. The energy of the fault is decomposed into energy related to normal and shear deformation of the interface elements, W_n and W_s respectively. The continuum elements (formations) also have gravity energy. As a result, five energy terms are distinguished in the current 2-dimentional model, namely

1. formation strain energy W_ε,
2. formation pore pressure energy W_p,
3. fault shear strain energy W_s,
4. fault pore pressure energy W_n,
5. gravity energy W_g.

In the current 2D model, energy is added to the modelled system through the labour performed by external (boundary) forces. However, no external forces are prescribed, and the energy change of the modelled system is zero, so that:

$$W_\varepsilon + W_p + W_s + W_n + W_g = 0 \tag{2.2}$$

In DIANA, the formation strain energy for continuum elements is defined as:

$$W_\varepsilon = \frac{1}{2}\int_V (\sigma + \sigma_0)\varepsilon \, dV \tag{2.3}$$

Where σ is the effective stress tensor and σ_0 is the effective stress tensor in the reference situation and ε is the strain tensor relative to the references situation. The product of stress and strain is integrated over the model domain V. The reference situation is the situation before depletion and incorporates the initial in-situ stress condition.

The formation pore pressure energy for continuum elements is defined as:

$$W_p = \frac{1}{2}\int_V (p + p_0)\varepsilon_{vol} \, dV \tag{2.4}$$

Where p is the pore pressure and p_0 is the pore pressure in the reference situation and ε_{vol} is the volumetric strain relative to the reference situation. The product of pressure and volumetric strain is integrated over the model domain V.

The fault shear strain energy for interface elements is defined as:

$$W_s = \frac{1}{2}\int_A (\sigma + \sigma_0)du \, dA \tag{2.5}$$

Where σ and σ_0 is the effective traction stress in the interface elements in the actual and reference situation respectively, and du is the relative normal displacement in the interface in the normal direction relative to the reference situation. The product of stress and displacement is integrated over the fault surface A.

The fault pore pressure energy for interface elements is defined as:

$$W_n = \frac{1}{2}\int_A (p + p_0)du^n \, dA \tag{2.6}$$

Where p is the pore pressure and p_0 is the pore pressure in the reference situation and du^n is the interface opening relative to the reference situation. The product of pressure and interface opening is integrated over the fault surface A.

A force field, such as gravity, performs labour if mass is moving through it. The energy related to gravity is defined as:

$$Wg = -\int_V \rho \, g du \, dV \tag{2.7}$$

Where ρ is the density of the formations and g is the gravity acceleration vector and du is the displacement vector relative to the reference situation. The product of density, gravity acceleration and displacement is integrated over the model domain V. Interface elements do not contribute to the gravity energy, because they do not have mass.

In the current model the formation strain energy is an elastic, recoverable energy component. The formation pore pressure energy is calculated from the pore pressure and pore volume compressibility. Fault strain energy is the labour performed by shear stress along the fault plane and is irrecoverable after the onset of fault slip. The fault is also assigned a pore pressure that can

store energy as a result of displacements of the formations on both sides normal to the fault plane. The prescribed pore pressure change in the reservoir formations induces a change of formation pore pressure energy. The modelled system responds with a change of the other four energy components to satisfy equation 2.2. The relationship between energy terms and various modelling parameters is investigated in this study.

Finally, it is noted that negative stress and strain values represents a compression condition. Effective stress is discussed in the remainder of this report unless stated otherwise.

2.7. Analytical approach

In previous studies [10][17], the onset of fault slip has been assessed based on an evaluation of the Mohr circle under virgin and reservoir depletion conditions. This analytical approach assumes so-called stress-path coefficients γ_i to estimate the three principal total stress components under depleted reservoir conditions. In this approach the change of the total principal stress ΔS_i is proportional to the change of pore pressure ΔP_p at any particular location in the subsurface:

$$\Delta S_i = \gamma_i \Delta P_p , \tag{2.8}$$

Herein, the subscript "i" denotes any of the principal stress directions (1, 2 or 3). Typically, these coincide with the vertical, the minimum and maximum horizontal stress directions. For uni-axial compaction conditions it can be derived [5][10] that the two horizontal stress stress-path coefficient γ_h relates to Poisson's ratio ν according to

$$\gamma_h = \alpha\left(\frac{1-2\nu}{1-\nu}\right). \tag{2.9}$$

Herein, the Biot constant α is introduced that is assumed to be 1 for the remainder of this study.

The vertical stress-path coefficient γ_v is assumed zero for uni-axial compaction conditions. That is, the total overburden stress σ_v is not changing due to reservoir depletion.

The total stress condition under depleted reservoir conditions is derived from the virgin in-situ stress as discussed in previous sections of this chapter, and the stress-path coefficients.

Subsequently, the effective normal and resultant shear stress components σ_n and τ respectively on a fault with given orientation to calculated the SCU according to equation 2.1 [10]. The finite-element results are compared to this analytical approach in a number of sections of this report.

The influence of Poisson's ratio ν on the onset of fault slip is explained from the change of the horizontal effective stress $\Delta\sigma_h$ under uni-axial compaction condition, which reads [5] :

$$\Delta\sigma_h = \frac{\nu}{1-\nu}\Delta\sigma_v . \tag{2.10}$$

Herein, $\Delta\sigma_v$ is the change of the vertical effective stress and is assumed to be equal to the change of the reservoir pressure.

3. Base-Case results

The fault slip response and the stress and strain development in the depleting reservoir layer are discussed for the Base case described in Chapter 2. The results are the starting point for the sensitivity studies presented in subsequent chapters. This chapter features the finite-element results in section 3.1 as well as the analytical results in section 3.2.

The key features of the Base-case model are the uniform linear-elastic formation properties (Young's modulus is 10 GPa and Poisson's ration is 0.25) and no formation offset across the fault. The fault plane is exposed to the minimum horizontal stress, i.e. the fault dip azimuth is 90 degrees with the maximum horizontal stress, and therefore provides the most critical orientation for the onset of fault slip. Other parameters worth highlighting are the reservoir formation thickness of 215 m, and the fault dip angle of 65 degrees with the horizontal. See Chapter 2 for the full description.

3.1. Finite-Element results

3.1.1. Formation stress and strain distribution

Figure 3.1 shows the vertical and horizontal effective stress distributions as well as the vertical compaction strain under 30 MPa (300 bar) reservoir depletion. The depleting reservoir formation is clearly recognised by the effective stress level that is higher compared to the over- and underburden. The fault is indicated by the grey diagonal line and shows discontinuities in the stress and strain components between the "Hanging wall" and "Foot wall". Furthermore, three horizontal lines are drawn close to the top, centre and bottom of the reservoir formation, which are used in the Figure 3.2 and Figure 3.3. The "Top" is 1 m below the top and the "Bottom" is 1 m above the bottom of the depleting reservoir formation, whereas the "Centre" is located at 2875 m TVD to allow comparison with the results of the analytical approach.

The vertical and horizontal effective stress distribution is shown in Figure 3.2 as a function of the horizontal coordinate at the top, centre and bottom of the reservoir formation for different depletion levels. Up to about 20 MPa depletion, the stress distribution is uniform across the reservoir. The vertical effective stress increases with the same magnitude as the reduction of the reservoir pressure (Biot's constant α =1). Onset of slip occurs at 19.9 MPa reservoir depletion, and causes a disturbance of the uniform stress distribution in the vicinity of the fault. It is seen that the vertical stress in the reservoir at the top-left and bottom-right side of the fault remains virtually constant after the onset of slip. This is caused by the ideal plasticity model assumed in the interface elements that does not include a softening response after the onset of fault slip.

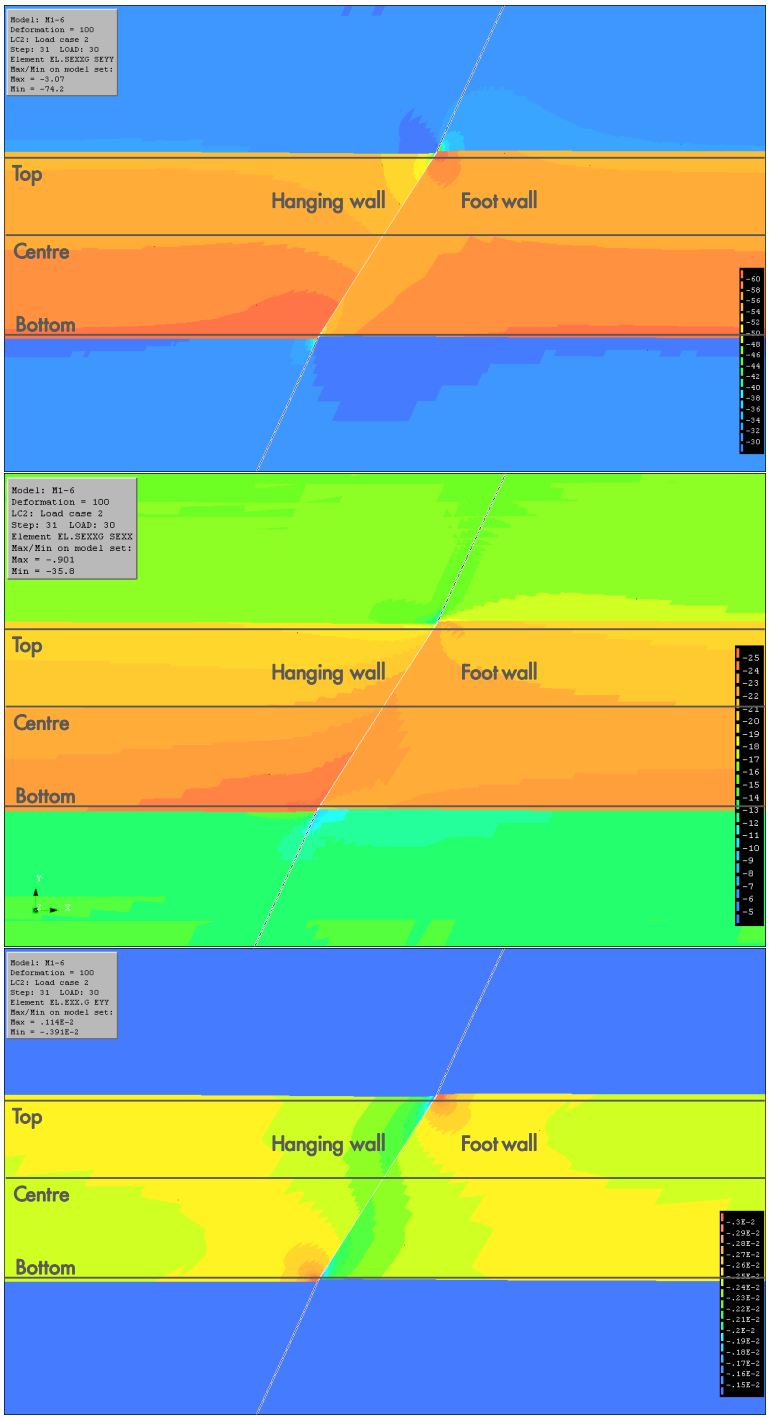

Figure 3.1: **Vertical and horizontal effective stress (top and middle respectively), and the vertical (compaction) strain (bottom) under 30 MPa depletion and a fault dip of 65 degree plotted in the deformed model. A part of the model is shown, with colour scale ranges between -30 (blue) and -60 MPa (red) for the vertical effective stress, between -5 (blue) and -25 MPa (red) for the horizontal effective stress, and between -0.15% (blue) and -0.30% (red) for the vertical strain.**

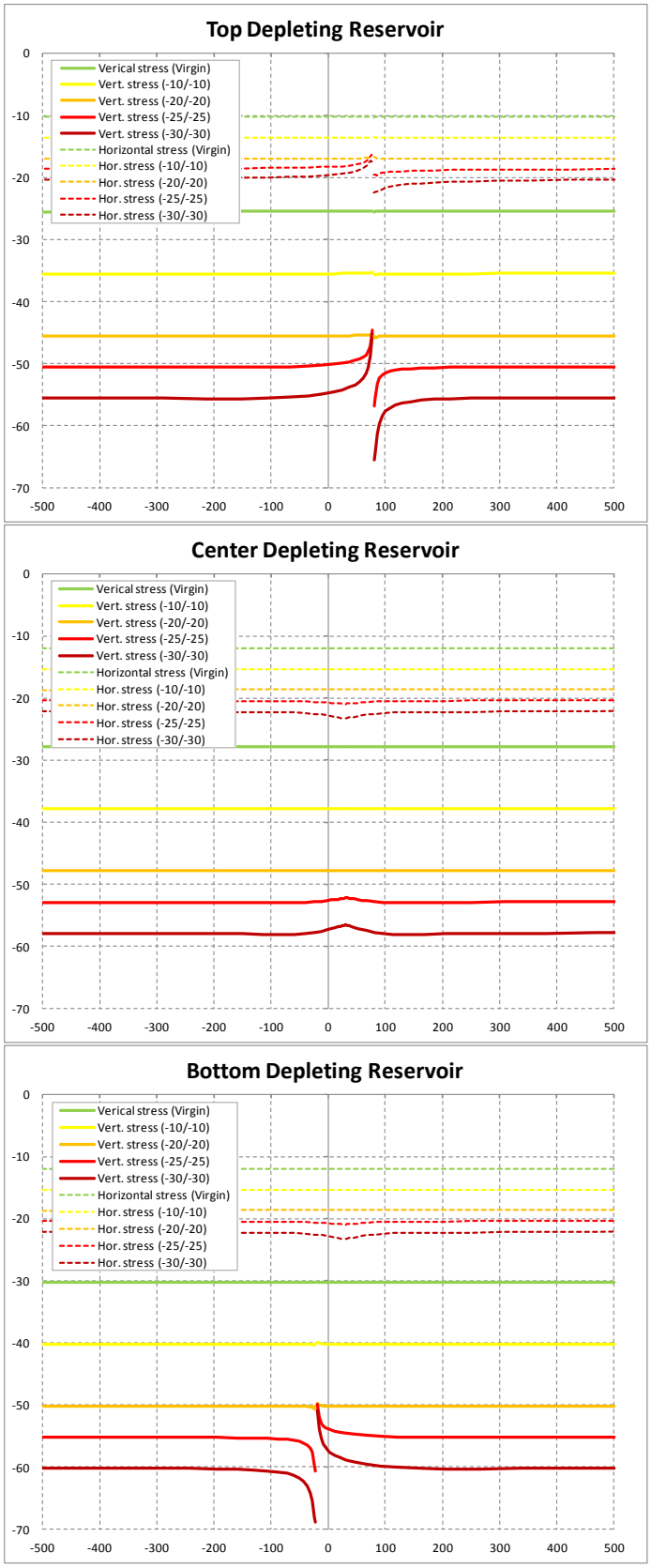

Figure 3.2: **Vertical (solid lines) and horizontal stress distribution (dashed lines) as a function of the horizontal coordinate at the top, centre and bottom of the reservoir under virgin, 10, 20, 25 and 30 MPa reservoir depletion. Compression is negative.**

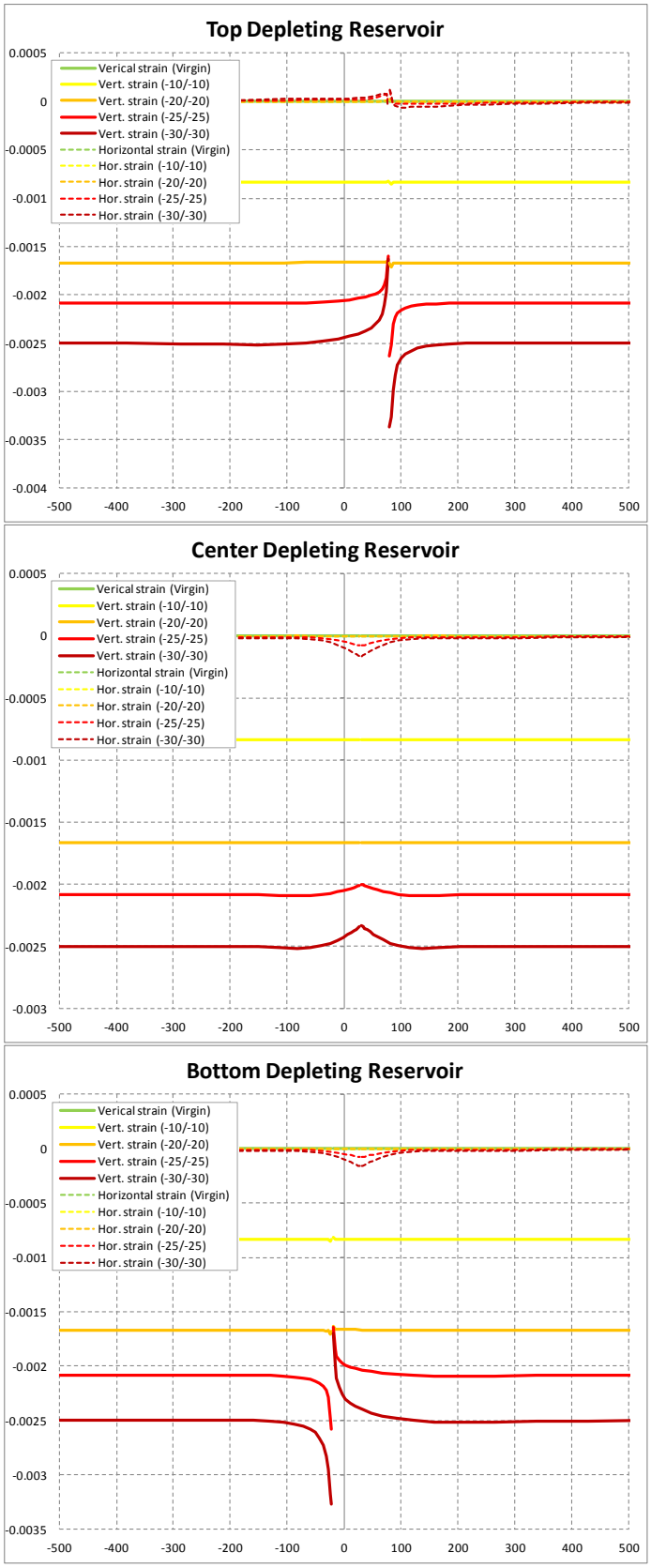

Figure 3.3: **Vertical (solid lines) and horizontal strain distribution (dashed lines) as a function of the horizontal coordinate at the top, centre and bottom of the reservoir under virgin, 10, 20, 25 and 30 MPa reservoir depletion. Compaction is negative.**

The vertical strain is uni-axial and can be calculated from the increase of vertical effective stress $\Delta\sigma_v$ relative to the virgin conditions, Young's modulus E and Poisson's ratio ν according to

$$\Delta\varepsilon_v = \frac{(1+\nu)(1-2\nu)}{(1-\nu)}\frac{\Delta\sigma_v}{E}. \tag{3.1}$$

Table 3.1 shows the uniaxial compaction strain values for different depletion levels and the linear-elastic model parameters applicable in the Base case. It is found that the finite-element results in Figure 3.3 correspond to the uniaxial compaction strain values at sufficient distance from the fault, where the stress and strain distribution is undisturbed by fault slip. Close to the fault, a significant deviation from the uniaxial compaction strain is developed. This deviation can be up to 40% more or less than the uniaxial compaction strain given in Table 3.1. Finally, it is noticed that the disturbed zone in horizontal direction is less than the reservoir thickness. This is similar to finding by TNO [21].

Table 3.1: Uni-axial compaction strain calculated using equation (3.1) for different depletion levels and a Young's modulus of 10 GPa a Poisson's ratio of 0.25.

Depletion	$\Delta\varepsilon_v$
10 MPa	$0.83\cdot10^{-3}$
20 MPa	$1.7\cdot10^{-3}$
25 MPa	$2.1\cdot10^{-3}$
30 MPa	$2.5\cdot10^{-3}$

3.1.2. Fault stress and Relative Shear Displacement (RSD)

Figure 3.4a shows the applied pressure profile as a function of depth for 10, 20, 25 and 30 MPa (100, 200, 250 and 300 bar) reservoir depletions. The location of the interfaces between formation layers 1, 2, 3 and 4 on both sides of the fault are indicated by horizontal (green and blue) marker lines (see also Table 2.1). The gas gradient in the reservoir formations is recognisable steeper than the water gradients in over- and under-burden.

Figure 3.4b shows the Relative Shear Displacement (RSD) along the fault plane as a function of depth for the same depletion levels. Negative values indicate that the left-hand side of the fault (the hanging wall) is displaced downwards relative to the right-hand side (foot wall) of the fault. A maximum RSD of 0.079 meter is calculated under 30 MPa depletion, whereas the slip is negligible for a depletion level up to 20 MPa.

Figure 3.4c shows the effective normal and shear stress distribution and Figure 3.4d shows the derived Shear Capacity Utilisation (SCU) as a function of depth. This is the ratio of the actual shear stress τ and the shear stress carrying capacity τ_{max} according to a Coulomb friction law (see section 2.5). A SCU of 1 means that the maximum shear stress has reached and that the fault is slipping. Values larger than 1 are not possible. The total length of the interface elements for which SCU=1 is defined as the slip patch. One slip patch over the entire height of the reservoir formation is created after the onset of slip at 19.9 MPa reservoir depletion. It is seen that the slip patch grows only marginally upon further reservoir depletion.

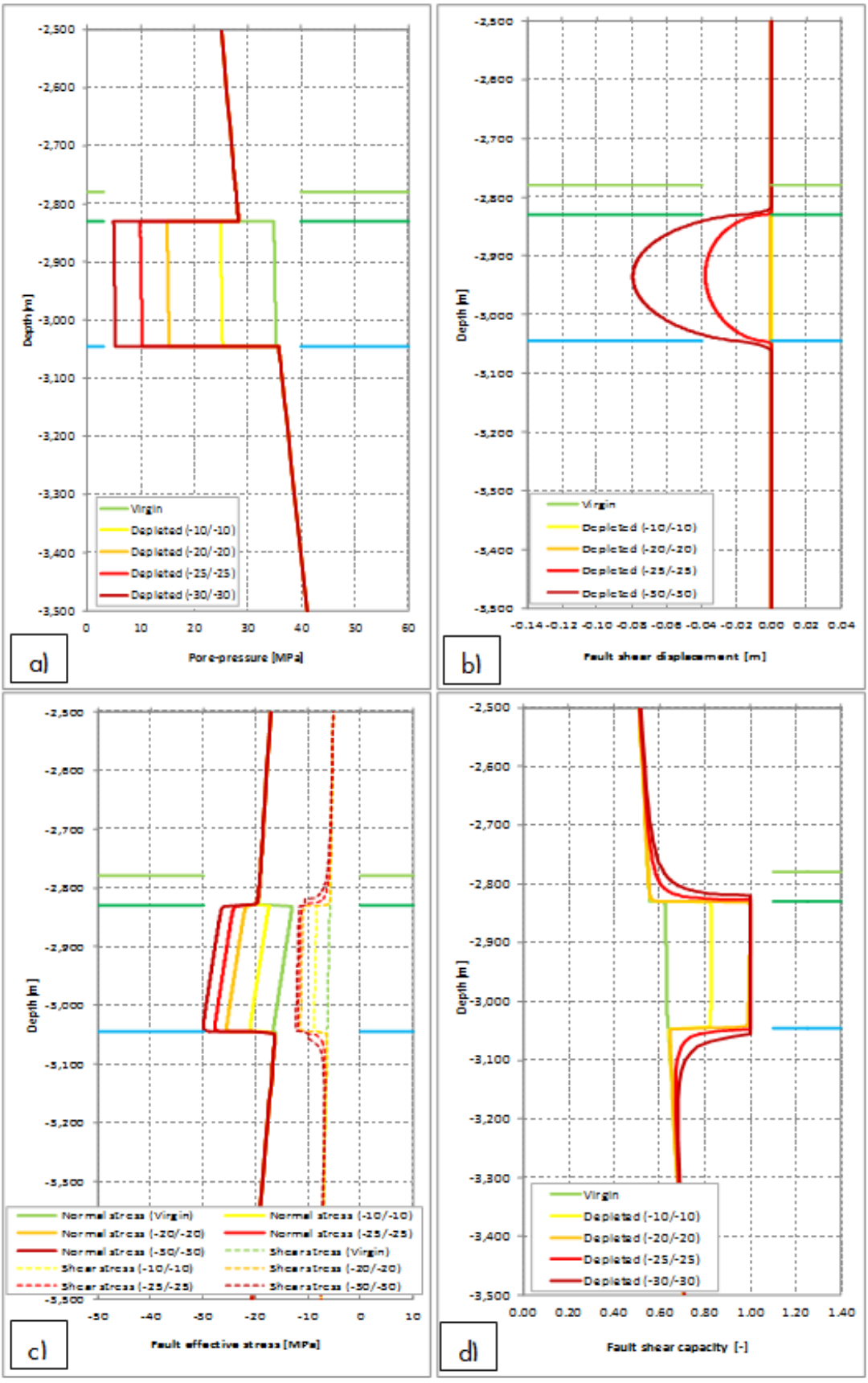

Figure 3.4: **a) Pore pressure, b) Relative Shear Displacement (RSD), c) Effective normal and shear stress, and d) the Shear Capacity Utilisation as a function of the depth, under virgin and 10, 20, 25 and 30 MPa depletion conditions.**

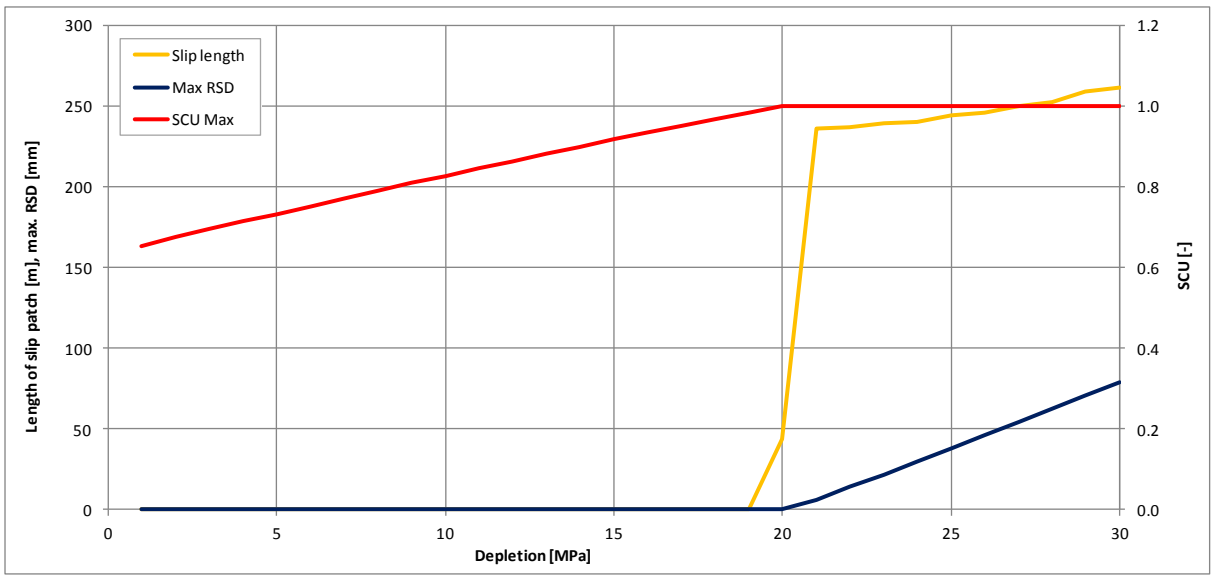

Figure 3.5: The length of the slip patch, the maximum Relative Shear Displacement (RSD) and the maximum Shear Capacity Utilisation (SCU) as a function of reservoir depletion

The onset of fault slip occurs if the maximum Shear Capacity Utilisation (SCU) along the fault plane reached the value 1, which is calculated at 19.9 MPa (red line in Figure 3.5). The development of the slip patch length with increasing reservoir depletion is shown by the yellow line (with depletion increments of 1 MPa). It is seen that the slip patch develops rather quickly after the onset of fault slip to 236 m at 21 MPa reservoir depletion, which is 10% more than the reservoir thickness of 215 m. Upon further depletion, a limited growth is seen to 261 m at 30 MPa reservoir depletion. After the onset of fault slip, the maximum Relative Shear Displacement (RSD) increases gradually with depletion up to 0.079 m at 30 MPa depletion.

3.1.3. Energy considerations

The five terms of the energy balance equation 2.2 are plotted as a function of reservoir depletion in Figure 3.6. The absolute values of the energy terms are shown as well as the fractions relative to the release of gravity energy. The release of gravity energy in the model $\Delta E_{potential}$ in the Base-case model is shown as positive value by the dark blue line. The linear increase is caused by the employed linear-elasticity theory for the reservoir formations and the uniaxial compaction response discussed in section 3.1.1 (equation 3.1). The lines with markers represent the fault energy terms, the green lines represent the strain energy and the blue lines the pressure terms. The following observations can be made from Figure 3.6:

- The energy terms for formation stress and formation pressure are of the same order of magnitude
- The fault energy terms are 3 orders of magnitudes smaller than the formation energy terms for the current 2-dimensional model
- The fault strain energy remains negligible up to the onset of fault slip at 19.9 MPa depletion, and absorbs less than 0.001 part of the change of gravity energy at 30 MPa reservoir depletion
- The fault pressure energy is negligible for all depletion levels

It is emphasised that the change of gravity energy is proportional with the volume of the depleting reservoir, and therefore proportional with the height and width of the reservoir

formation in the 2-D model. This implies that the energy fraction of the fault is dependent on the model dimensions.

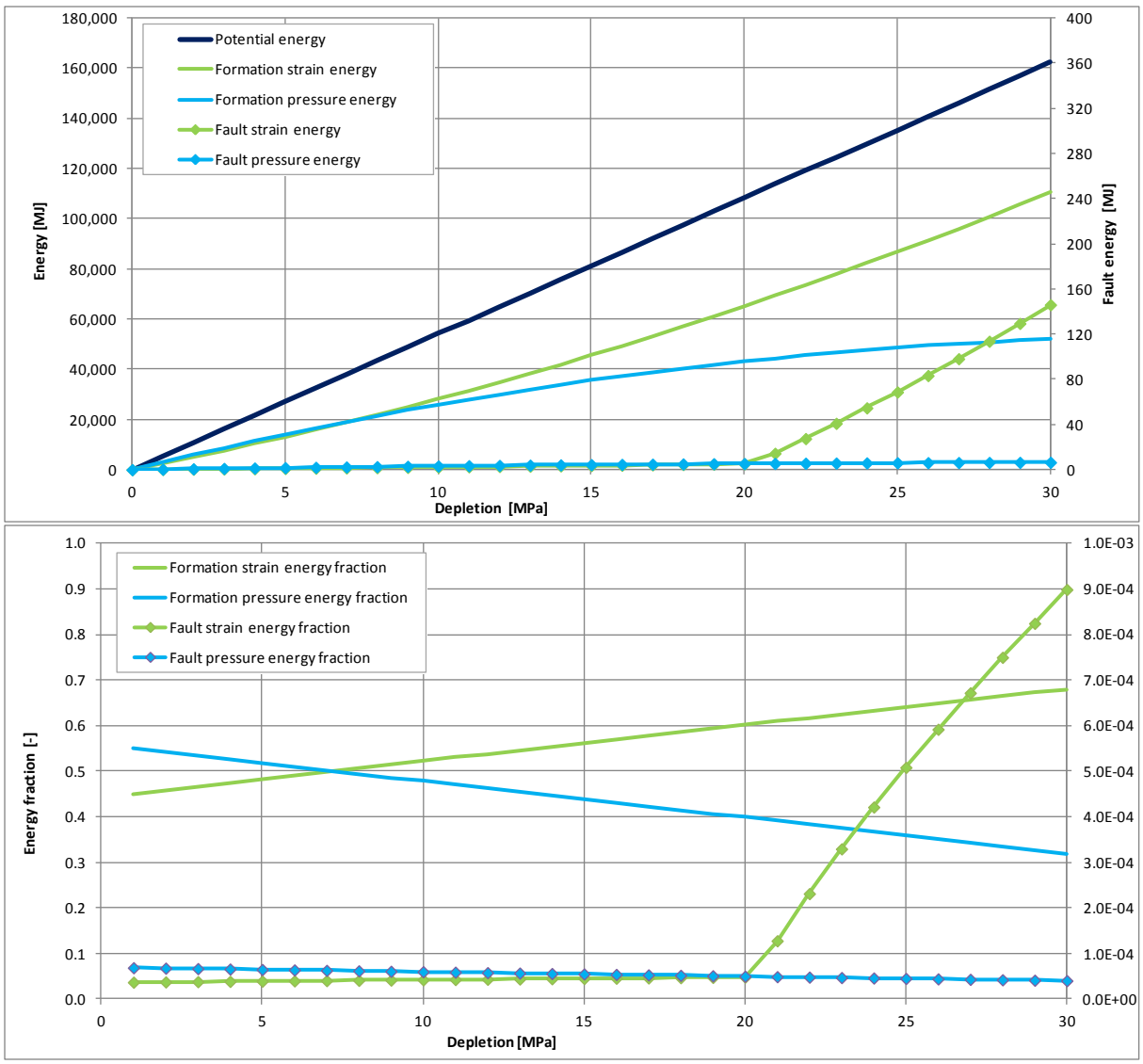

Figure 3.6: Total energy (top) and energy fractions (bottom) as a function of reservoir depletion. The formation energy terms are plotted on the left-hand scale, and the fault energy terms on the right-hand scale.

3.2. Analytical solution

For the Base case, the onset of fault slip can also be calculated analytically. The method is outlined in section 2.7, and described in detail in [10].

Figure 3.7 shows the Mohr-circle under virgin and 19.9 MPa reservoir depletion conditions. The applicable Base-case assumptions are given in the graph. For the virgin stress condition only the largest, most critical Mohr-circle is given. The three purple circles represent the stress condition under depleted reservoir conditions:

1. The smallest circle between the minimum and the maximum horizontal stress
2. The largest circle between the minimum horizontal stress and the vertical stress
3. The intermediate circle between the maximum and the vertical stress

The stress condition on a fault plane with 65 degree dip and 70 degree azimuth angle is represented by the two points. The green point represents the virgin stress condition and the purple point the condition after 19.9 MPa reservoir depletion.

The stress points of the fault under evaluation lies on the largest Mohr circle (see Figure 3.7), because the fault is oriented perpendicular to the minimum horizontal stress direction, i.e. the dip azimuth is 90 degrees with the maximum horizontal stress. The fault dip angle determines the location of the stress point on the largest Mohr-circle. A vertical fault, with a 90 degree dip angle, would position the stress point in the minimum horizontal stress on the horizontal axis, whereas a horizontal fault, with a dip angle of 0 degree, would position the stress point in the (maximum) vertical stress on the horizontal axis. The stress condition of a fault with arbitrary orientation would generate a stress point between the three Mohr circles in Figure 3.7.

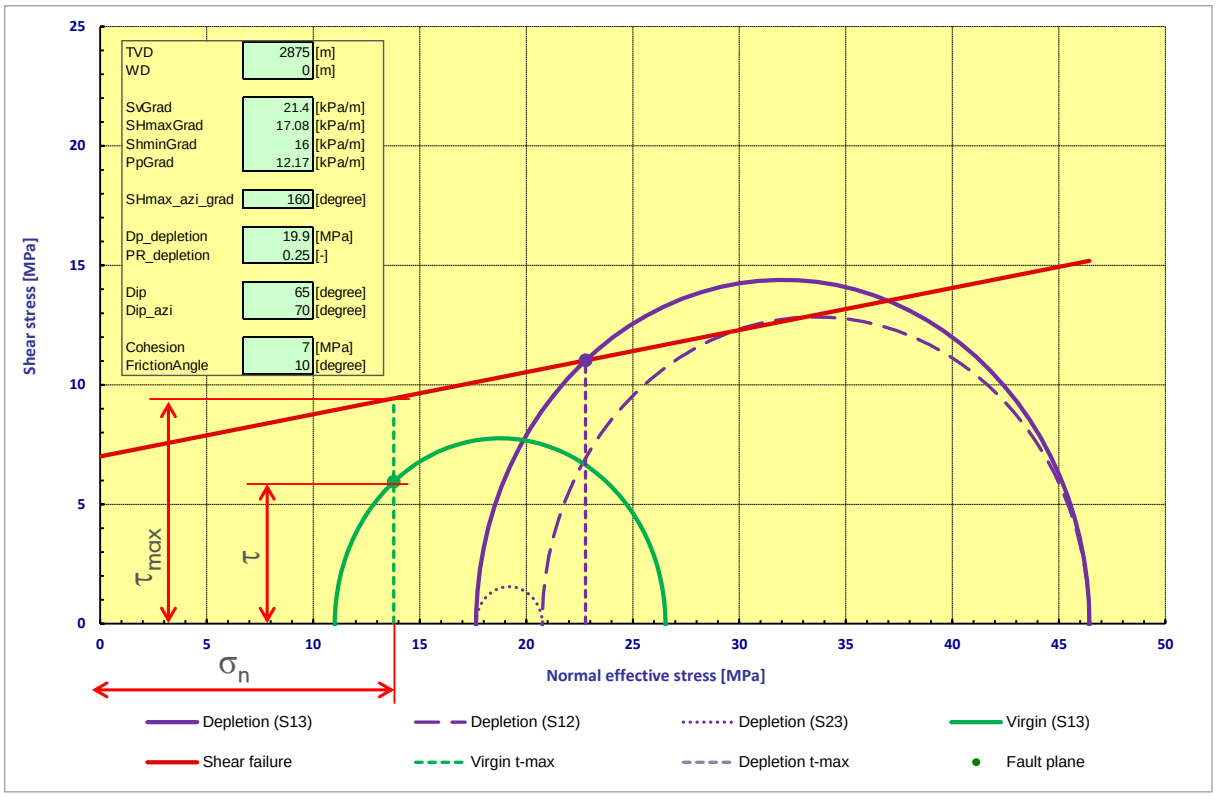

Figure 3.7: Mohr-Circle representation of the effective in-situ stress under virgin (green) and 19.9 MPa reservoir depletion (purple). The dots reflect the normal and shear stress condition on a fault plane with a 65 degree dip angle and 70 degree dip azimuth. Evaluation data is specified in the insert.

The (green) virgin stress point is located below the (red) Mohr-Coulomb shear failure line. The virgin SCU is 0.63 and is calculated as the resultant shear stress component τ divided by the shear stress carrying capacity τ_{max} (see also Chapter 2). The fault is at the onset of slip after 19.9 MPa reservoir depletion, because the (purple) stress point lies on the failure line (the SCU=1). This is exactly the same result as obtained with the finite-element model described in section 3.1.

So, the analytical approach can be used to calculated the reservoir depletion at the onset of fault slip in case of an arbitrary oriented fault, with uniform slip properties, in a subsurface with uniform linear-elastic formation properties and a uniform in-situ stress field. The stress-path coefficient used to determine the in-situ stress under depleted reservoir conditions should be calculated according to equation 2.9 (4) that assumes uni-axial compaction. Other post-failure results obtained from the finite-element analysis, such as the maximum RSD and the length of the slip patch, cannot be determined with the analytical approach.

3.3. Summary of the findings

For the Base case as specified in Chapter 2 it is found that:

- The stress and strain distribution in the depleting reservoir formation
    - Is uniform up to the onset of fault slip. The vertical strain is equal to uni-axial compaction strain.
    - is disturbed within 1 reservoir thickness away from the fault after the onset of fault slip
- The slip patch develops over the entire height of the reservoir after the onset of fault slip, while showing limited growth in the over- and underburden upon further depletion.
- The change of gravity energy of the subsurface induced by reservoir depletion is the energy source being distributed over formation strain energy, formation pressure energy, fault strain (slip) energy and fault pressure energy.
    - The two formation energy terms dissipate the change of gravity energy prior to the onset of fault slip.
    - Energy dissipation by fault slip (strain) is 3 orders of magnitudes smaller than the formation energy terms after the onset of fault slip.
    - The fault pressure energy is negligible for all depletion levels
- The reservoir depletion pressure at the onset of fault slip can be calculated using an analytical solution in case of an arbitrary oriented fault, with uniform slip properties, in a subsurface with uniform linear-elastic formation properties and a uniform in-situ stress field.

Furthermore, for the parameters used in the Base case it is found that

- The onset of fault slip occurs at 19.9 MPa reservoir deletion
- The maximum Relative Shear Displacement (RSD) is about 0.08 m at 30 MPa depletion.
- Energy dissipation by fault slip is less than 0.1% of the change of gravity energy after 30 MPa reservoir depletion.

4. Influence of elastic parameters on the onset of fault slip

The elastic parameters, Young's modulus and Poisson's ratio, have been assumed uniform for all formations in the Base case. Previous work [14] has found that stiffness contrast between reservoir and overburden is a key factor that discriminates fields with and without seismic events in the Netherlands. TNO [15] uses stiffness contrast as one of the parameters to assess the seismic hazard of individual fields. It is highlighted that stiffness contrasts in these studies are the basis to assume a higher total horizontal stress in the overburden and reservoir seals prior to hydrocarbon production, thereby creating a higher threshold for the onset of fault slip.

In this study, the impact of stiffness contrasts is investigated without horizontal stress contrasts between reservoir and top-seal and overburden. Instead, the impact of the elasticity parameters on the stress change induced by reservoir depletion is investigated. Different values for both Young's modulus and Poisson's ratio for the reservoir and non-reservoir formations is investigated. In this chapter, three different configurations are considered for the stiffness contrast in combination with reservoir depletion as indicated in Figure 4.1.

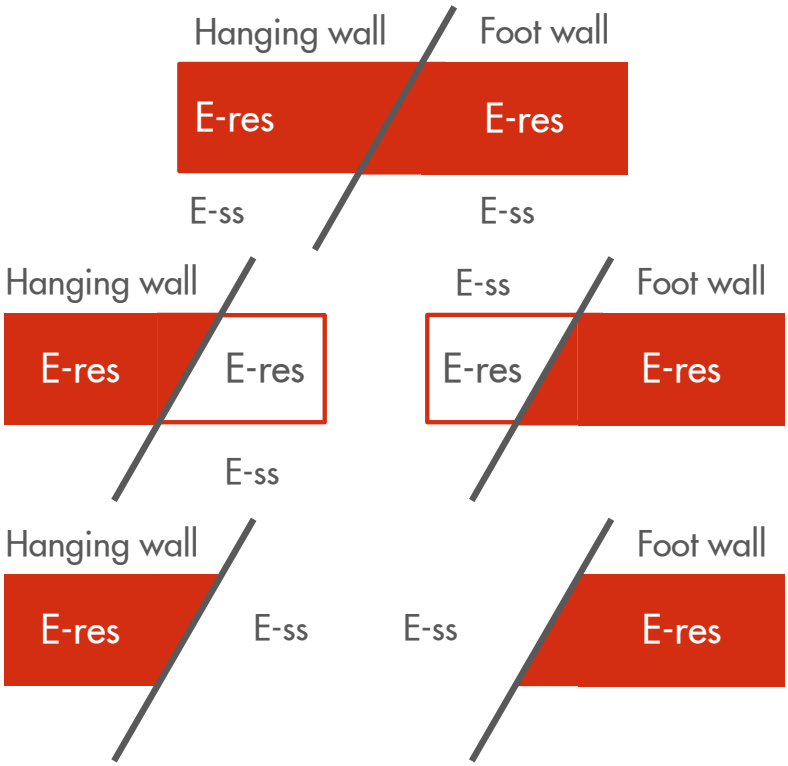

Figure 4.1: **Configuration 1 (top) considers the Base case with a depleting reservoir formation on both sides of the fault; Configuration 2 (middle) also considers a reservoir formation on both side of the fault, but depletion occurs only on a single side of the fault; Configuration 3 (bottom) considers a depleting reservoir on only a single side of the fault. Young's modulus of the reservoir (E-res) is varied relative to Young's modulus of the subsurface (E-ss).**

Configuration 1 considers the Base case with a continuous reservoir formation with Young's modulus E-res and an overburden and underburden with Young's modulus E-ss. Depletion is simulated on both sides of the fault without pressure differential (non-sealing fault). Configuration 2 also considers a continuous reservoir formation, but depletion is simulated in either the foot wall or the hanging wall reservoir formation. Finally, in configuration 3, a discontinuous reservoir formation is assumed on one side of the fault.

So, in Configuration 1 stiffness contrasts are investigated in a horizontally layered subsurface with uniform depletion, while in Configuration 2 the additional impact of a reservoir pressure

differential across the fault is assessed. In Configuration 3, the additional impact of stiffness contrasts across the fault is assessed.

4.1. Impact of Young's modulus on the onset of fault slip

Each of the three configuration is discussed in separate section. All other modelling parameters are the same as in the Base case, i.e. a formation offset of 0m, fault dip angle of 65 degrees, and an azimuth angle of 90 degrees with the maximum horizontal stress.

4.1.1. Configuration 1, Base case

The impact of Young's modulus on the onset of fault slip is investigated for Configuration 1 and compared to the Base-case results described in section 3.1. Three series of sensitivities have been evaluated:

1. Young's modulus is varied for all formations uniformly
2. Young's modulus is varied for depleting reservoir formations only
3. Young's modulus is varied for non-depleting reservoir formations only

This implies that no property contrasts between formations are introduced in Series 1. In Series 2, Young's modulus is kept at 10 GPa for all non-depletion formations, while in Series 3 Young's modulus of the depleting reservoir is kept at 10 GPa. Fifteen values have been considered for Young's modulus in each of the three cases, namely 1.0, 2.5, 5.0, 7.5, 9.0, 10.0, 12.5, 15.0, 17.5, 20, 25, 30, 40, 50, and 100 GPa. For the RO (Rotliegendes) Formation in the Groningen field values have been measured between 3 GPa and 35 GPa, with an average of 14 GPa [12].

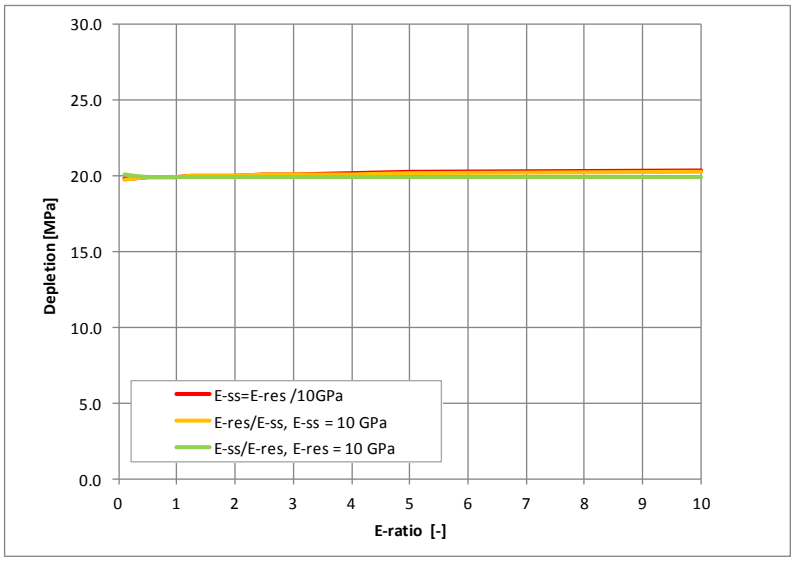

Figure 4.2: Reservoir depletion pressure [MPa] at the onset of fault slip as a function of Young's modulus ratio [-]

Figure 4.2 shows that the influence of stiffness contrasts on the reservoir depletion level at the onset of fault slip is negligible for all three series. Series 1 shows the largest deviation from the base-case results (19.9 MPa) with the onset of fault slip after 19.8 MPa reservoir depletion for an E-ratio of 0.1 and 20.4 MPa for an E-ratio of 10. All other results are within this range.

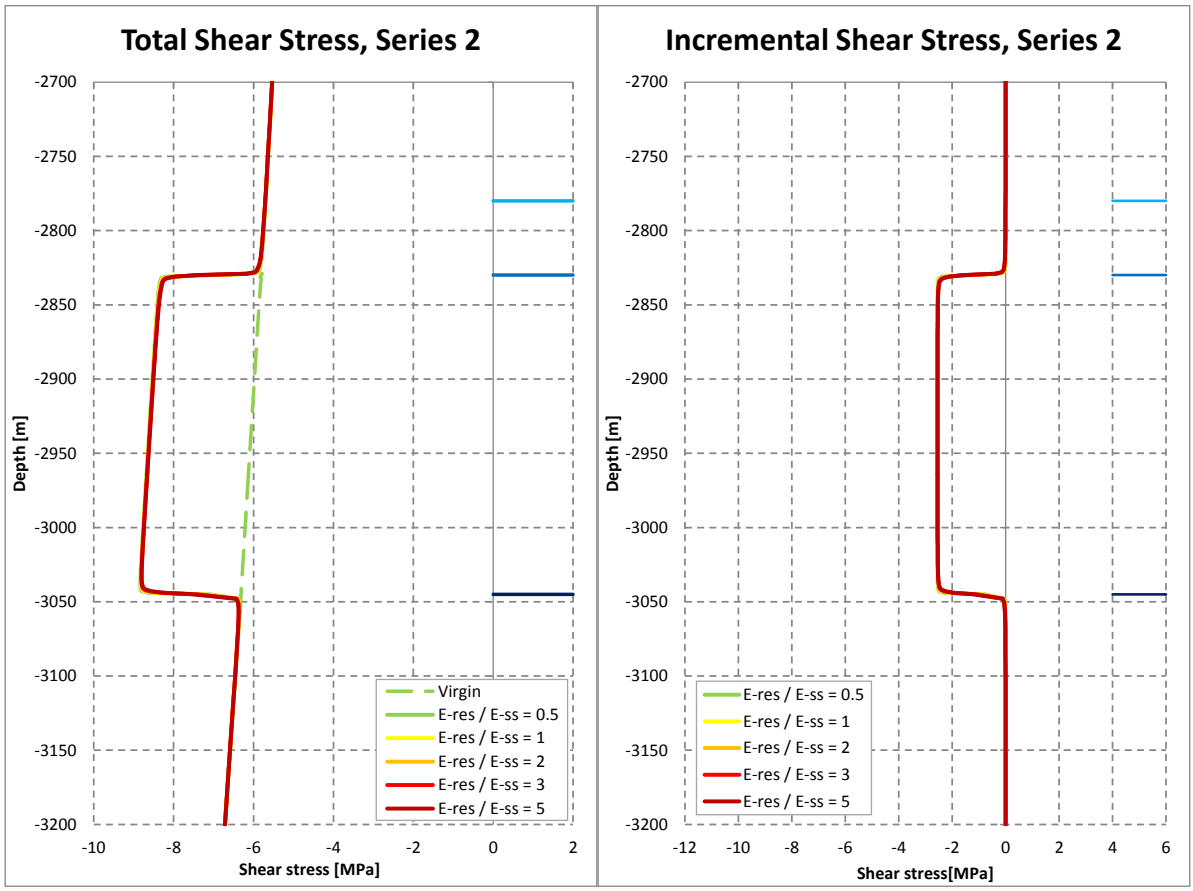

Figure 4.3: Total and incremental shear stress [MPa] along the fault plane for Series 2 as a function of depth [m] induced by 10 MPa reservoir depletion for different values for Young's modulus.

The negligible impact of stiffness contrasts is demonstrated by the total and incremental shear stress along the fault plane after 10 MPa reservoir depletion for Series 2 in Figure 4.3. At this depletion level, no onset of fault slip has occurred yet and the model response is linear elastic. The incremental shear stress is the difference between the total shear stress after 10 MPa depletion and the virgin shear stress condition on the fault plane. The blue horizontal marker lines at the right-hand side in the graphs indicate the interfaces between the four model layers. The virgin shear stress on the fault plane is negative in the current model, which is in downwards direction. It is found that stiffness contrast between reservoir and subsurface has no impact on the shear stress distribution along the fault plane. The same is found for the distribution of the (effective) normal stress. This explains why no impact is found on the onset of fault slip. Similar results are found for Series 1 and Series 3.

Figure 4.4 shows the horizontal effective stress distribution at the top of the reservoir formation as a function of the horizontal coordinate after 10 MPa reservoir depletion. The graph is the same as the yellow line for 10 MPa depletion in Figure 3.2 except that the horizontal coordinate is divided by the reservoir thickness and that the vertical scale is enlarged. The scale enlargement causes a small stress peak to become visible close to the fault and close to boundary of the depleting reservoir. Stiffness contrasts between the reservoir and surrounding formations cause this stress peak to become larger. This causes the slight dependence on Young's modulus in Figure 4.2. Figure 4.3 shows that stiffness contrast between a horizontal depleting reservoir formation and it's subsurface environment does not have an impact on the onset of fault slip.

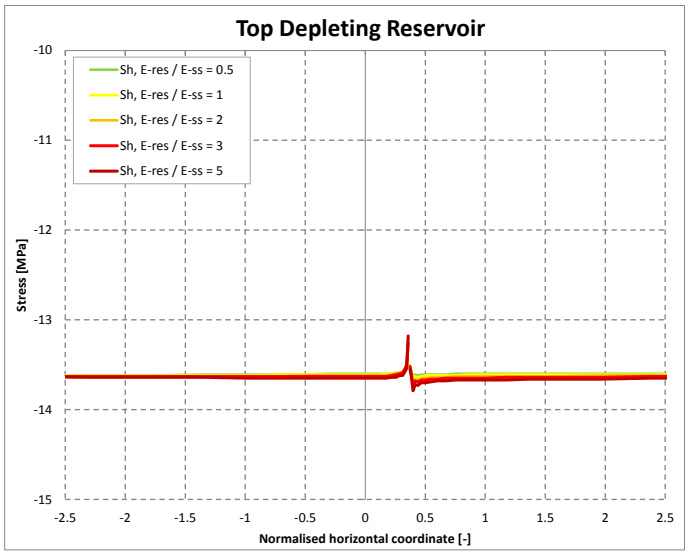

Figure 4.4: **Horizontal stress distribution as a function of the horizontal coordinate normalised for the reservoir thickness at the top of the reservoir under 10 MPa reservoir depletion and for a reservoir Young's modulus of 5, 10, 20, 30 and 50 GPa (Series 2, Configuration 1). Negative values indicate compression.**

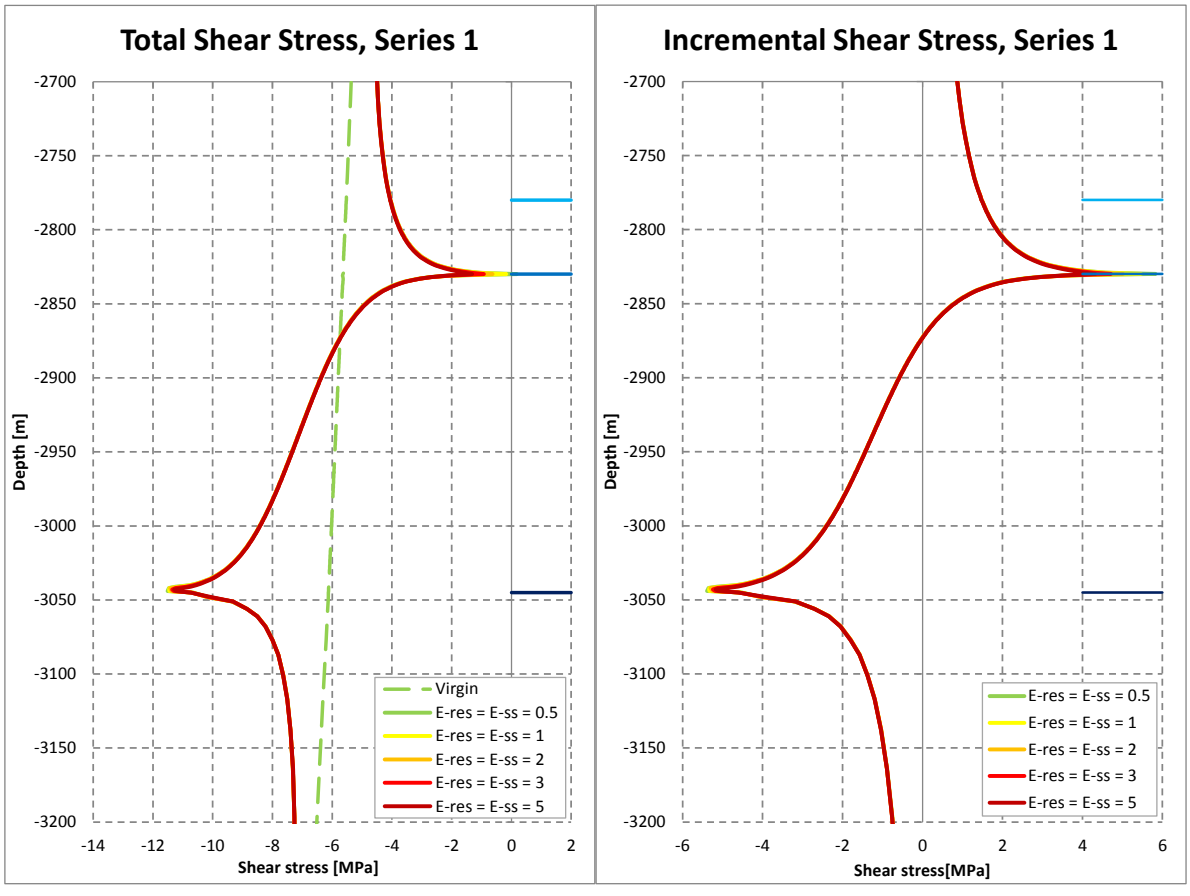

Figure 4.5: **Total and incremental shear stress [MPa] along the fault plane as a function of depth [m] induced by 10 MPa reservoir depletion for Series 1 of Configuration 2 and for different values for Young's modulus.**

4.1.2. Configuration 2

The results of the previous section show that stiffness contrasts between reservoir and overburden have have no impact on the incremental stress as a result of reservoir depletion. In this section, the analyses have been repeated for depletion on a single side of the fault according to Configuration 2 (Figure 4.1). The main difference with Configuration 1 is the introduction of reservoir pressure difference across the fault. The variation of linear-elastic formation properties are the same as in Configuration 1. Six series of evaluations have been conducted, namely:

1. foot wall depletion with varying Young's modulus of all formations uniformly
2. foot wall depletion with varying Young's modulus of the reservoir formations
3. foot wall depletion with varying Young's modulus of all non-reservoir formations
4. hanging wall depletion with varying Young's modulus of all formations uniformly
5. hanging wall depletion with varying Young's modulus of the reservoir formations
6. hanging wall depletion with varying Young's modulus of all non-depleting formations

The impact of stiffness contrasts is demonstrated by the total and incremental shear stress along the fault plane after 10 MPa reservoir depletion in Figure 4.5. The blue horizontal marker lines at the right-hand side in the graphs indicate the interfaces between the four model layers. Reservoir depletion is simulated in Layer 3 at the right-hand side of the fault (foot wall) for Series 1. The incremental shear stress is the difference between the total shear stress after 10 MPa depletion and the virgin shear stress condition on the fault plane. The virgin shear stress on the fault plane is negative in the current model, which is in downwards direction.

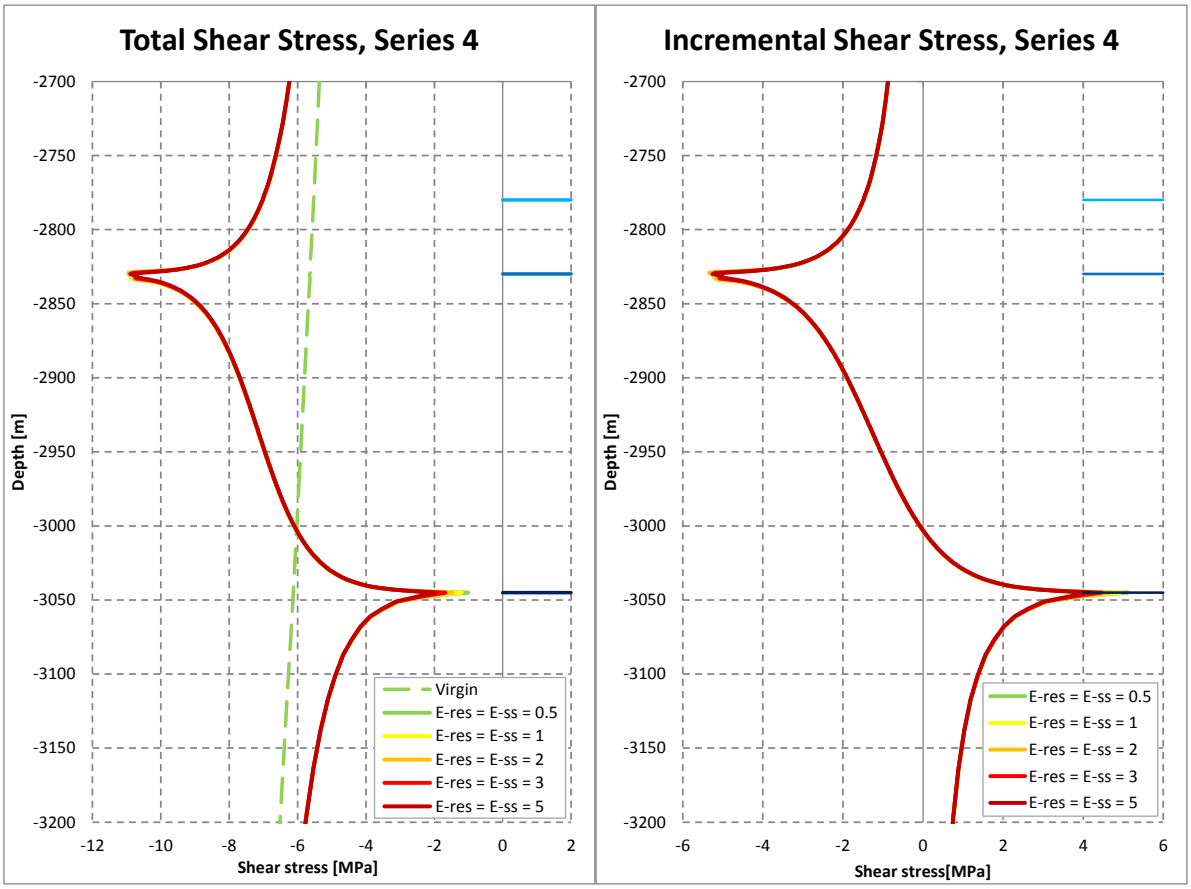

Figure 4.6: Total and incremental shear stress [MPa] for Series 4 as a function of depth [m] induced by 10 MPa reservoir depletion for different values for Young's modulus

It is seen that negative incremental shear stress is developed at the bottom of the depleting reservoir formation in Series 1, whereas positive incremental shear stress is developed at the top. This implies that onset of fault slip occurs at the bottom of the depleting foot wall reservoir

formation. At this location, the incremental shear stress acts in the same direction as the virgin shear stress, whereas at the top of the depleting reservoir formation the incremental shear stress acts in opposite direction and reduces the virgin shear stress level. In other words: the stress paths of all material points along the fault plane are different between Configuration 1 and 2, and explains the difference in onset of fault slip of 19.9 MPa and 7.5 MPa respectively.

It is seen that a uniform variation of Young's modulus of all formations in Series 1 does not have an impact on the stress distribution on the fault plane and therefore on the onset of fault slip. Some difference is seen in the peak shear stress at the top and bottom of the depleting reservoir formation, but these are limited to a very small region. Also, these differences are attributed to the finite-element discretisation that is not able to capture the steep gradients locally. The main point is that the stress paths of (virtually) all material points along the fault plane are unaffected by a uniform change of Young's modulus in Series 1 of Configuration 2.

Similar results are found for Series 4, shown in Figure 4.6, in which the hanging wall reservoir formation is depleted (at the left-hand side of the fault). The main difference with depletion in the foot wall reservoir formation in Series 1 is that negative incremental shear stress is developed and onset of fault slip occurs at the top of the depleting reservoir formation.

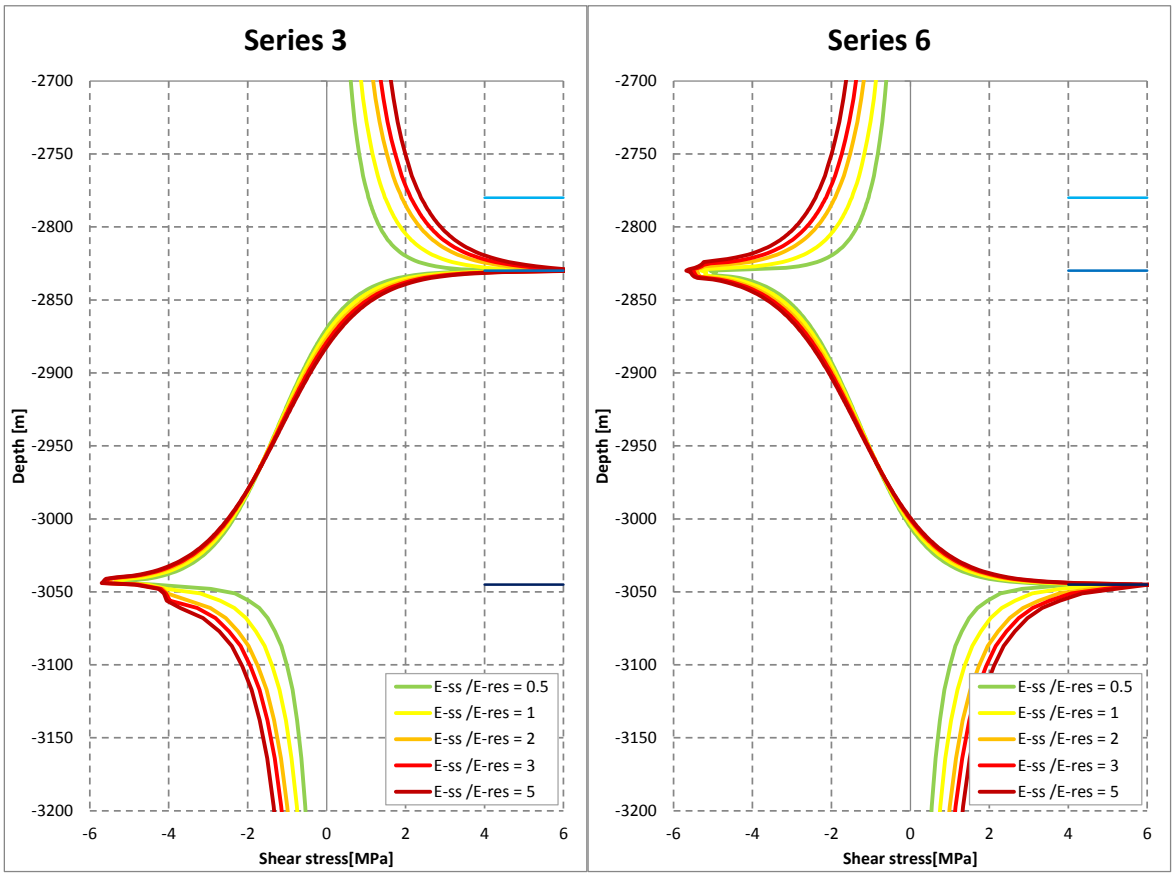

Figure 4.7: Incremental shear stress [MPa] along the fault plane as a function of depth [m] induced by 10 MPa depletion for Series 3 and 6 of Configuration 2 and for different values of the Young's modulus.

Now consider the incremental shear stress for different values of the reservoir Young's modulus in Series 3 and Series 6 in Figure 4.7. In these two series, Young's modulus of the depleting reservoir formation in the foot wall (Series 3) and hanging wall (Series 6) is the same while Young's modulus of the surrounding formations is varied. It is seen that the incremental shear stress induced by reservoir depletion increases with increasing stiffness of the surrounding formations. This is seen in particular along the fault plane across the over- and underburden,

while the impact vanishes into the reservoir formation at the top and bottom. A larger value for Young's modulus implies a larger resistance of the subsurface to reservoir deformation, which is the same for all cases in Series 3 and Series 6. Consequently, the stress response in the surrounding formations is larger in response to the induced reservoir compaction strain, and hence the larger incremental shear stress on the fault plane in the over- and underburden.

In Series 2 and 5 (not shown) the opposite is found. In these series, the Young's modulus of the depleting reservoir formation is varied, while Young's modulus of the surrounding formations is unchanged at 10 GPa. A higher Young's modulus of the reservoir formation leads to smaller compaction strain and therefore a smaller stress response under the same reservoir depletion level.

The impact of stiffness contrasts on the reservoir depletion level that triggers onset of fault slip for Configuration 2 is summarised in Figure 4.8. It is highlighted that in this study onset of fault slip is defined by a SCU value of 1 in single interface element, and is highly influenced by the peak stress values at the interface between depleting reservoir formation and over- and underburden. These peak stress levels are influenced by finite-element discretisation. Therefore, it is better to include the impact of Young's modulus on the stress paths in neighbouring material points in the assessment. The difference seen between foot wall and hanging wall depletion at the onset of fault slip may be attributed to the depth difference at which fault slip occurs in combination with discretisations issues. This difference is therefore not considered meaningful.

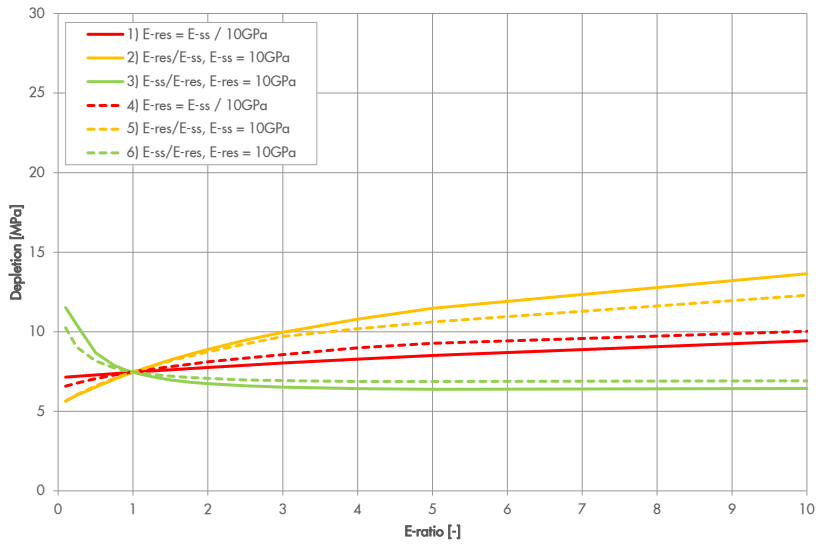

Figure 4.8: Reservoir depletion pressure [MPa] at the onset of fault slip as a function of Young's modulus ratio [-] for Series 1 through 6, Configuration 2.

Also, the shown influence of Young's modulus in Series 1 and 4 is considered not meaningful. This is because the stress distribution along the fault plane is not impacted anywhere else than in the locations of peak stress. The variation in depletion level at the onset of fault slip in Series 1 and 4 is seen as an indicator for the accuracy of model if high peak stresses occur. An alternative definition for the onset of fault slip should be considered to remove unintended modelling aspects from the results. Such a definition could stipulate that multiple interface elements satisfy SCU=1, while a certain slip patch length is exceeded.

The impact of stiffness contrast between the depleting reservoir and the subsurface environment is significant, considering the fact that also the stress response in over- and underburden are impacted. In general, it is found that a higher depletion level at the onset of fault slip is allowed if the reservoir formation is stiffer than the over- and underburden. This corresponds to an E-ratio > 1 in Series 2 and 5 (yellow lines) and an E-ratio < 1 for Series 3 and 6 (green lines).

4.1.3. Configuration 3

The analyses results for Configuration 3 (Figure 4.1) are presented in this section. The main difference with Configuration 2 is the introduction of a stiffness contrast across the fault in combination with the depletion difference across the fault. That is, reservoir depletion is simulated in either the foot wall or the hanging wall reservoir formation. Four series of evaluations have been conducted with:

1. foot wall depletion with varying Young's modulus of the reservoir formations
2. foot wall depletion with varying Young's modulus of all non-reservoir formations
3. hanging wall depletion with varying Young's modulus of the reservoir formations
4. hanging wall depletion with varying Young's modulus of all non-reservoir formations

Fifteen values have been considered for Young's modulus in each Series, namely 1.0, 2.5, 5.0, 7.5, 9.0, 10.0, 12.5, 15.0, 17.5, 20, 25, 30, 40, 50, and 100 GPa. All other modelling parameters are the same as in the Base case.

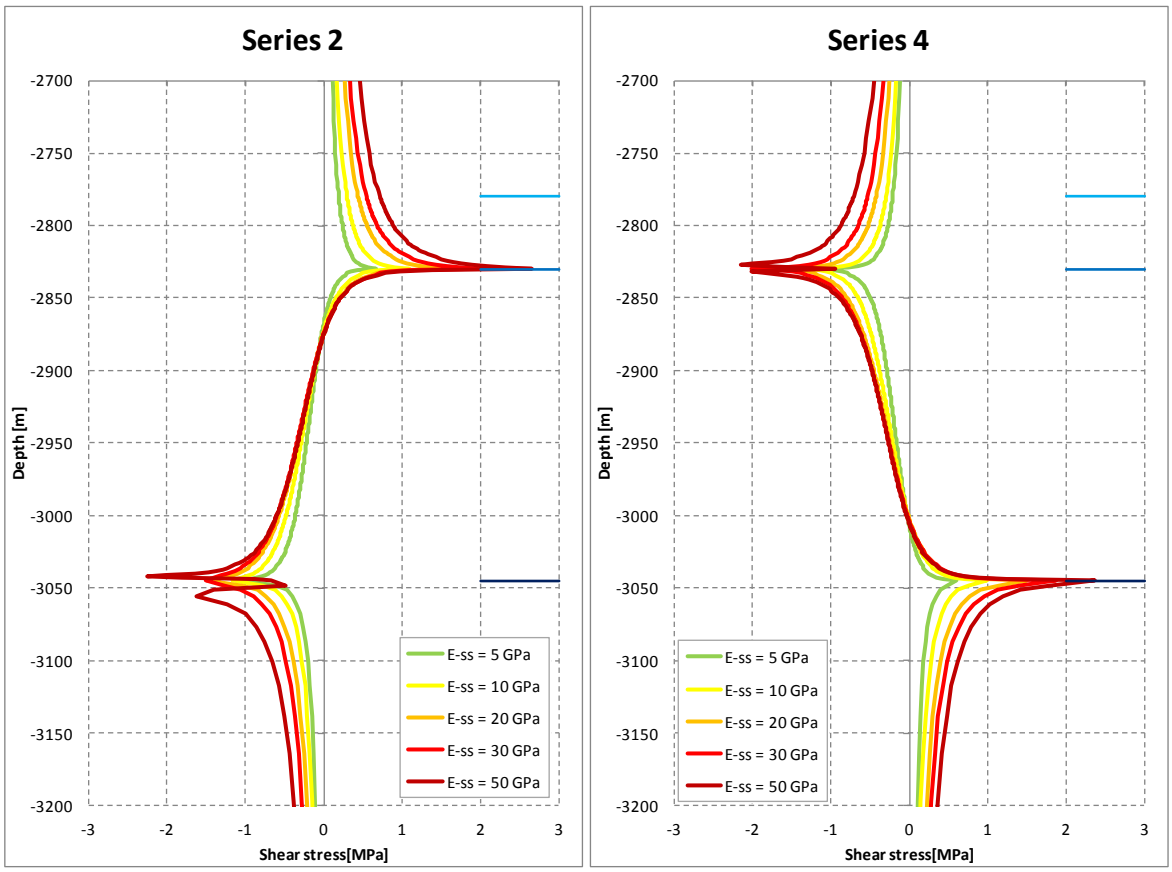

Figure 4.9: Incremental shear stress [MPa] along the fault plane for Series 2 and Series 4 as a function of depth [m] induced by 2 MPa reservoir depletion for different values for Young's modulus.

The impact of stiffness contrasts is demonstrated by the incremental shear stress along the fault plane after 2 MPa reservoir depletion in Figure 4.9. The location of the shear stress peaks is very similar to Configuration 1 and 2, and also the impact of Young's modulus on the shear stress distribution in over- and underburden is similar: A higher Young's modulus of the surrounding formations implies a larger resistance for reservoir deformation and therefore a larger stress response under the same depletion conditions.

In Configuration 3 the shear stress distribution over the reservoir section of the fault plane is also impacted by Young's modulus. In particular close to the peak stress location at the top and bottom of the reservoir, an increase of shear stress is found compared to Configuration 2. This

explains why the impact of Young's modulus is more pronounced in Configuration 3 compared to Configuration 2 (Figure 4.10). The difference between the onset of fault slip due to depletion in the foot wall and the hanging wall is attributed to discretisation and the current definition for onset of fault slip

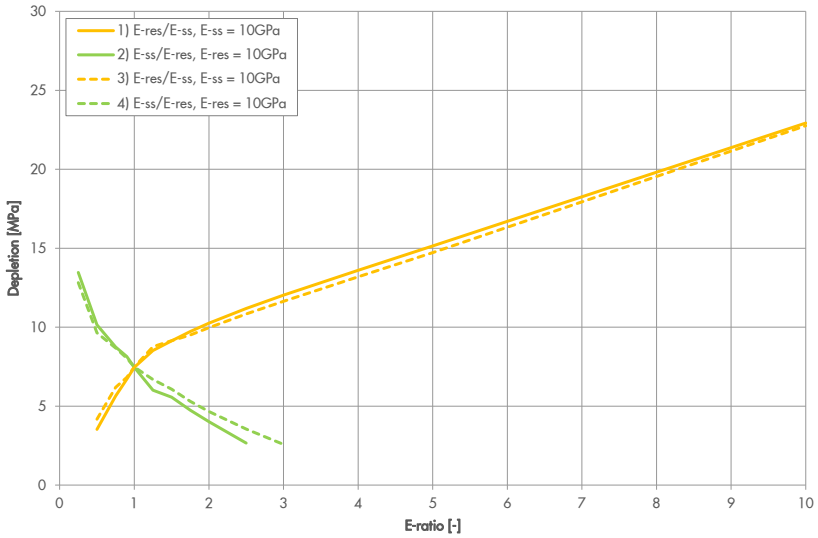

Figure 4.10: Reservoir depletion [MPa] required causing onset of fault slip as a function of the Young's moduli ratio of the reservoir and non-reservoir formations for Configuration 3.

4.2. Impact of Poisson's ratio on the onset of fault slip

In this section, the impact of Poisson's ratio on the fault slip response is investigated and compared to the Base-case results described in Section 3.1. In the Base case formation offset is 0m, fault dip angle is 65 degrees, and the azimuth angle is 90 degrees with the maximum horizontal stress. Two series of runs have been conducted:

1. Poisson's ratio is varied for all formations uniformly
2. Poisson's ratio is varied for depleting reservoir formations only

This implies that no property contrasts between formations are introduced in Series 1, whereas in Series 2, Poisson's ratio is kept at 0.25 for all non-depletion formations. Nine values have been considered for Poisson's ratio in each series: 0.05, 0.10, 0.15, 0.20, 0.25, 0.30, 0.35, 0.40, and 0.45 (For Groningen values between 0.03 and 0.28 have been measured with an average of 0.16 [12]). No cases have been run to investigate the impact of a contrast of Poisson's ratio across the fault.

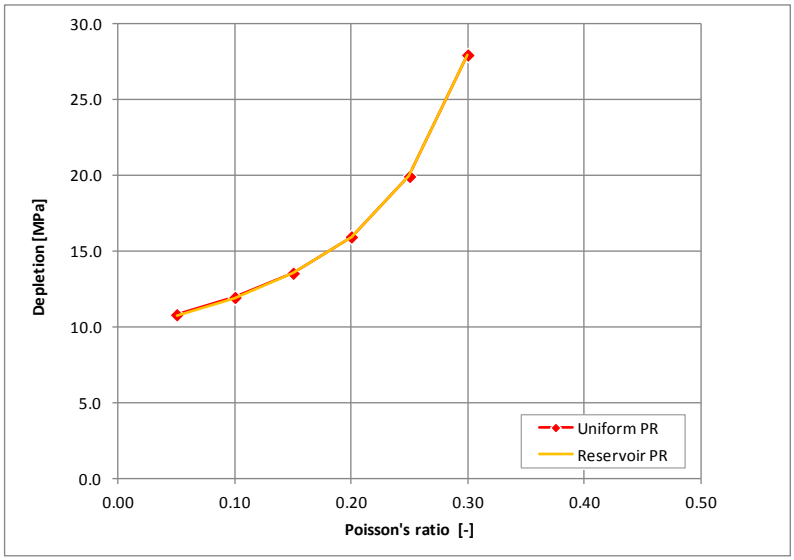

Figure 4.11: Reservoir depletion pressure [MPa] at the onset of fault slip as a function of Poisson's ratio (PR) [-] for the entire model (red line) or the reservoir formation only (yellow line)

Figure 4.11 shows that the depletion level that causes onset of fault slip is significantly influenced by the Poisson's ratio. Also, it is seen that Poisson's ratio of the non-depleting reservoir formations has no impact on the on-set of fault slip. In the Base case, in which Poisson's ratio is assumed 0.25, the onset of fault slip is calculated at 19.9 MPa reservoir depletion. For Poisson's ratios larger than 0.3 no onset of fault slip is calculated, because reservoir depletion is limited to 30 MPa.

4.2.1. Stress distribution in the reservoir

The change of horizontal effective stress is shown in Figure 4.12 for various values of Poisson's ratio and can be simply calculated from (section 2.7):

$$\Delta\sigma_h = \frac{\nu}{1-\nu}\Delta\sigma_v .$$

It is seen that the model results agree well with the theoretical values assuming uni-axial deformation. Reservoir depletion causes the horizontal effective stress to increases more rapidly for values of Poisson's ratio larger than in the Base case. This is expressed by the equation above considering that $\Delta\sigma_v$ is proportional with the change of reservoir pressure. The shear stress on the fault plane increases with increasing difference between the horizontal and vertical effective stress. This is also referred to as the deviatoric stress. The deviatoric stress increases faster with depletion for a low value of Poisson's ratio. Consequently, onset of fault slip is found at a lower depletion level for a lower value of Poisson's ratio than the Base case.

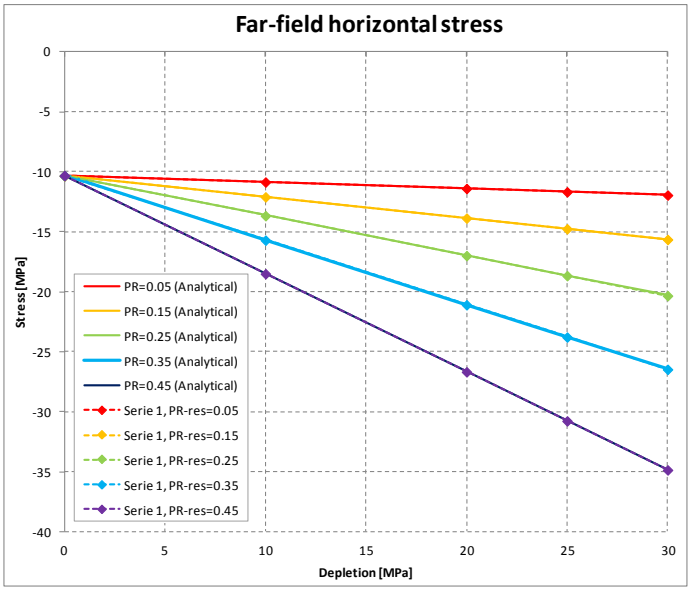

Figure 4.12: **Theoretical and calculated far-field horizontal effective stress as a function of reservoir depletion pressure for various values of Poisson's ratio for the entire model (Series 1).**

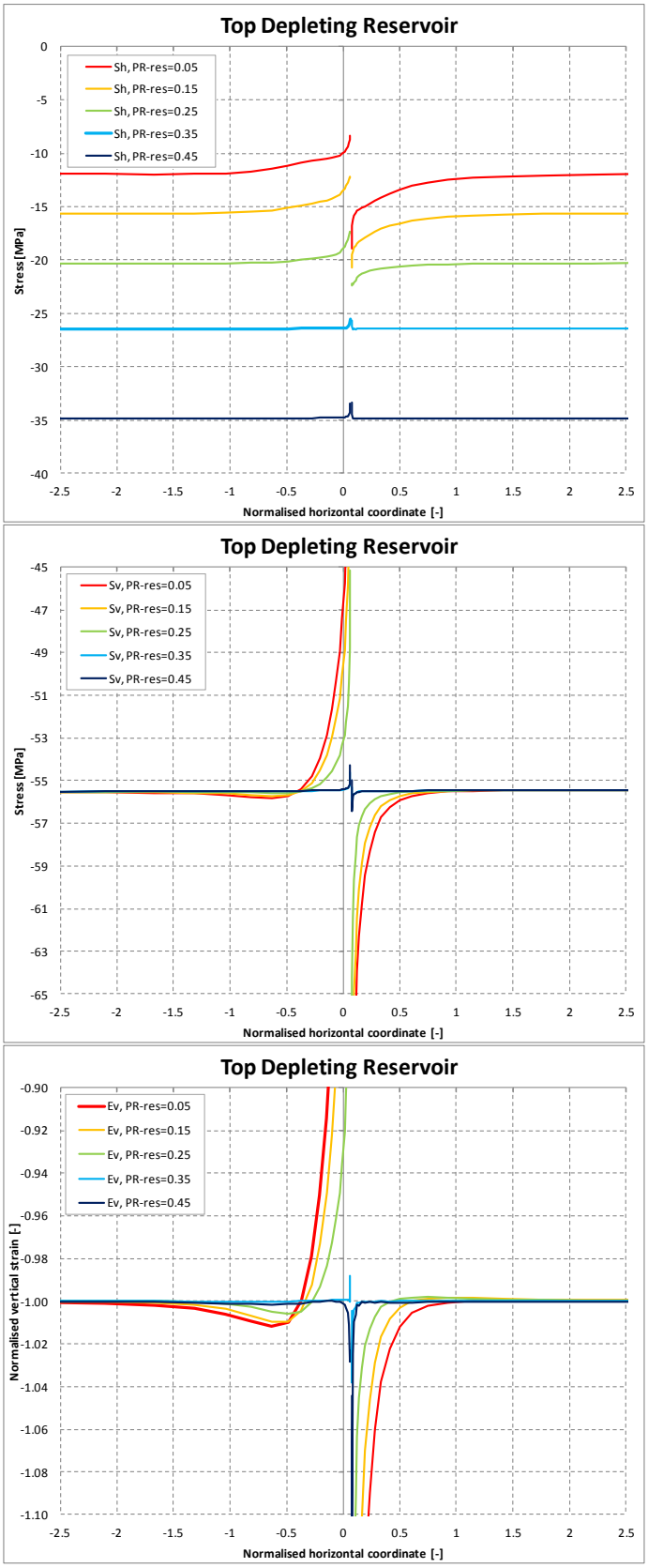

Figure 4.13: **Vertical and horizontal effective stress (top and middle respectively) and the normalised vertical strain (bottom) as a function of the horizontal coordinate normalised for the reservoir thickness at the top of the reservoir under 30 MPa reservoir depletion and for various values for Poisson's ratio.**

Figure 4.13 shows the impact of Poisson's ratio on the stress and strain distribution in the reservoir as function of the normalised horizontal coordinate. It is seen that the vertical effective stress (and strain) is only impacted by Poisson's ratio within a zone less than 1 reservoir thickness from the slipping fault. The peak value for the vertical effective stress deviates more than 10 MPa from the undisturbed value for the extreme case if Poisson's ratio is 0.05, while the peak value for the vertical strain deviated more than 10% from the uniaxial compaction strain.

The horizontal effective stress, however, is impacted uniformly throughout the reservoir. Note that the values for the far-field horizontal stress in Figure 4.13 are the same as those shown in Figure 4.12 at 30 MPa reservoir depletion. At 30 MPa depletion and a Poisson's ratio of 0.35 and 0.45, no fault slip is calculated (Figure 4.11) and a uniform stress and strain condition is obtained in the reservoir. For lower values of Poisson's ratio, the uniform horizontal stress distribution is disturbed in the vicinity of the fault due to fault slip. The disturbed zone remains smaller than 1 reservoir thickness in horizontal direction.

4.2.2. Stress distribution along the fault plane

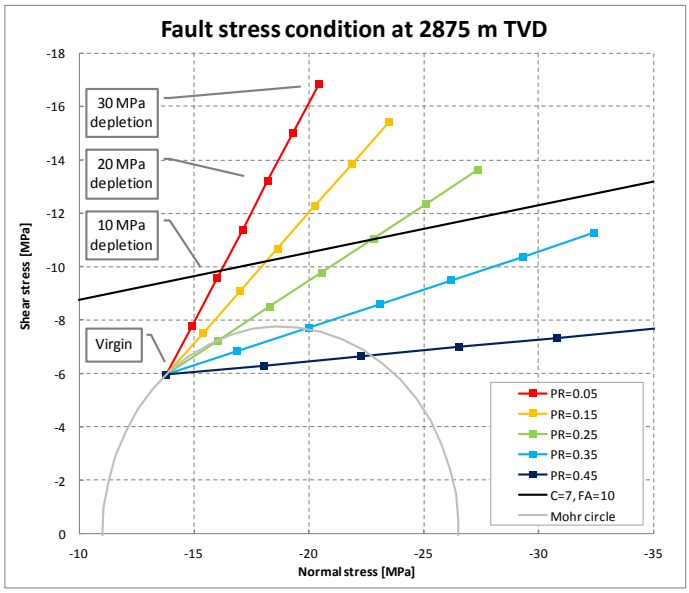

Figure 4.14: Normal and resultant shear stress development on the fault plane at 2875 m TVD for various values of Poisson's ratio as a function of reservoir depletion. The Mohr-circle represents the in-situ stress condition prior to depletion.

The impact of Poisson's ratio on the induced changes of stress and onset of fault slip is also shown in Figure 4.14, in which the analytical approach (Section 2.7) has been used. The finite-element results are identical to those of the analytical approach (Section 3.2). The Mohr circle represents the virgin stress condition in the Base case at 2875 meter Depth. The virgin normal and shear stress condition of the fault, represented by the "Virgin" marker in Figure 4.14 is determined by its dip angle of 65 degree with the horizontal and an azimuth of 90 degree with the maximum horizontal stress. The various lines indicated the development of the normal and shear stress on the fault plane due to depletion for different value for Poisson's ratio and are referred to as stress paths. Markers indicate the stress condition in 5 MPa depletion increments. The normal stress increases more rapidly with increasing value for a Poisson's ratio (see also Figure 4.12). The solid black line represents the assumed Mohr-Coulomb shear failure criterion with a Cohesion of 7 MPa and a friction angle of 10 degree. It is seen that the Mohr-Coulomb shear failure line is intersected at a higher depletion level with increasing value for Poisson's ratio, and that onset of fault slip does not occur under depletion conditions up to 30 MPa for a Poisson's ratio of 0.35 or higher.

4.3. Summary of the findings

For the Base-case configuration, which assumes a horizontally layered subsurface with a uniform depletion across a fault without throw, it is found that

- Poisson's ratio of the depleting formation has a strong impact on the onset of fault slip
    - the stress path followed by the material points on the fault plane that determines the onset of fault slip is strongly influenced by Poisson's ratio of the depleting formation.
    - Poisson's ratios of non-depleting formations have no impact.
- Young's modulus of depleting and non-depleting formations have no impact on the stress path and the onset of fault slip
    - Also in the case of a reservoir pressure contrast across the fault the impact is absent.

For the configuration of a horizontally layered subsurface and a reservoir pressure contrast across the fault without throw, it is found that:

- a lower depletion level is allowed at the onset of fault slip if the over- and underburden have a larger stiffness than the depleting reservoir formation
    - A higher Young's modulus of the surrounding formations implies a larger resistance for deformation and therefore larger stress response under the same reservoir properties and depletion conditions.
- reservoir pressure contrast across the fault has a larger impact on the onset of fault slip than a stiffness contrast of 1:10 between reservoir and over- and underburden.

For the configuration of a fault against a depleting reservoir in a subsurface with uniform but different Young's modulus, it is found that:

- the influence of Young's modulus on the onset of fault slip increases compared to configuration without stiffness contrast across the fault

More generally, it is found that

- the influence of Poisson's ratio on the onset of fault slip is larger than Young's modulus
- pressure differences across the fault have a larger impact on the onset of fault slip than stiffness contrasts in a horizontally layered subsurface
- the current definition of onset of fault slip is influenced by the local occurrence of peak stress.
    - An improved definition of the onset of fault slip should be based on multiple interface elements with SCU=1 in excess of given length of the slip patch

5. Influence of elastic parameters on the energy distribution

The impact of Young's modulus and Poisson's ratio on the energy distribution is investigated for Configuration 1 that is specified in Figure 4.1 of Chapter 4. The results in section 5.1 that address the impact of Young's modulus on the energy distribution are obtained from the same cases as discussed in section 4.1.1, and the results in section 5.2 that address the impact of Poisson's ratio are obtained from the same cases as in section 4.2. So, the same cases are discussed as in Chapter 4, but now with focus on the energy distribution rather than the onset of fault slip. Configuration 2 and 3 are not addressed in this chapter.

5.1. Impact of Young's modulus on the energy distribution

Three series of sensitivities have been evaluated:

1. Young's modulus is varied for all formations uniformly
2. Young's modulus is varied for depleting reservoir formations only
3. Young's modulus is varied for non-depleting reservoir formations only

This implies that no property contrasts between formations are introduced in Series 1. In Series 2, Young's modulus is kept at 10 GPa for all non-depletion formations, while in Series 3 Young's modulus of the depleting reservoir is kept at 10 GPa. Fifteen values have been considered for Young's modulus in each of the three cases, namely 1.0, 2.5, 5.0, 7.5, 9.0, 10.0, 12.5, 15.0, 17.5, 20, 25, 30, 40, 50, and 100 GPa.

The impact of Young's modulus on the change of gravity energy due to subsidence of the overburden is shown in Figure 5.1. The green line, representing Series 3 in which the reservoir Young's modulus is kept constant, does not show a significant influence on the change of gravity energy. The red and yellow lines, representing Series 1 and 2 respectively, show that the energy release is proportional with the uni-axial compressibility C_m (blue line), defined by equation equation 3.1(6).

$$C_m = \frac{(1+\nu)(1-2\nu)}{(1-\nu)} \frac{1}{E}. \tag{5.1}$$

So, the release of gravity energy is determined by the uniaxial compaction of the depletion reservoir formation. It is noted that the width of the finite-element model, which is 2000 m in this study, determines the absolute value of the energy release. In other words, the gravity energy is released by the subsidence of the overburden mass. This explains why no significant difference is seen in the change of gravity energy between Series 1 and 2: Young's modulus of the overburden has no meaningful impact on the subsidence under uni-axial compaction conditions.

The distribution of the change of gravity energy over the four modelling terms is quite different between the three evaluation series. Considering the Base-case conditions (E-ratio=1) and increasing the stiffness of the non-depleting over- and underburden (Series 3, green line in Figure 5.2), it is seen that a reducing fraction of the available gravity energy is dissipated by fault slip with increasing stiffness contrast. This is explained by the reduction of the maximum RSD (Figure 5.3). The energy fraction stored in the fluid system (right-hand side of Figure 5.2) is not impacted by a larger Young's modulus of the non-depleting formations, just like the total gravity energy available for distribution (Figure 5.1). This implies that a reduced fraction of dissipated energy by fault slip is compensated by an increased fraction of formation strain energy, as is shown in Figure 5.2.

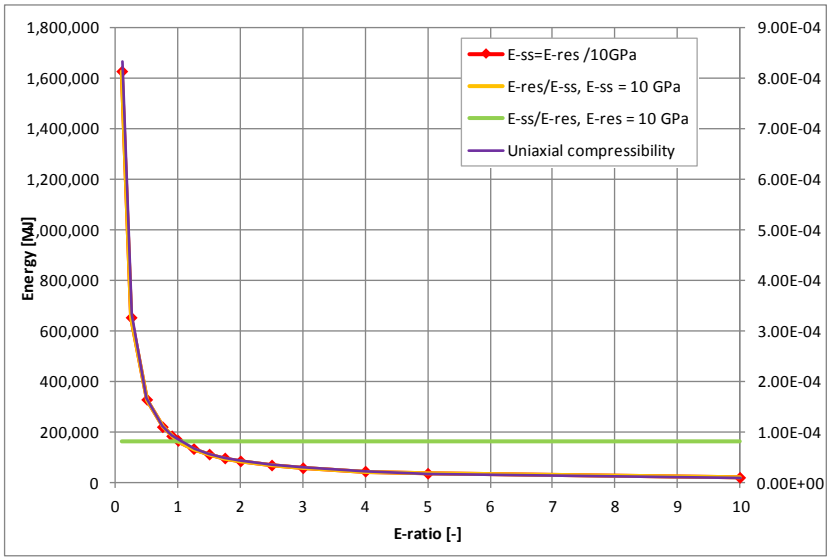

Figure 5.1: **Change of gravity energy [MJ] released due to vertical displacement of under and overburden under 30 MPa depletion for varying Young's modulus of the reservoir (E-res) and non-reservoir (E-ss) formations. For Series 1 the uniform Young's modulus of the subsurface is divided by 10 GPa. E-ratio = 1 represents the Base case. The uniaxial compressibility is plotted against the right-hand scale [1/MPa]**

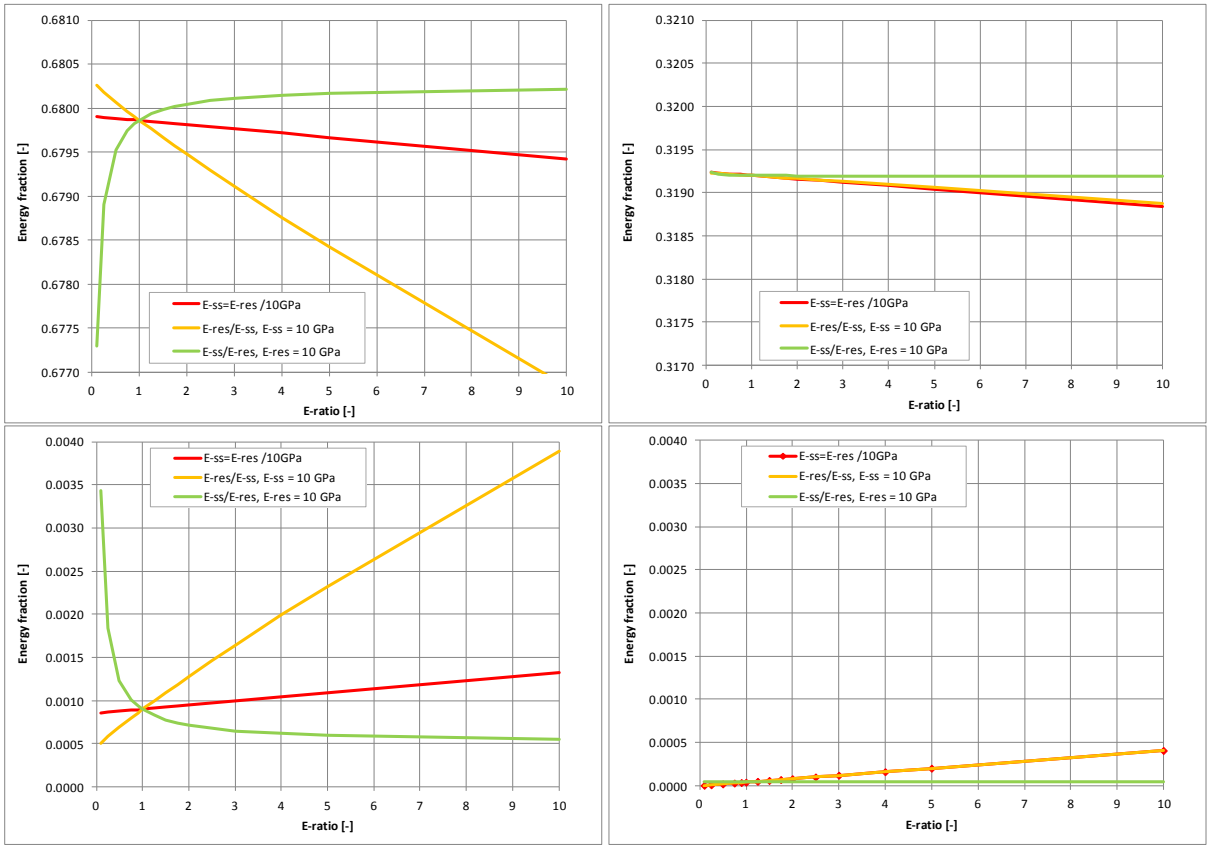

Figure 5.2: **Fraction [-] of the change of gravity energy stored in formation strain (top left), formation pressure (top right), fault slip (top right) and fault pressure (bottom right) under 30 MPa depletion for different Young's moduli of the reservoir (E-res) and non-reservoir (E-ss) formations. The same vertical scale is applied for each energy component.**

Considering Series 2 (yellow line in Figure 5.2), it is seen that the energy fraction dissipated by fault slip increases with increasing stiffness of the depleting reservoir formations. As noted

above, however, the total gravity energy available for distribution reduces with increasing reservoir stiffness. These two effects combined cause the maximum RSD to reduce with increasing reservoir stiffness (Figure 5.3). Series 2 and Series 3 demonstrate the same dependency: a larger fraction of the gravity energy is dissipated by fault slip if the Young's modulus of the depleting reservoir formation is larger than its environment. This is largely compensated by a reduced fraction of formation strain energy.

Series 1 is a combination of Series 2 and Series 3, in which Young's modulus of both depleting and non-depleting formations is changed in the same way. The gravity energy release is the same as for case 2 (Figure 5.1), but the energy distribution is half-way in between those find for Series 2 and Series 3 (Figure 5.2). The difference with Series 2 is found in the distribution between the formation strain energy and the fault slip energy. The reduced energy fraction effect dissipated by fault slip causes the maximum RSD to be further reduced compared to Series 3 and Series 2 (Figure 5.1).

The main difference between the three cases is the maximum Relative Shear Displacement (RSD) as shown in Figure 5.4. The slip patch remains more or less contained to the depleting reservoir formation (not shown) similar to the Base case. The total length of the slip patch is not impacted by Young's modulus. Only the magnitude of the RSD increases significantly with a reduction of Young's modulus.

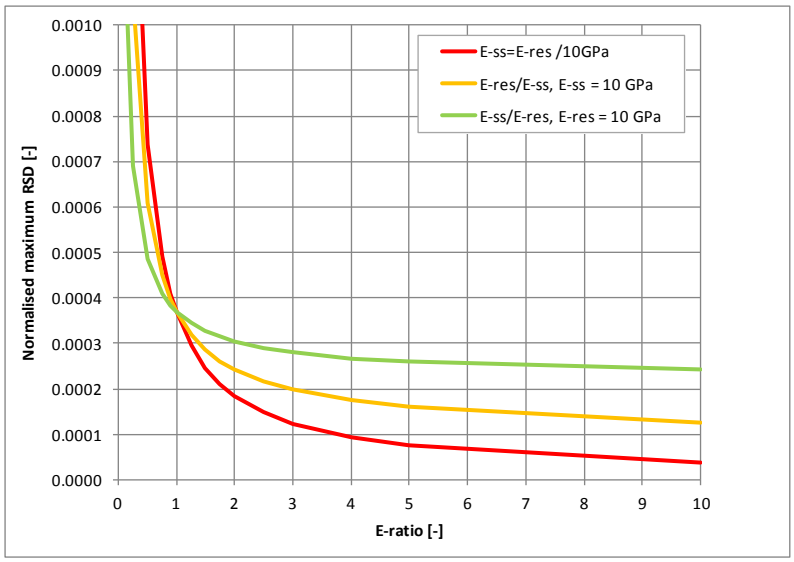

Figure 5.3: Normalised maximum Relative Shear Displacement [-] as a function of Young's modulus ratio [-]

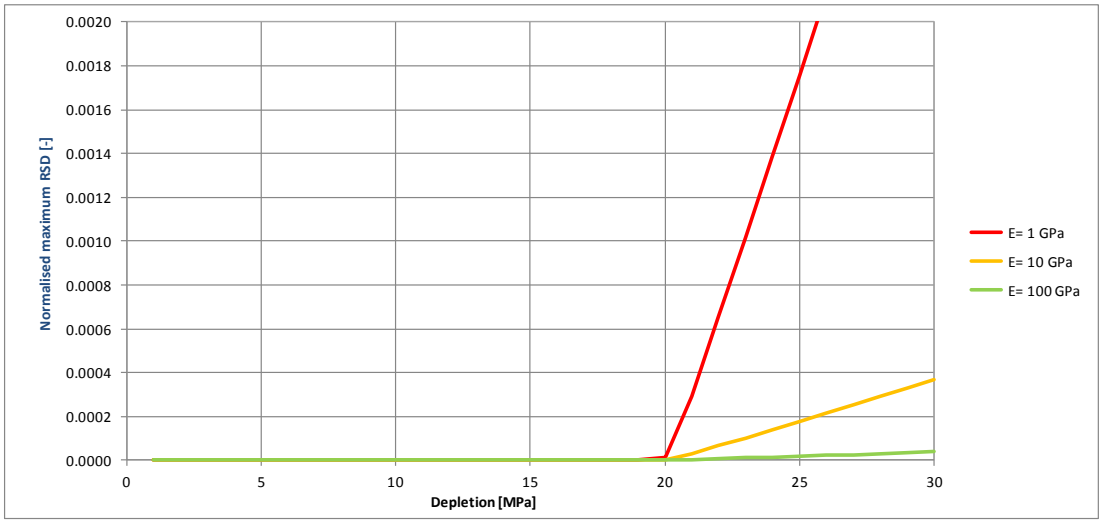

Figure 5.4: Maximum Relative Shear Displacement (RSD) divided by reservoir thickness as a function of reservoir depletion for a uniform Young's modulus of 1, 10 and 100 GPa. Results are shown for Series 1.

5.2. Impact of Poisson's ratio on the energy distribution

In this section, the impact of Poisson's ratio on the energy distribution is investigated and compared to the Base-case results described in Section 3.1. Two series of runs have been conducted:

1. Poisson's ratio is varied for all formations uniformly
2. Poisson's ratio is varied for depleting reservoir formations only

This implies that no property contrasts between formations are introduced in Series 1, whereas in Series 2, Poisson's ratio is kept at 0.25 for all non-depletion formations. Nine values have been considered for Poisson's ratio in each series: 0.05, 0.10, 0.15, 0.20, 0.25, 0.30, 0.35, 0.40, and 0.45. No cases have been run to investigate the impact of a contrast of Poisson's ratio across the fault.

Figure 5.5 shows the release of gravity energy due to subsidence of the overburden as a function of Poisson's ratio, while Figure 5.6 shows the distribution of the energy over the four terms in the current model. It is seen that the release of gravity energy is proportional with the reservoir compressibility given by equation 5.1 (7), and that Poisson's ratio of non-depleting reservoir formations does not have an impact. So, the total gravity energy available reduces with increasing Poisson's ratio and becomes negligible if Poisson's ratio approaches 0.5 (incompressible material behaviour). Also, it is seen that the energy fraction dissipated by fault slip increases with reduction of Poisson's ratio (i.e. an increase of the compressibility). This is compensated by the energy fraction stored in the formation strain.

The absence of fault slip under 30 MPa depletion for Poisson's ratio larger that 0.3 is reflected by the dissipated energy by fault slip. The dependency on compressibility and relationship between fault slip energy and formation strain energy are similar to those found for Young's modulus discussed in the previous section.

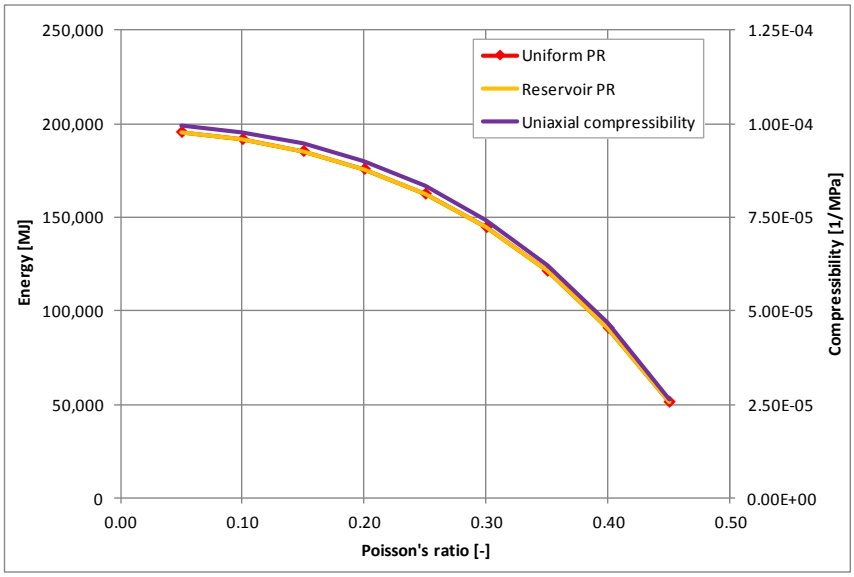

Figure 5.5: **Gravity energy release [MJ] under 30 MPa depletion as a function of Poisson's ratio for the entire model and for the depleting reservoir formation only. The uniaxial compressibility is plotted against the right-hand scale [1/MPa]**

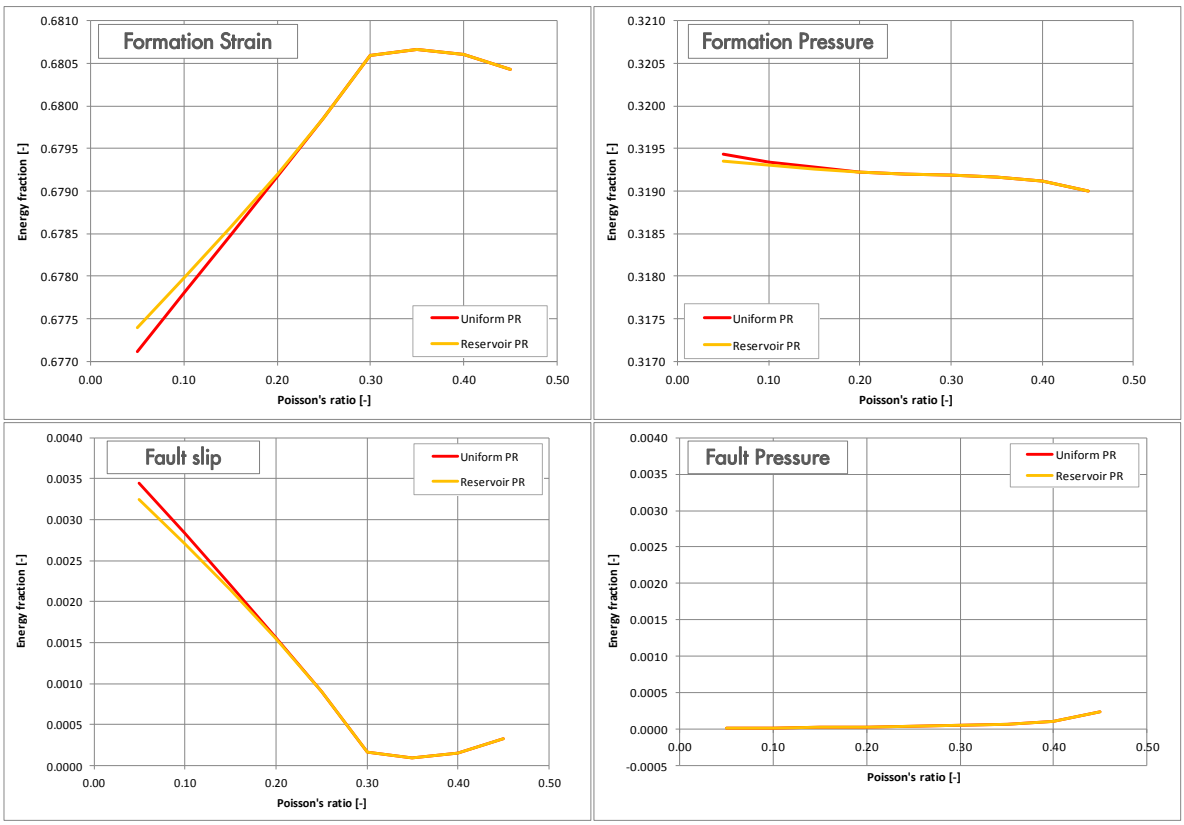

Figure 5.6: **Gravity energy fraction [-] stored or dissipate in formation strain, formation pressure, fault slip and fault pressure under 30 MPa depletion as a function of Poisson's ratio for the entire model and for the depleting reservoir formation only.**

5.3. Summary of the findings

For the Base case, which constitutes a case of a fault without throw in a uni-axial compacting reservoir and a uniform linear-elastic subsurface, it is found that

- The release of gravity energy is proportional with the uni-axial compressibility of the depleting reservoir formation.
    - Compressibility of non-depleting formations does not impact the release of gravity energy. This implies that also Young's modulus and Poisson's ratio of non-depleting formations do not impact the release of gravity energy.
    - Energy dissipated by fault slip is compensated by a reduction of the formation strain energy.
- The distribution of the released gravity energy over formation strain energy and fault slip energy is strongly influenced by Young's modulus and Poisson's ratio of the depleting formations.
    - Young's modulus of non-depleting formations also impacts the distribution between these two energy terms.
    - Poisson's ratio of non-depleting formations does not have an impact.
- The distribution of the released gravity energy over formation and fault pressure energy terms is impacted to a much smaller degree by Young's modulus.
    - Poisson's ratio has no impact on the energy distribution between these two terms.

6. Influence of the in-situ stress and shear failure properties

So far in this study, the fault strength of cohesion *C*, briefly refered to as cohesion, has been assumed 7 MPa and the fault friction angle φ 10 degrees. The assumption for *C* may be considered rather high, while the friction angle may be regarded rather low. In the end, it is the shear stress carrying capacity τ_{max} that determines the slip condition in each material point along the fault plane and is defined by both parameters in the Coulomb friction law:

$$\tau_{\max} = C + \sigma_n \tan\varphi \tag{6.1}$$

With σ_n the normal (effective) stress in any point on the fault plane.

In this chapter it is shown that different value combinations for Poisson's ratio, Cohesion, Friction angle and minimum horizontal stress gradient may cause onset of slip at the same reservoir depletion pressure for a given depth, but a different fault slip response upon further depletion. In Section 6.1, attention is focussed on Cohesion and Friction angle, whereas in Section 6.2 the additional impact of the minimum horizontal stress is assessed on the onset of fault slip.

6.1. Impact of Cohesion and Friction angle

First, a single point on the fault plane is considered at a depth of 2875 m TVD. The Base-case assumptions (Chapter2) are assumed, which include:

- Young's modulus of 10 GPa and Poisson's ratio of 0.25
- Cohesion of 7 MPa and a friction angle of 10 degrees
- Fault dip angle of 65 degrees with horizontal
- Fault dip azimuth of 90 degrees with maximum horizontal stress
- No formation offset
- Vertical stress gradient of 21.4 kPa/m
- Minimum horizontal stress gradient of 16.0 kPa/m

At this point on the fault plane the virgin stress state is (Figure 6.1):

- Normal (effective) stress 13.7 MPa
- Resultant shear stress 5.9 MPa

The onset of fault slip occurs at the intersection of the stress path and the failure line. Alternative stress paths are followed for different values for Poisson's ratio ν as discussed in section 4.2 and shown in Figure 6.1. The stress path followed in the Base case is given by the green dashed line for ν=0.25. The points on the stress path lines mark the stress condition on the fault plane in increments of 5 MPa reservoir depletion. The grey line represents the Mohr Coulomb failure condition assumed in the Base case. The Base-case stress path intersects this failure line after 19.9 MPa reservoir depletion (section 3.1).

The horizontal green solid line represents an alternative Mohr-Coulomb failure line that also intersects the Base-case stress path at 19.9 MPa reservoir depletion. This alternative failure line is specified by a *C* of 11.0 MPa and a φ of 0 degrees. In a similar fashion, Mohr-Coulomb failure lines can be constructed that predict onset of fault slip at 19.9 MPa depletion for different stress paths and associated Poisson's ratio, as shown in Figure 6.1. In this case, $\varphi=0$ in all cases and the *C* is adjusted.

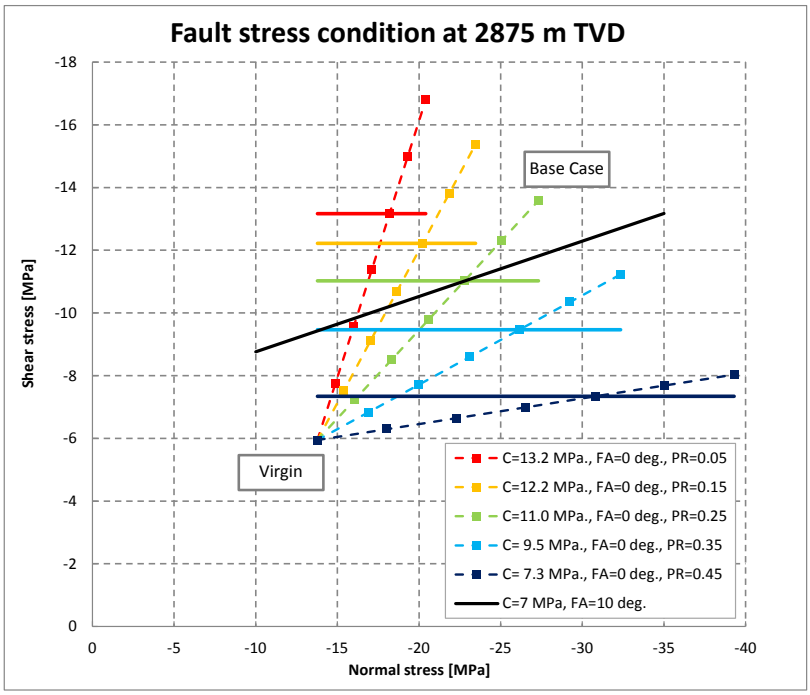

Figure 6.1: **Alternative failure lines to cause onset of slip at 2875 m deptph after 19.9 MPa reservoir depletion for various values for Poisson's ratio (PR).**

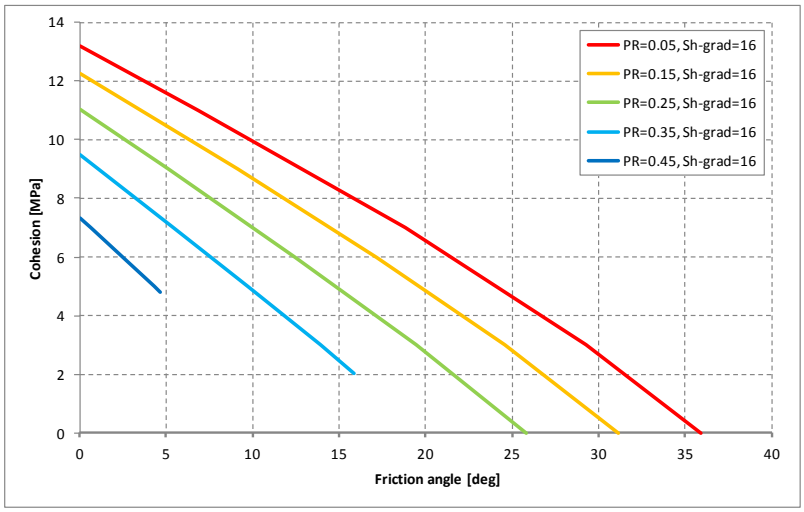

Figure 6.2: **Relationships between Cohesion and Fiction angle for various values of Poisson's ratio that cause onset of slip at 2875 m depth after 19.9 MPa reservoir depletion and a minimum horizontal in-situ stress gradient of 16.0 kPa/m (Base case).**

Other (positive) value combinations for Cohesion and Friction angle can be calculated using expression (5.1) such that the same value for τ_{max} is obtained compared to the Base case. The result is given in Figure 6.2, which shows the combination of values for Poisson's ratio, Cohesion and Friction Angle that causes onset of slip after 19.9 MPa reservoir depletion at 2875 m depth. Additionally, it is assumed that the onset of fault slip does not occur under virgin stress conditions, so that the Mohr-Coulomb failure should lie above the virgin stress point. This explains the narrow range of values for the friction angle between 0 and about 5 degrees that can be considered in combination with a Poisson's ratio of 0.45.

Next, the onset of fault slip and the subsequent fault response is considered using finite-element techniques for an entire fault section across a depleting reservoir without offset. Eight different value combinations for the cohesion and friction angle have been taken (Table 6.1). The Base case (Chapter 3) is catured in the first value combination. The other seven cases have a lower

cohesion and higher friction angle, and follow the green line in Figure 6.2. That is, all value combinations are aimed to cause onset of fault slip at about 20 MPa reservoir depletion. Cases with a friction angle lower than the Base case are not considered very realistic. Poisson's ratio and the minimum horizontal in-situ stress are according to the Base case.

Table 6.1: Cohesion and Friction angle that cause onset of fault slip after about 20 MPa reservoir depletion, assuming Base case properties (Poisson's ratio is 0.25, and minimum horizontal stress is 16.0 kPa/m).

Cohesion [MPa]	Friction angle [deg]
7	10
6	12.5
5	15.0
4	17.4
3	19.7
2	22.0
1	24.2
0	26.4

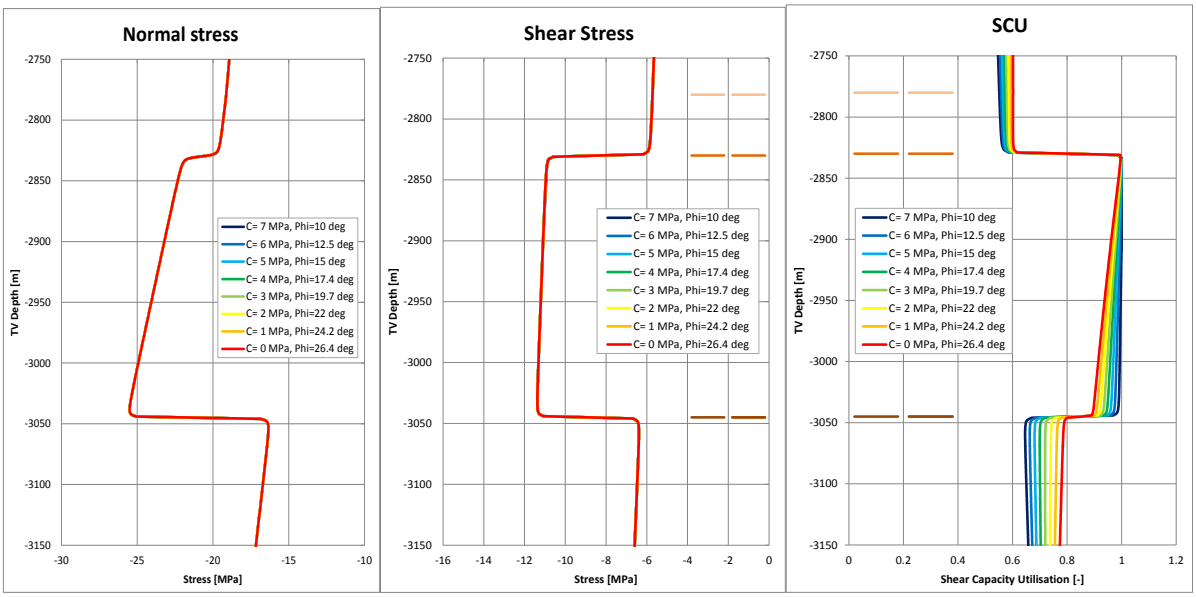

Figure 6.3: Effective normal stress (left), shear stress (middle) and fault Shear Capacity Utilisation (right) as a function of depth after 20 MPa reservoir depletion for the eight value combinations of cohesion and friction angle in Table 6.1

Figure 6.3 shows that the fault is at the onset of slip after 20 MPa depletion for all value combinations in Table 6.1. It is seen that the SCU=1 at the most shallow point of the depleting reservoir for all cases, and that the SCU is smaller and reduces faster with depth for larger values of the friction angle. This is explained by the larger shear strength τ_{max} that increases with normal stress and depth.

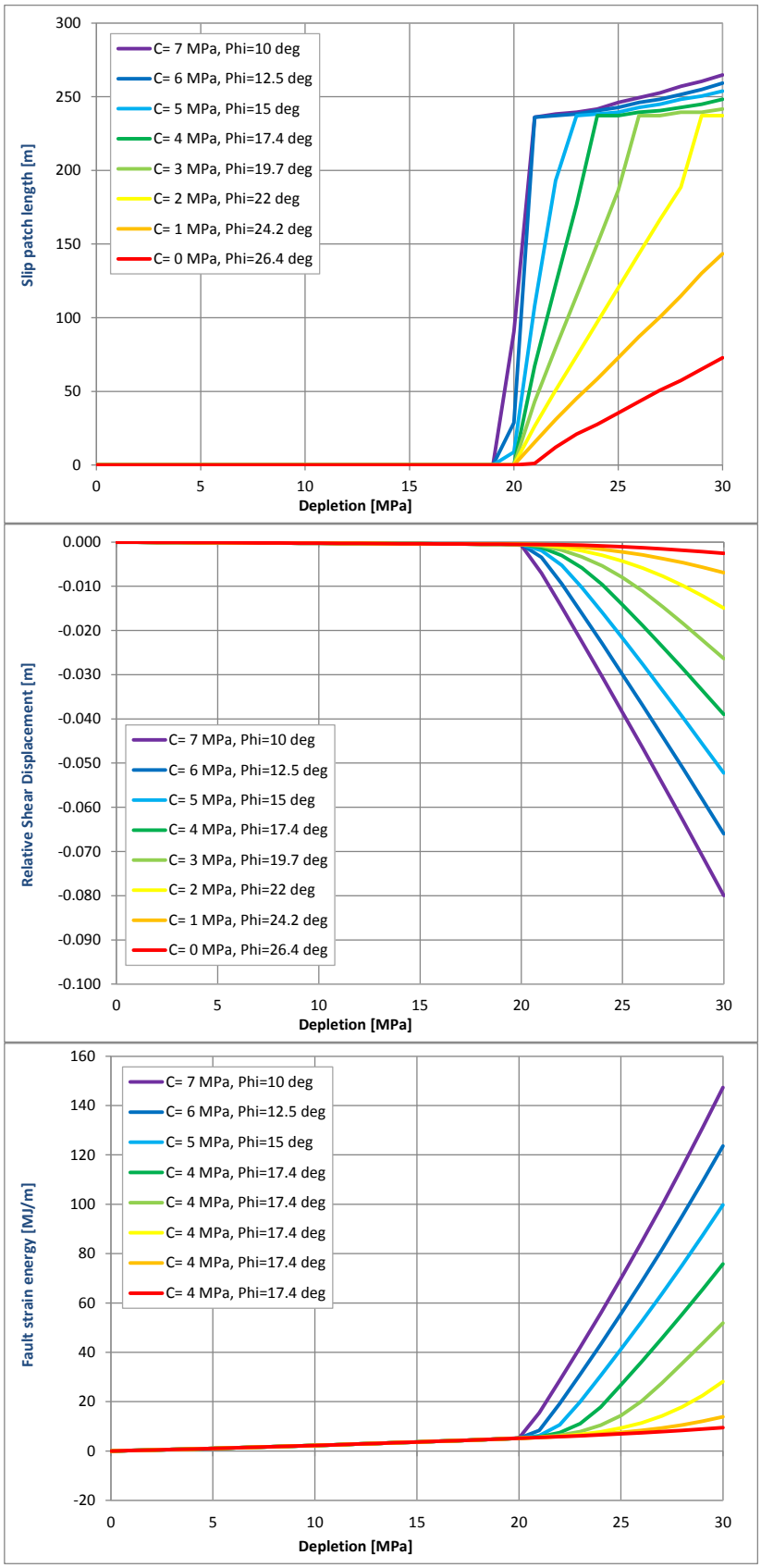

Figure 6.4: **Length of the slip patch (top), the maximum Relative Shear Displacement (middle) and the energy dissipated by fault slip (bottom) as a function of reservoir depletion for the eight value combinations of cohesion and friction angle in Table 6.1.**

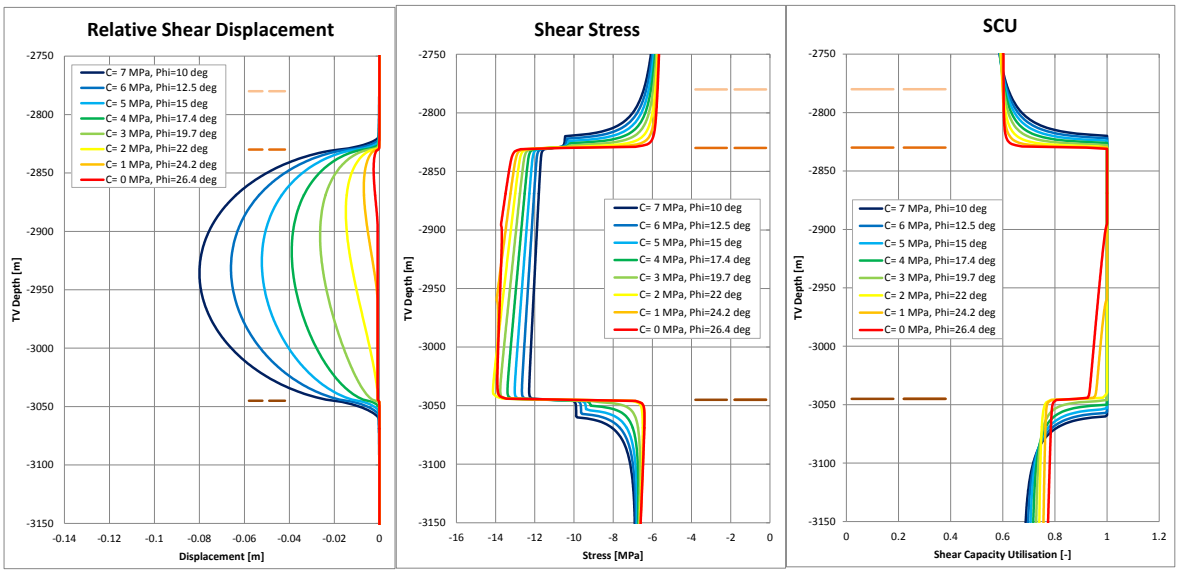

Figure 6.5: Relative Shear Displacement (RSD, left), shear stress (middle) and SCU (right) as a function of depth after 30 MPa reservoir depletion for the eight value combinations of cohesion and friction angle in Table 6.1.

The slip response after the onset of fault slip differs between the 8 cases (Figure 6.4). It is seen that the length of the slip patch, the maximum RSD and the energy dissipated by fault slip develop much slower for larger friction angle due to the residual shear strength of the fault (SCU<1) over the reservoir formation. At 30 MPa reservoir depletion (Figure 6.5), the slip patch is fully developed over the reservoir height of 215 m, except for the cases with 0 and 1 MPa cohesion. The RSD ranges from less than 3 mm for the case with 26.4 degree friction angle to about 80 mm for the Base case with 10 degree friction angle. So, it is concluded that a different slip responses can be simulated while the onset accurs at the same reservoir depletion level by varying the fault friction angle and adjusting the fault cohesion.

6.2. Impact of minimum horizontal stress

The Base case assumes a virgin total minimum horizontal stress gradient of 16.0 kPa/m (1.60 bar/10m) [10]. However, this gradient is usually uncertain and is expected in a range between 15.4 and 16.6 kPa/m in the current study. The impact of this uncertainty is reflected on the virgin stress condition of the fault plane, as shown in Figure 6.6. The Mohr circles correspond with three possible minimum horizontal stress gradients, namely the low case, the Base case and the high case. The uncertainty of the minimum horizontal stress causes a shift of the left-most point of the Mohr circle. The right-most point on the circle corresponds with the vertical effective stress and is considered to be known from density log integration. The virgin stress point on the Mohr circle is determined by the dip angle of the fault (see next section). The stress paths for a Poisson's ratio of 0.05 and 0.45 are indicated for the three minimum horizontal stress assumptions, while the markers indicate the stress condition with 5 MPa pressure depletion increments. It is seen that the stress paths shift accordingly.

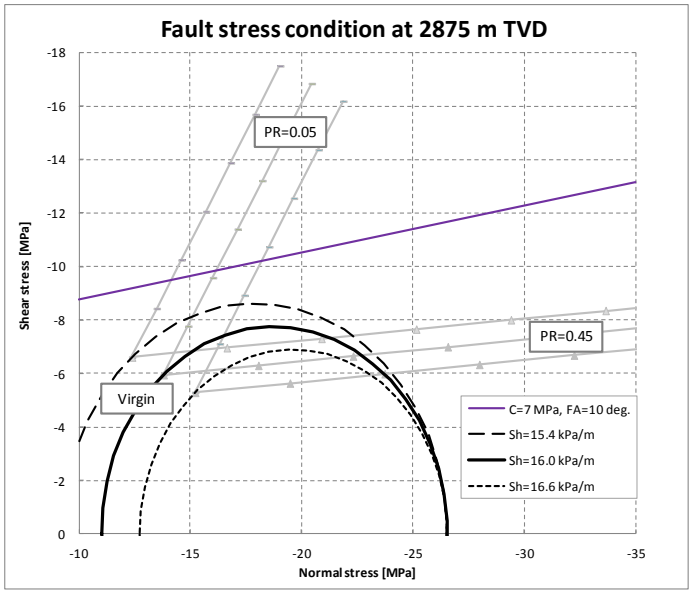

Figure 6.6: **Uncertainty in the minimum horizontal stress shifts the origin of the stress paths for different values for Poisson's ratio (see Figure 6.1).**

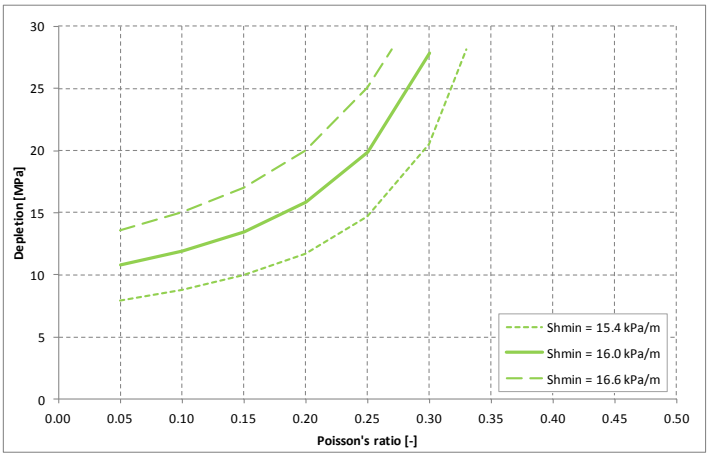

Figure 6.7: **Reservoir depletion pressure [MPa] at the onset of fault slip as a function of Poisson's ratio [-] for different values for the total virgin minimum horizontal stress gradient (no formation offset).**

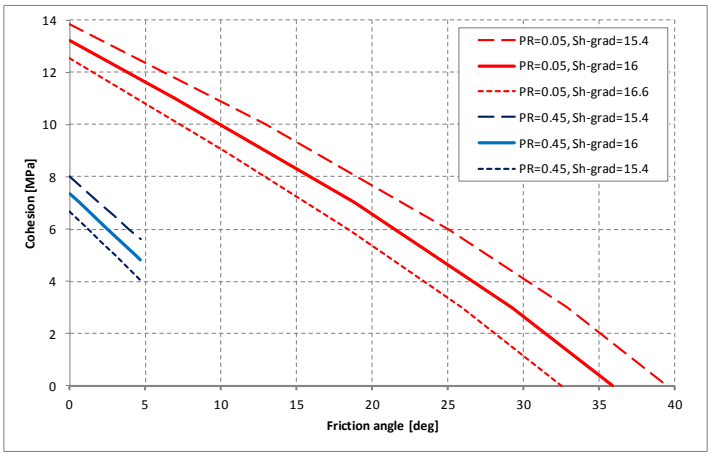

Figure 6.8: **Impact of the minimum horizontal in-situ stress gradient on the relationship between Cohesion and Fiction angle that cause onset of fault slip after 19.9 MPa reservoir depletion for a Poisson's ratio of 0.05 and 0.45. See Figure 6.2 for the relationship for other values of Poisson's ratio.**

The impact of minimum horizontal stress uncertainty on the relationship between Poisson's ratio and the onset of fault slip is shown in Figure 6.7. It is seen that a larger minimum horizontal stress requires a larger reservoir depletion to develop a critical stress condition on the fault plane. This is also reflected in the relationship between Cohesion and Friction angle to trigger fault slip at a depletion level of 19.9 MPa. Figure 6.8 shows the impact of the minimum horizontal stress uncertainty for a Poisson's ratio of 0.05 and 0.45 as extreme cases.

6.3. Impact of fault dip angle

The fault orientation in terms of fault dip angle and fault dip azimuth (see Chapter 2 for the definition) varies considerably across the Groningen Field. Most faults are quite steep with a dip angle between 70 and 80 Degreess with the horizontal axis. The Base case dip angle of 65 Degrees actually relatively low.

The impact of this variability is reflected on the virgin stress condition of the fault plane, as shown in Figure 6.9. No shear stress is exerted on a vertical fault plane (at 90 degrees with the horizontal axis) perpendicular to the minimum horizontal stress. This is presented by a virgin stress point at the horizontal axis in Figure 6.9. The normal and shear stress increase with decreasing fault dip angle following the Mohr circle.

Figure 6.9 also shows that the stress path of the considered point on the fault plane is dependent on the dip angle. Considering the stress paths for a fault dip angle of 50, 65 and 80 degrees and a Poisson's ratio of 0.05, it is seen that both the direction of the stress path and the magnitude of the stress change are impacted by the dip angle. This results in the finding that no onset of fault slip is calculated up to 30 MPa depletion for any value of Poisson's ratio between 0.05 and 0.45 and a fault dip angle of 80 degrees or larger (and under the Base-case assumptions of all other modelling parameters).

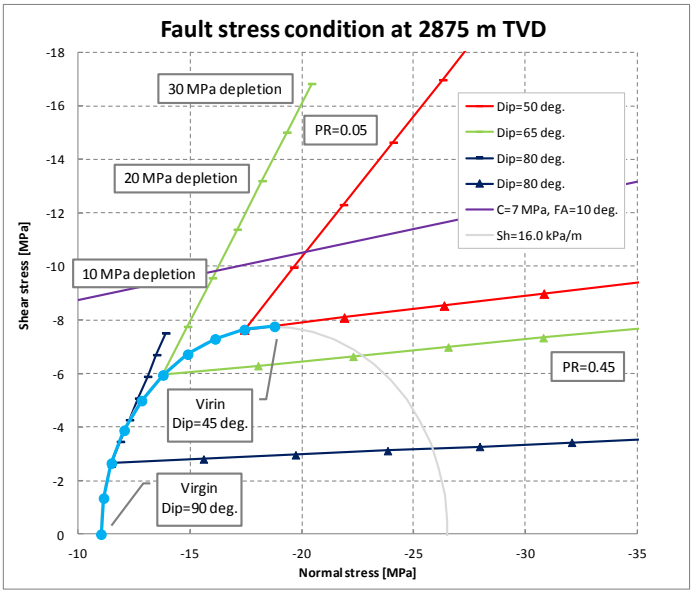

Figure 6.9: **The fault dip angle determines the position of the virgin stress on the Mohr circle, and influences the stress path due to reservoir depletion. The markers on the blue line indicate the virgin stress for a fault dip angle between 45 and 90 degrees (with the horizontal) in increments of 5 degrees. Stress paths are shown for a Poisson's ratio of 0.05 and 0.45 and a fault dip angle of 50, 65 and 80 degrees.**

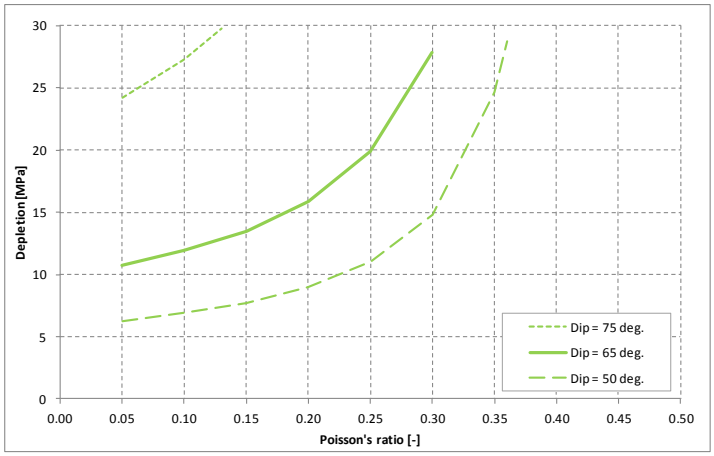

Figure 6.10: Reservoir depletion pressure [MPa] at the onset of fault slip as a function of Poisson's ratio (PR) [-] for different values for the fault dip angle (no formation offset). Total minimum horizontal stress is 16.0 kPa/m.

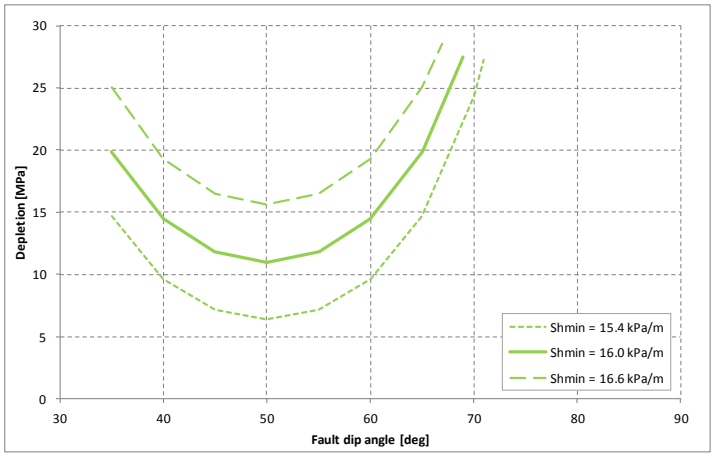

Figure 6.11: Reservoir depletion pressure [MPa] at the onset of fault slip as a function of the fault dip angle [deg] for different values for the total virgin minimum horizontal stress gradient (no formation offset).

Figure 6.10 and Figure 6.11 show the impact of the fault dip angle, the total minimum horizontal stress and Poisson's ratio on the onset of fault slip. The solid lines represent the Base case. The relationships show that faults steeper than 70 degrees are stable up to extremely high reservoir depletion levels, even under a low horizontal in-situ stress scenario and assuming an extremely low values for Poisson's ratio. This suggests that other modelling aspects play a role than the ones assessed in this chapter, if onset of slip is to be simulated for faults with a dip angle between 70 and 80 degrees as is the case in the Groningen field.

6.4. Summary of the findings

The impact of the following parameters on the onset of fault slip in a formation without offset can be quantified using a Mohr-circle evaluation:

- Fault Cohesion
- Fault Friction angle
- Fault dip angle
- Fault dip azimuth
- Poisson's ratio (of the depleting formation),
- minimum horizontal in-situ stress

Young's modulus is the only evaluated parameter thus far that has no influence on the onset of fault slip, except when stiffness or depletion contrasts across the fault are considered. The impact of these parameters on the onset of fault slip can be quantified using a Mohr-circle evaluation.

For the Base-case parameters used in the current study, which represent the conditions in the Groningen field, it is found that no onset of fault slip is calculated up to 30 MPa depletion for any value of Poisson's ratio between 0.05 and 0.45 and a fault dip angle of 80 degrees or larger. Cohesion and friction angle can be adjusted (calibrated) to better reflect actual field observations.

Furthermore, it is concluded that a different slip responses can be simulated starting at the same reservoir depletion level by varying the fault friction angle and adjusting the fault cohesion.

7. Influence of formation offset

So far, cases have been analysed with a uniformly depleting reservoir formation that is intersected by a fault without throw. In this chapter, the influence of formation offset is evaluated. The results of this chapter have been reported as part of the Winningsplan 2013 submission to the Dutch Ministry [23]. The cases evaluated differ from the Base case on one point: the fault dip azimuth is 240 degrees instead of 250 degrees with Northing. Therefore, dip azimuth makes an angle of 80 degrees instead of 90 degrees with the maximum horizontal in-situ stress. As a consequence, onset of fault slip is calculated at slightly larger reservoir depletion pressure compared to the Base case described in Chapter 2.

In section 7.1, the results are discussed in detail for the case with a (downwards) throw of 80 meter. The results comprise of the calculated effective normal and shear stress, the Shear Capacity Utilisation (SCU) and the Relative Shear Displacement (RSD) along the fault plane as a function of depth and depletion level. Furthermore, the total length of the slip patches, the maximum RSD and the energy dissipated by fault slip are discussed. Similar results for 215 and 440 meter throw are reported in Appendix 4.

Subsequently, the impact of reservoir formation offset on the onset of fault slip is discussed in section 7.2, on the total length of the slip patch in section 7.3, on the maximum RSD in section 7.4, and on the dissipated energy by fault slip in section 7.5. The results are summarised in section 7.6.

7.1. Results for 80 m formation offset

Figure 7.1a shows the applied pore pressure profile as a function of depth for 10, 20, 25 and 30 MPa (100, 200, 250 and 300 bar) reservoir depletion. The location of the interfaces between formation layers 1, 2, 3 and 4 on both sides of the fault are indicated by horizontal (green and blue) marker lines. The gas gradient in the reservoir formations is recognisably steeper than the water gradients in over- and underburden.

Figure 7.1b shows the Relative Shear Displacement (RSD) along the fault plane as a function of depth for the same depletion levels. Negative values indicate that the left-hand side of the fault is displaced downwards relative to the right-hand side of the fault. For a throw of 80m a maximum RSD of 0.25 meter is calculated after 30 MPa reservoir depletion.

Figure 7.1c shows the effective normal and shear stress distribution and Figure 7.1d shows the derived Shear Capacity Utilisation (SCU) as a function of depth. This is the ratio of the actual shear stress τ and the shear stress carrying capacity τ_{max} according to a Coulomb friction law (see section 2.5). A SCU of 1 means that the shear stress carrying capacity has been reached and that the fault is slipping. Values larger than 1 are not possible, because the carrying capacity cannot be exceeded. The interface elements for which SCU=1 is defined as the slip patch.

Two slip patches initiate at 6.3 MPa reservoir depletion (onset of fault slip): one at the top of the depleting reservoir in the hanging wall (left-hand side) and one at the bottom in the foot wall (right-hand side of the fault). This is seen by the yellow line in Figure 7.1d representing the SCU distribution after 10 MPa depletion, showing a SCU of 1 at these locations and lower values elsewhere. The orange line representing the SCU distribution after 20 MPa depletion shows one much larger slip patch. The merging of the two slip patches occurs after 12 MPa depletion.

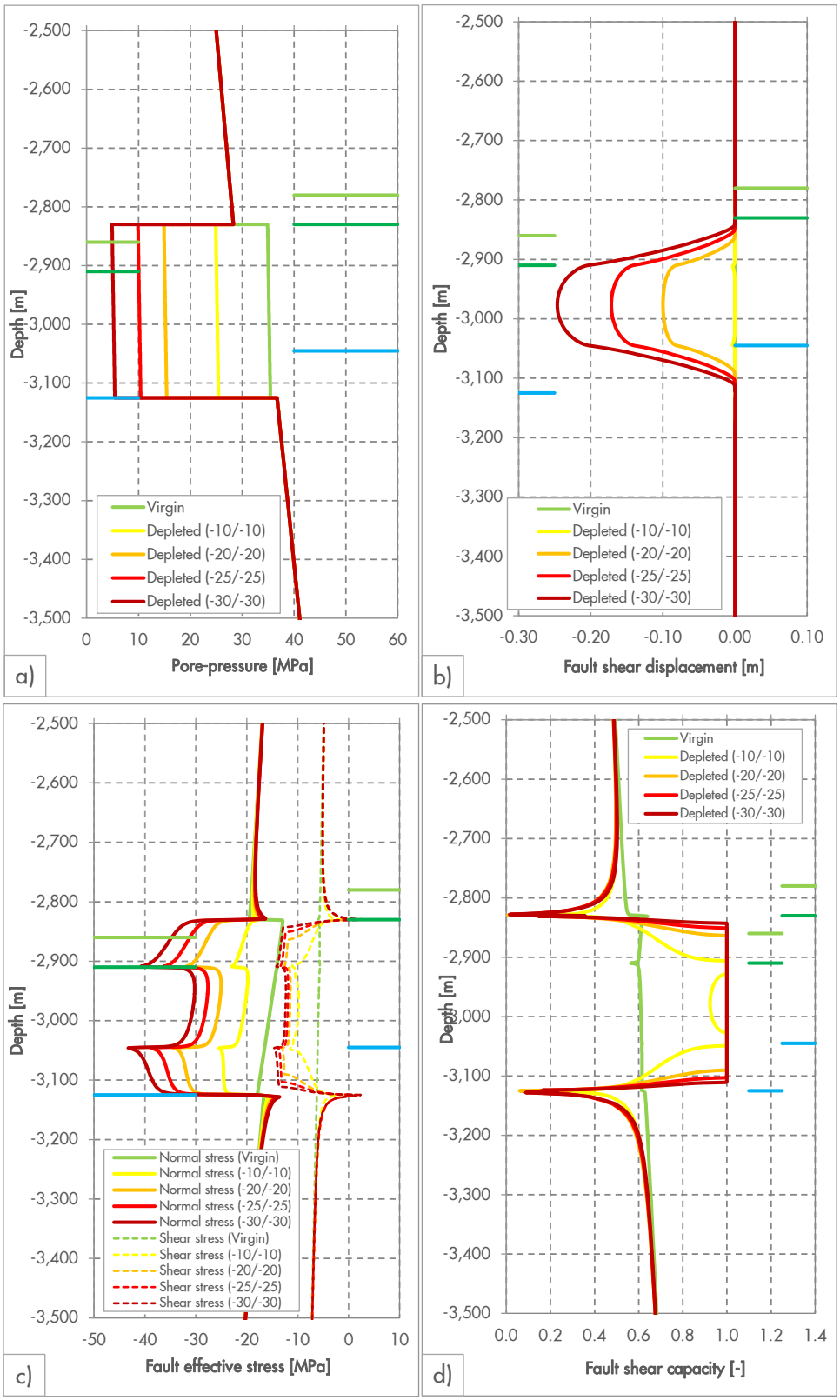

Figure 7.1: **a) Pore pressure, b) Relative Shear Displacement (RSD), c) Effective normal and shear stress, and d) the Shear Capacity Utilisation as a function of the depth for a throw of 80 meter, under virgin and 10, 20, 25 and 30 MPa depletion conditions.**

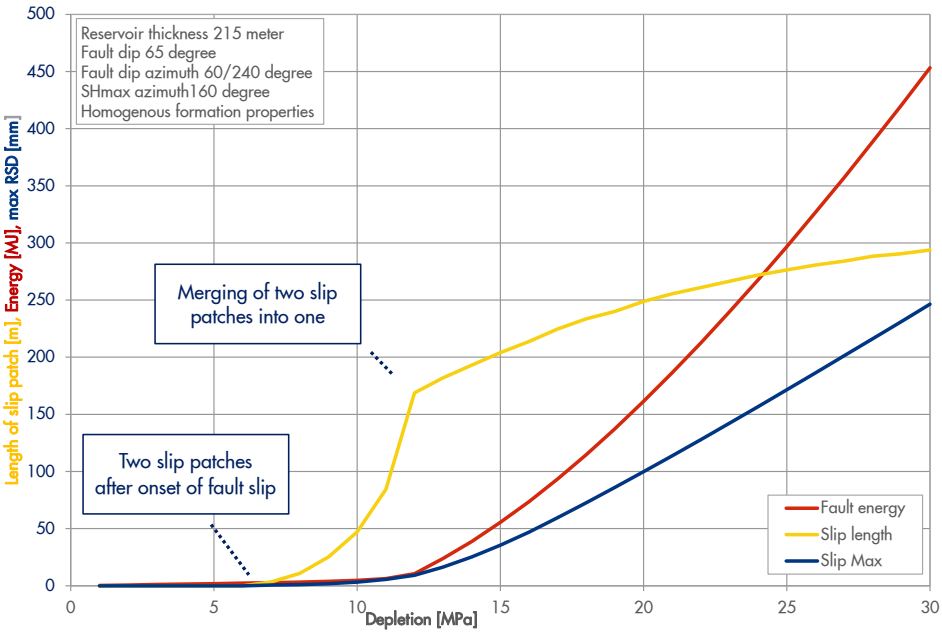

Figure 7.2: Dissipated energy by fault slip [MJ], the total length of the slip patch [m] and the maximum (absolute) RSD [mm] as a function of depletion level for a formation offset of 80 m

The yellow line in Figure 7.2 shows that the development of the slip patch length accelerates until the two slip patches merge after 12 MPa depletion. The slip length is 169m at this depletion level, which is less than the reservoir thickness of 215 m. The growth of the slip patch length is significantly slower upon further depletion, reaching 294m after 30 MPa reservoir depletion.

The blue line in Figure 7.2 shows that the development of the Relative Shear Displacement (RSD) remains limited until the two slip patches merge into one at 12 MPa depletion, and develops more quickly upon further reservoir depletion. The RSD reaches 0.25m after 30 MPa depletion.

The red line in Figure 7.2 represents the energy dissipated by fault slip, and is calculated as the product of the shear stress, the slip displacement and the area of each interface element. The onset of fault slip at 6.3 MPa depletion is not recognisable from the dissipated energy in Figure 7.2, while the merging of the two slip sections is. The acceleration after the merging of the two slip patches is more pronounced than for the RSD. Furthermore, it is noted that the energy stored in the fault up to onset of slip is elastic and recoverable, whereas the incremental energy in the fault dissipated after onset of slip is not. It is seen that the dissipated energy level remains limited as long as two slip sections exist.

7.2. Onset of fault slip

Similar results have been evaluated for about 40 analyses with offset increments of 20 meter between -300 m (up-thrown) and +500 m. The results for 215 and 440 meter formation offset are found in Appendix 4, while the case of no offset is discussed in Chapter 3. The impact of formation offset on the onset of fault slip is shown in Figure 7.3. The depletion level is calculated by interpolation between depletion step results. It is seen that a fault without reservoir offset allows the largest depletion level at the onset of fault slip, namely 21.5 MPa, whereas a fault with an offset about equal to the reservoir thickness (215 m in this case) allows the smallest depletion level (3.6 MPa). A slightly higher depletion level at the onset of fault slip is calculated compared to the Base discussed in Chapter 3, because the fault dip azimuth is less than 80 degrees instead of 90 degrees with the maximum horizontal in-situ stress.

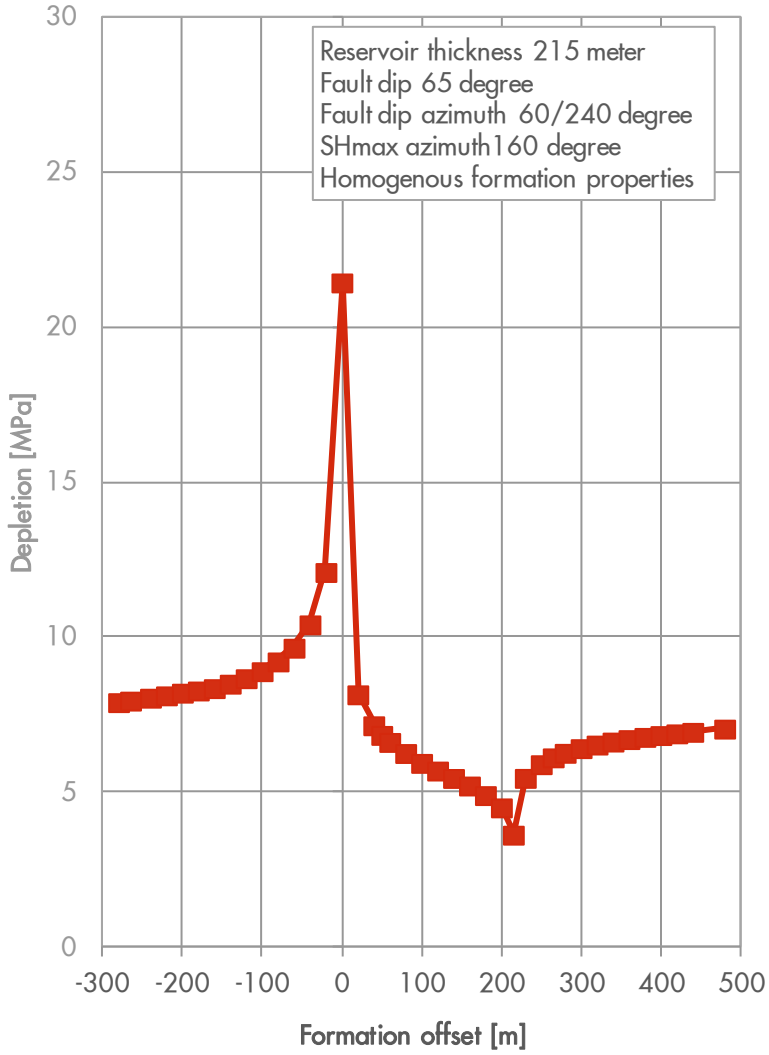

Figure 7.3: **Reservoir depletion pressure [MPa] at the onset of fault slip as a function of formation offset [m]**

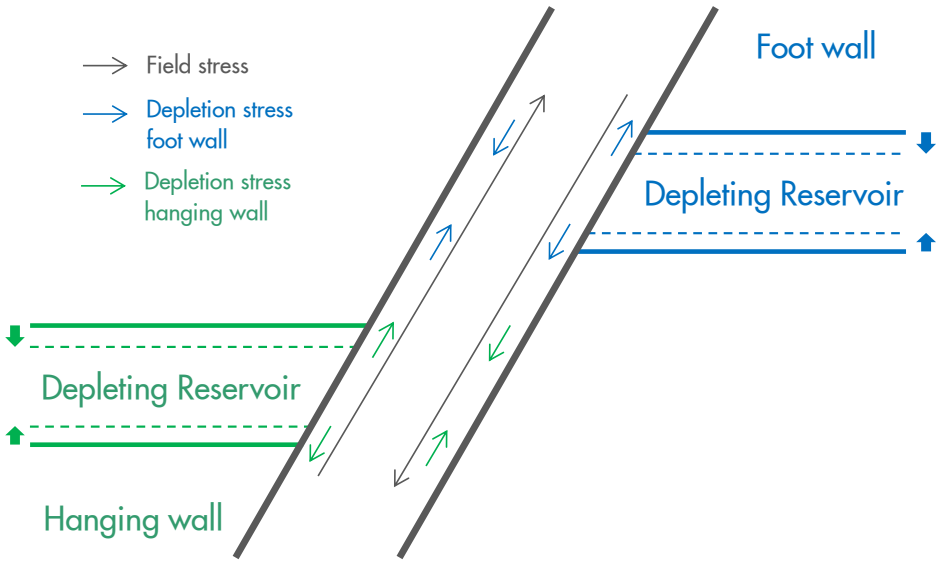

Figure 7.4: **Direction of shear stress exerted on the formation on each side of the fault plane due to depletion of the reservoir units in the footwall and hanging wall and in relation to the shear stress present in a normal faulting environment.**

The impact of formation offset can be explained by means of the shear stress induced by depletion of the two reservoir units separately (Figure 7.4). Here, a normal faulting environment is assumed, which determines the downwards direction of the tectonic shear stress acting on the foot wall. Considering depletion in the foot wall, it is seen that the induced stress change exerted at the top of the depleting reservoir formation acts in opposite direction from the tectonic stress and in the same direction at the bottom of the reservoir formation (see Figure 4.5, in section 4.1.2). Considering depletion in the hanging wall, it is found that induced shear stress acts in the same direction as the tectonic stress at the top of the reservoir and in opposite direction at the bottom of the reservoir unit (see Figure 4.6, in section 4.1.2). It is highlighted that the direction of the induced shear stress acts in opposite direction on the formations on the opposite side of the depleting reservoir units. Furthermore, it is noted that incremental stress changes should be superposed in case of depletion in the foot wall and the hanging wall reservoir units.

Consequently, both the shear stress level and the SCU reduce at the top of the foot wall reservoir and at the bottom of the hanging wall reservoir upon depletion. This is seen for 80 meter formation offset in Figure 7.1c and Figure 7.1d, but is much clearer for larger offsets (Appendix 3). Reservoir depletion may even flip the shear stress direction and cause the SCU to reach 1 to trigger slip in opposite direction.

Consider the induced shear stress in the case that the formation offset is equal to the reservoir thickness. Super-position of the shear stress components acting on the foot wall shows that the tectonic shear stress at the bottom of foot wall is increased by downward contributions from both reservoir units. This explains why the lowest reservoir depletion pressure is required to cause the onset of fault slip at a formation offset equal to the reservoir thickness.

Considering the shear stress in case of zero formation offset, it is found that the shear stress induced at the top and bottom of the reservoir units are neutralised. This neutralisation may be partial if the depletion, reservoir thickness or compressibility (Young's modulus) on both sides of the fault is unequal. This explains why the highest reservoir depletion pressure before slip is found at zero formation offset.

Furthermore, Figure 7.3 shows that extremely large positive or negative offsets converge to the same depletion level for the onset of slip. In these cases, the distance between the depleting reservoir formations on either side of the fault is so large that the stress change induced by depletion in one unit is not interfering with the stress change induced by the other unit. This implies that these cases describe a fault configuration with depletion on one side of the fault only, as discussed in section 4.1.

7.3. Total length of the slip patch

The development of the total slip patch length with increasing reservoir depletion is plotted in Figure 7.5 for the cases of 0, 80, 215 and 440 m formation offset. The total length of the slip patch is calculated as the total length of all interface elements with a SCU of 1 and may include more than one slip patch. The total length of the slip patch develops rapidly after the onset at 21.5 MPa depletion in the absence of offset, while the slip patch grows gradually starting after about 3.6 MPa depletion in the case of 215 m offset. These two cases feature only one slip patch that initiates at the top of the down-thrown block, which coincides with the bottom of the hanging wall. The case of 80 m formation offset, shown in detail in Figure 7.1, features two slip patches up to 12 MPa depletion when both merge into a single slip patch. From Figure 7.5, it is seen that the growths of the two slip patches accelerate with depletion, until they merge and continue to grow at a slower pace afterwards. A similar fault slip process is found for a formation offset larger than the thickness of the depleting reservoir formation, in which also two slip patches appear after the onset of fault slip and that merge into a one larger patch upon further reservoir depletion.

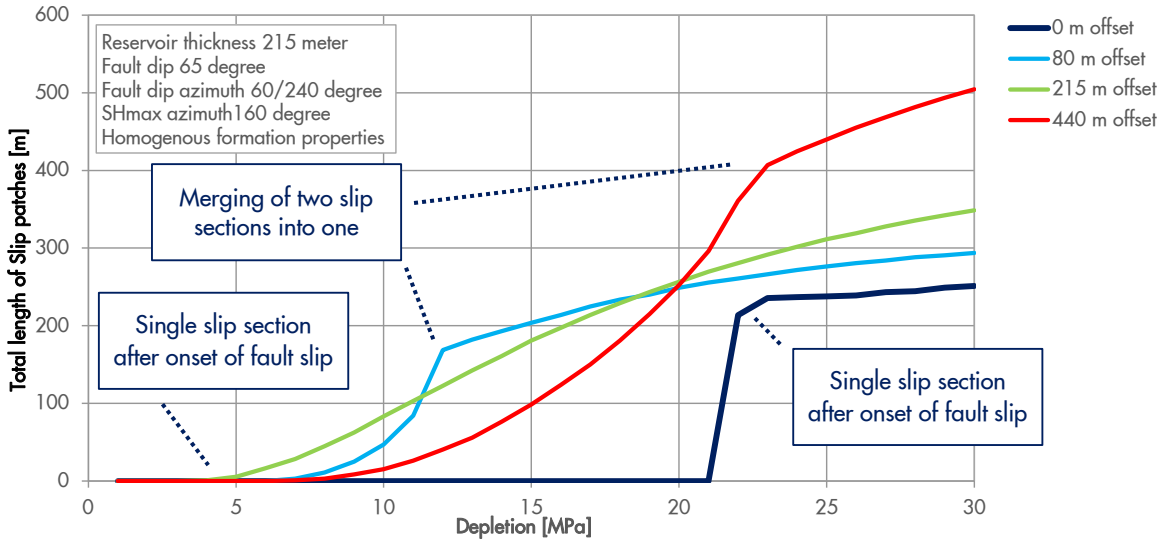

Figure 7.5: Development of the slip patch [m] as function of the depletion level for different values of the vertical offset along the fault plane

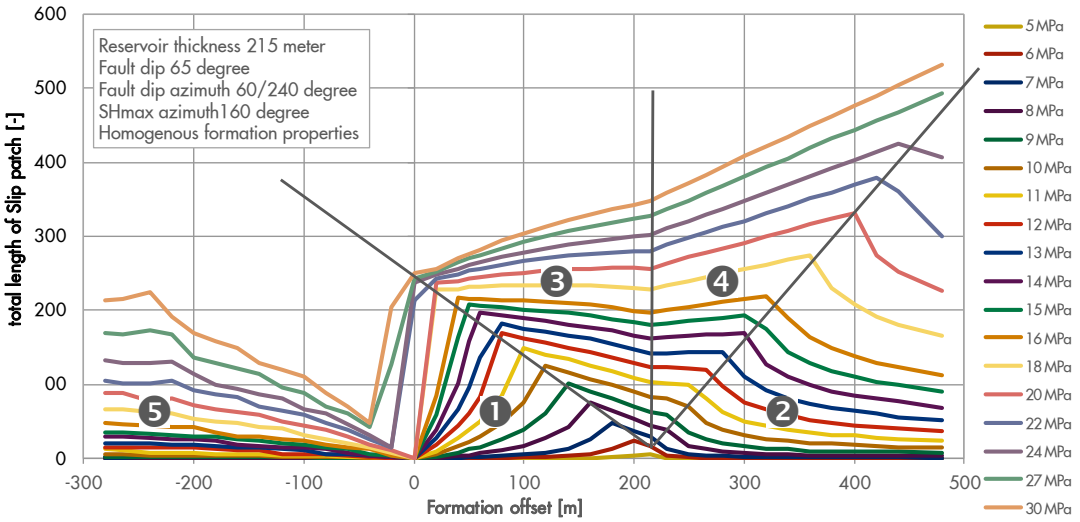

Figure 7.6: Total slip length of slip sections as a function of throw and reservoir depletion

Figure 7.6 shows the total slip length of the slip patches for various depletion levels (starting at 5 MPa) and a throw between -300 and +500 m. Three fault slip conditions can be identified based on throw and depletion level:

1. Two slip patches are found in case of a positive reservoir offset and under low to moderate depletion levels, labelled (1) and (2).
2. A single, merged fault slip patch is found in case of a positive reservoir offset and under elevated depletion levels, labelled (3) and (4).
3. Two slip patches that do not merge even under elevated reservoir pressure in case of a negative reservoir offset, labelled (5).

The merging of the two slip patches into one is dependent on the formation offset along the fault. The transition from slip condition (1) with two slip patches into slip condition (3) with one slip patch is somewhat different for a throw smaller than the depleting formation thickness (215 m in this case) than the transition from slip condition (2) to (4) for larger throws. In the last case, the slip patch length growths more rapidly with depletion. This is also seen in Figure 7.5, in which the merged slip section for a throw of 440 meter increases faster (after 23 MPa depletion) compared to the case of a throw of 80 m (depletion larger than 12 MPa).

7.4. Maximum Relative Shear Displacement

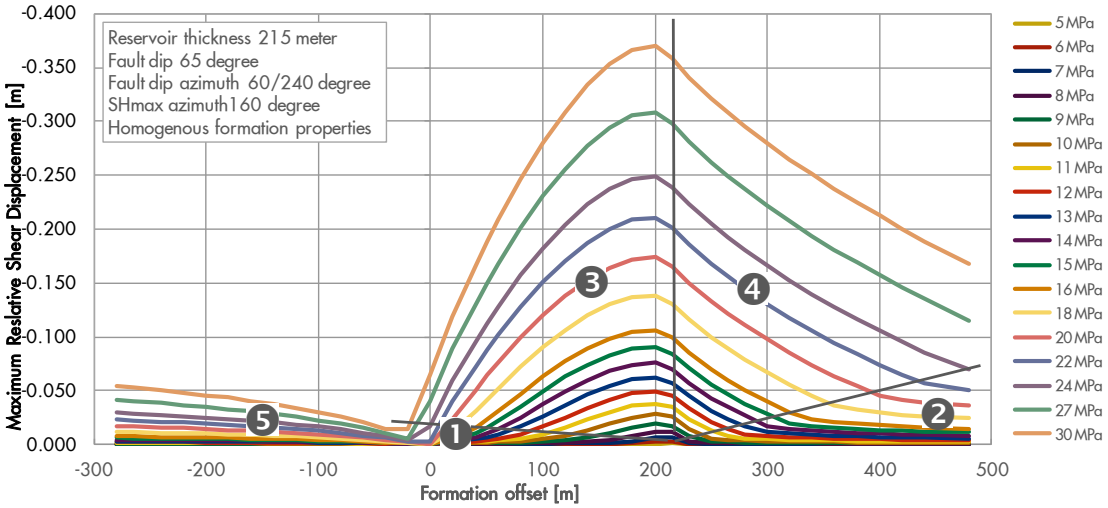

Figure 7.7: Maximum Relative Shear Displacement [m] as a function of throw and reservoir depletion

The maximum Relative Shear Displacement (RSD, Figure 7.7) shows an extreme value at an offset somewhat smaller than the depleting formation thickness for all depletion levels. The five different fault slip conditions indicated in the figure, highlight that the RSD accelerates with depletion after the slip sections have merged. This is the case in particular for offsets smaller than the thickness of the depleting reservoir: the maximum RSD in slip condition (1) is smaller than in condition (2) under the same depletion level, while the maximum RSD in (3) is comparable to larger than in (4).

In summary, it is seen that fault configurations with a throw smaller than the thickness of the depleting reservoir formation develop a larger slip displacement over a shorter slip length than configurations with an offset larger than the thickness of the depleting reservoir formation.

7.5. Dissipated energy by fault slip

The five different fault slip conditions indicated in Figure 7.8 highlight the limited energy dissipation for conditions (1), (2) and also condition (5). It is also seen that the energy dissipation is substantially larger in slip condition (2) for offsets larger than the thickness of the depleting reservoir than in slip condition (1). In both cases, (1) and (2), the energy dissipated by fault slip becomes more significant when the two slip sections have merge into one slip section, indicated by the labels (3) and (4) in the figure. It is seen that most energy is dissipated in slip condition (3), which is in general characterised by the larger RSD and a smaller slip section length than in slip condition (4).

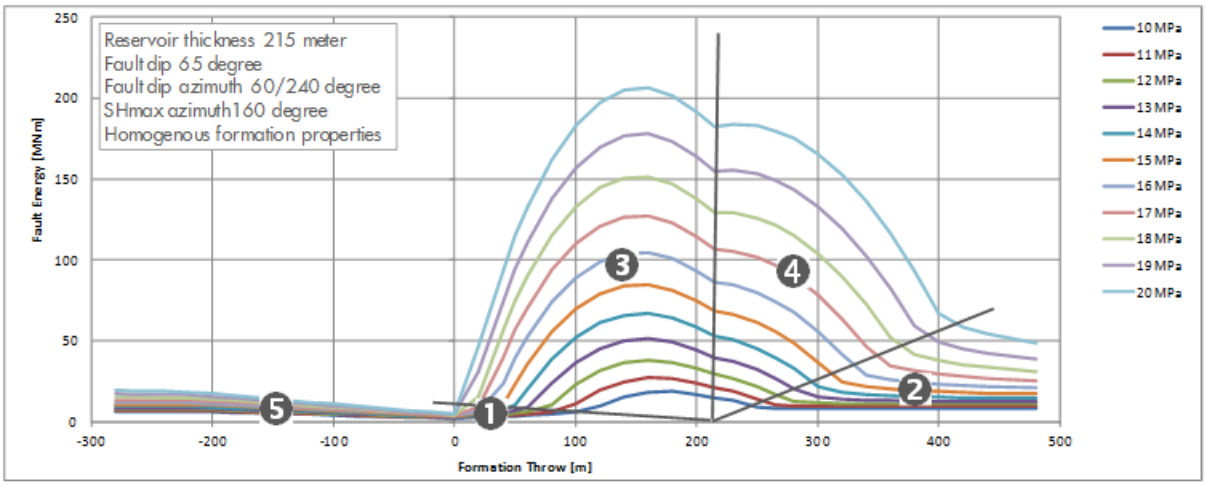

Figure 7.8: Fault energy dissipated by fault slip as a function of throw and depletion level

7.6. Interpretation of the results

In the previous sections, different fault slip geometries are identified based on fault throw and depletion level under the assumptions given in Chapter 2. It is found that offset of depleting reservoir formations along existing faults highly impacts the geomechanical response in terms of

- The depletion level at the onset of fault slip
- The number of slip patches
- The total length of the slip sections
- The maximum Relative Shear Displacement
- The dissipated energy by fault slip.

The following cases can be identified in terms of fault throw:

1. The down-thrown block has an offset smaller than the thickness of the depleting reservoir formation
2. The down-thrown block has an offset larger than the thickness of the depleting reservoir formation
3. Up-thrown blocks.

With two exceptions, fault slip starts with two slip patches at a relatively low depletion level in all three cases. The difference is found in the merging of the two slip patches at an elevated depletion level for cases 1 and 2, which is not found for the evaluated condition in case 3. The merging of the two slip patches has different characteristics in Case 1 than in Case 2. Generally, in Case 2 a smaller slip displacement is developed over a larger slip length compared to Case 1. Also, the energy dissipation shows differences. The two slip patches in Case 2 dissipate more energy than the two slip sections in Case 1 under the same depletion level, while this is the other way around for most throws in after the merging of the two patches. So, in general, more energy is dissipated by fault slip in the transition from condition (1) to (3) than from (2) to (4) (Figure 7.8).

There are two exceptions, in which a single (merged) slip patch occurs directly after the onset of fault slip, namely

1. No formation offset: a single slip patch is calculated over the entire height of the depleting reservoir formation just after the onset of fault slip.
2. The throw is equal to the thickness of the depleting reservoir formation, in which the slip patch increases gradually with depletion at the location where the two depleting formations connect.

These two exceptions also provide the upper and lower limit of allowable depletion at the onset of fault slip. Exception case 1 allows the highest depletion level at the onset of fault slip, while Exception case 2 allows the lowest depletion level. Hence, onset of fault slip is found to be strongly dependent on throw.

The development of the slip patch after the onset of fault slip under the current modelling assumptions, occurs most gradually with depletion for a fault throw equal to the thickness of the depleting reservoir formation. For all other cases with down-thrown reservoir blocks, the development of the slip patch accelerates with depletion until the two sections merge into a single slip patch (Figure 7.5). In the extreme case, in the absence of throw, the slip patch develops abruptly at the onset of fault slip. So, two extreme cases exist: one in which the fault slip patch develops gradually with depletion starting at a low depletion level and one in which fault slip occurs abruptly over the thickness of the depleting formation at an elevated depletion level.

The assumption of ideal plastic fault slip behaviour causes a stable propagation of the slip patches in all cases evaluated so far. Faults without throw show the most rapid development of the slip patch, but also in this case a stable equilibrium condition is found. Stable equilibrium means that no alternative deformation mode is possible (slip condition) at a lower (potential) energy level. This implies that incremental reservoir depletion is required to propagate the slip patch assuming and, as a result of the time-scale of this process in the field, that this occurs in an a-seismic fashion. So, it is found that an ideal plastic fault slip model in combination with the evaluated fault configurations do not lead to seismogenic fault slip.

The current results are in line with work reported earlier [5][6]. The calculated Relative Shear Displacement (RSD) shows a similar distribution as a function of depth, various formation offset levels are recognised, and the maximum RSD is in the same range (between 0.15 and 0.20 m [5]). This study provides a more comprehensive insight in the development of merged slip patches at elevated depletion levels and their dependence on formation offset. Furthermore, a relationship is developed between reservoir depletion, formation offset, number of slip patches and the total length of the slip patch, the maximum RSD and the dissipated energy.

7.7. Summary of the findings

In this chapter it is found that

- The offset along the fault plane of a depleting formation strongly determines the onset of fault slip.
    - An offset equal to the reservoir thickness requires the least reservoir depletion to trigger onset of fault slip
    - No reservoir offset requires the largest depletion to trigger onset of fault slip
    - reservoir depletion at a single side of a fault does not constitute the worst possible scenario for triggering onset of fault slip.
- The fault slip response in terms of length of the slip patch, RSD and dissipated energy is dependent on the formation offset. Three scenarios of slip response can be recognised:
    - formation offset smaller than the thickness of the depleting reservoir
    - formation offset larger than the thickness of the depleting reservoir
    - up-thrown blocks
- Merging of two slip patches does not lead to unstable equilibrium conditions if an ideal plastic slip law is used in the interface elements.
    - Unstable equilibrium could be a potential indicator for seismic slip response
- The depletion at the onset of fault slip and the maximum RSD are in line with those reported earlier [5][6].

8. Influence of reservoir thickness

The influence of reservoir thickness on compaction and subsidence of depleting fields is well known. The impact of reservoir thickness on the stress distribution in the subsurface that is essential in the assessment of fault slip is less well known and is investigated in this chapter.

The same series of analysis that are described in Chapter 7 have also been executed for a reservoir thickness of 165 m and 265 m. This is approximately the thickness range of the depleting reservoir formations across the Groningen field. The evaluations in the previous chapter represent a mid-case scenario with a reservoir thickness of 215 m. The offset for formation Layer 3 on the left-hand side of the fault have been varied between -300 meter (up-thrown) and +600 m (down-thrown). All other parameters have been taken as specified in Chapter 2, except that the fault dip azimuth is 240 degrees instead of 250 degrees with Northing and, therefore less than 80 degrees instead of 90 degrees with the maximum horizontal in-situ stress. Fault dip angle of 65 degrees is also the same as in the Base case.

In the next sections, the influence of the thickness of the depleting formation on the onset of fault slip, the total length of the slip patches, the maximum Relative Shear Displacement (RSD) and the dissipated energy by fault slip are presented. Various parameters are divided by (normalised for) the reservoir thickness to facilitate comparison.

8.1. Onset of fault slip

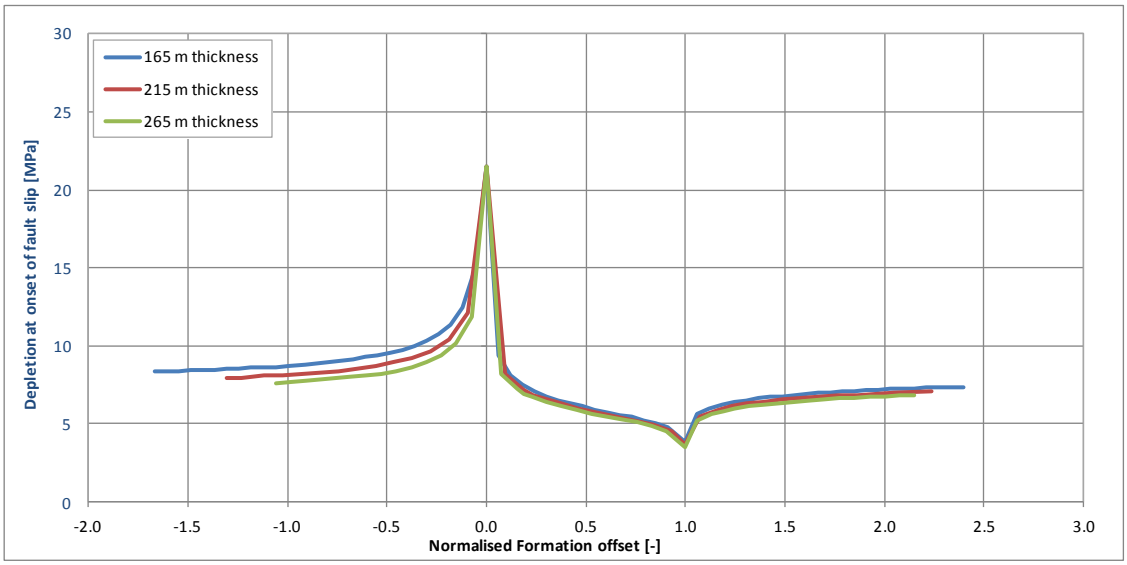

Figure 8.1: Reservoir depletion pressure [MPa] at the onset of fault slip as a function of normalised formation offset [-].

Figure 8.1 shows that the onset of fault slip is only marginally influenced by the reservoir thickness. It is noted that the formation offset, which is plotted on the horizontal axis, is normalised for the reservoir thickness. The depletion level at which onset of fault slip occurs is the same for 165m, 215m and 265m reservoir thickness in the absence of formation offset, namely 21.5 MPa (215 bar) depletion. The onset of fault slip is calculated after 3.8, 3.6 and 3.5 MPa depletion if the normalised formation offset is 1 and the reservoir thickness is 165 m, 215 m and 265 m respectively. In general, it is seen that the depletion level that the calculated onset of fault slip occurs at slightly lower depletion level with increasing reservoir thickness. However, the differences are not meaningful and may be caused by the inability of the finite-element discretisation to capture the peak stress at the interfaces between the depleting and non-depleting formations. See section 4.3.

8.2. Total length of the slip patch

The development of the total length of the slip patch as a function of reservoir depletion is plotted in Figure 8.2 in case of a reservoir thickness of 165 m, 215 m and 265 m. The absolute reservoir formation offset is different for the three cases, but the normalised offset is the same, namely 1. In this case only one slip patch develops at the onset of fault slip (about 3.6 MPa). In Figure 8.2, the length of the slip patch is divided by the applicable reservoir thickness. It is seen that the development of the total length of the slip path is very similar *after* the onset of fault slip.

Figure 8.3 shows the total length of the slip patches at 30 MPa depletion and for a normalised formation offset between -1.5 and 2.0. A normalised offset of 2.0 implies a formation offset that is twice the thickness of the depleting reservoir, whereas a negative normalised formation offset refers to up-thrown blocks. The red arrow in Figure 8.3 refers to the results shown in Figure 8.2 for a normalised offset of 1.0. The red arrow in Figure 8.2 refers to the results shown in Figure 8.3 for a depletion of 30 MPa. It is found that the normalised total length of the slip patches is identical for the evaluated range of normalised reservoir formation offsets up to 30 MPa depletion.

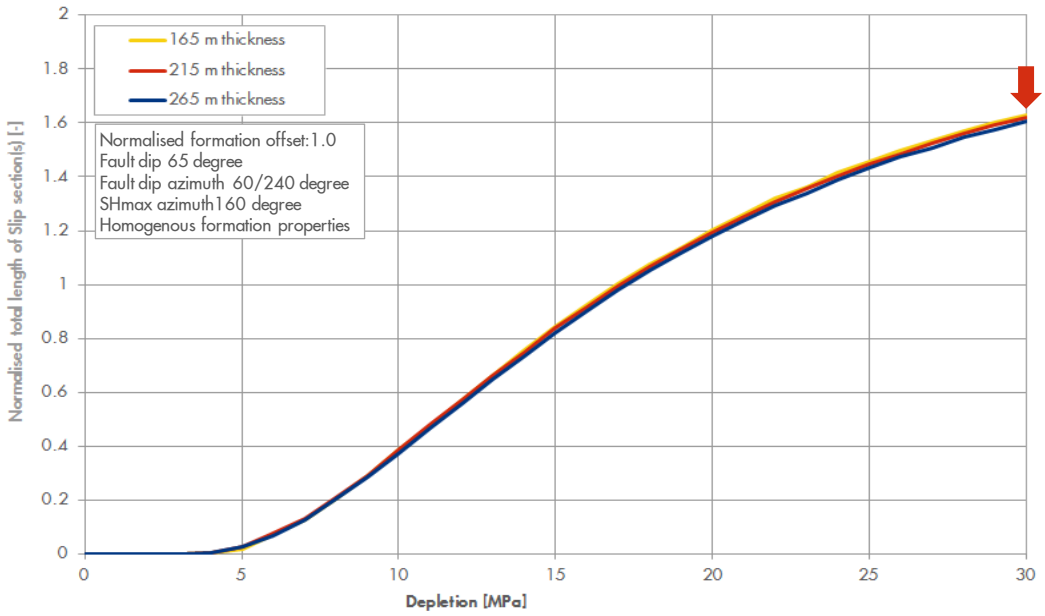

Figure 8.2: Normalised total length of the slip patch along the fault plane [-] as a function of reservoir depletion [MPa] for a the normalised formation offset of 1.0. The red arrow indicates the depletion level plotted in Figure 8.3.

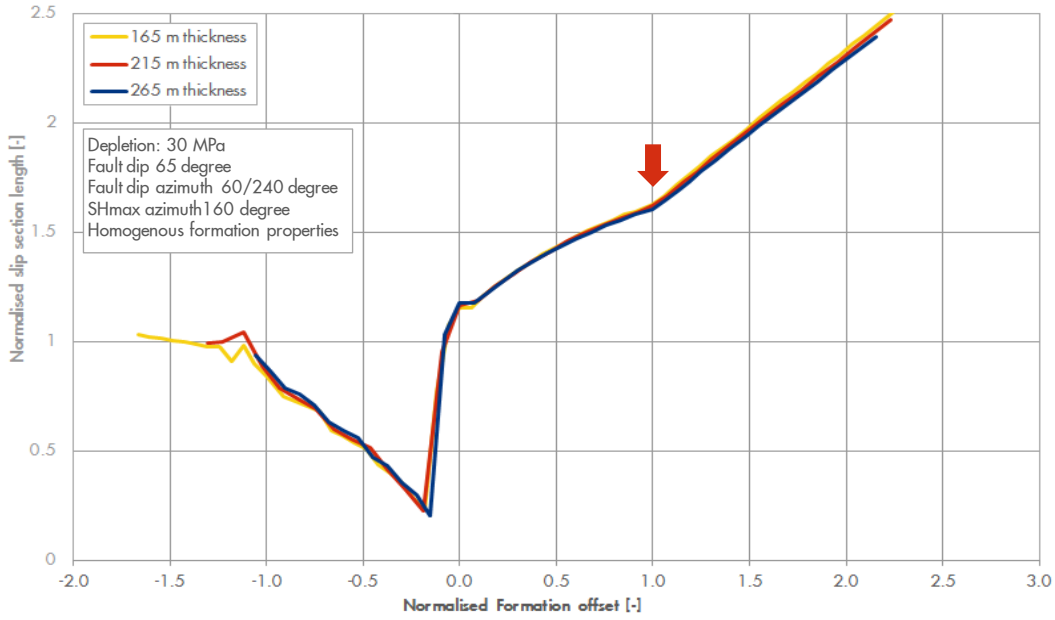

Figure 8.3: **Normalised total length of the slip patch along the fault plane [-] as a function of the normalised formation offset [-] under 30 MPa (300 bar) reservoir depletion. The red arrow indicates the normalised offset plotted in Figure 8.2.**

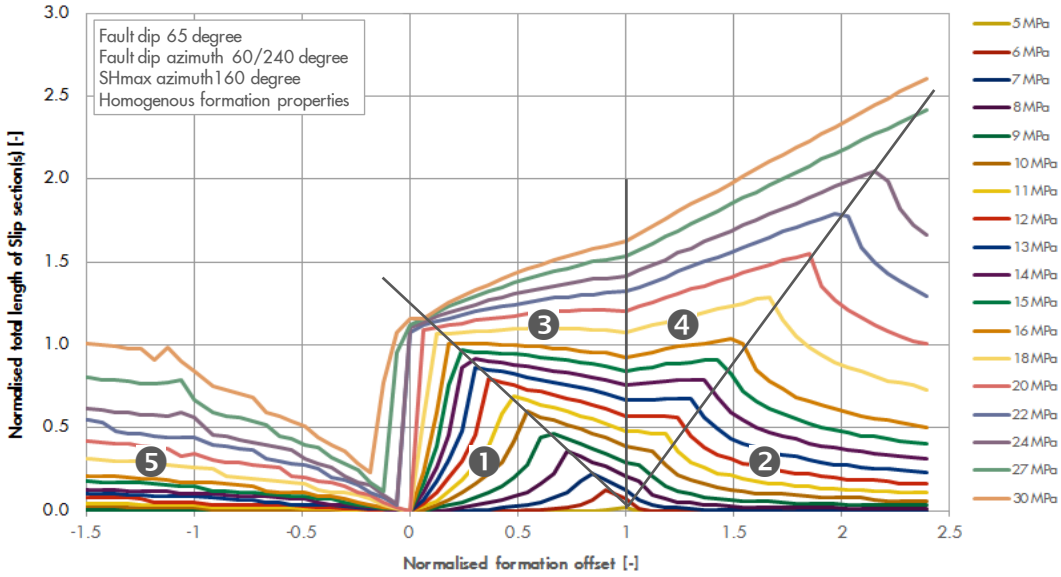

Figure 8.4: **Normalised total length of the slip patch along the fault plane [-] as a function of the normalised formation offset [-] for various depletion levels [MPa]. See section 7.3 for a description of the labels (1) through (5).**

The findings from Figure 8.2 and Figure 8.3 means that the results shown in Figure 7.6 can be generalised for any reservoir thickness by plotting the normalised total length of the slip patches as a function of the normalised formation offset. This is shown in Figure 8.4 for a reservoir depletion between 5 and 30 MPa. The different slip conditions, labelled (1) through (5) is the same as described in section 7.3.

8.3. Maximum Relative Shear Displacement

Figure 8.5 shows the maximum Relative Shear Displacement (RSD) divided by the reservoir thickness of respectively 165 m, 215 m and 265 m as a function of depletion. The results are shown for a normalised formation offset of 1.0. The maximum RSD starts to increase after the onset of fault slip at about 3.6 MPa for all three cases (section 8.1). Figure 8.5 shows that also the development of the normalised maximum RSD as a function of depletion is determined by the normalised formation offset.

The absolute and normalised maximum RSD as a function of normalised formation offset at 30 MPa depletion is shown in Figure 8.6. It is seen that the largest (normalised) maximum RSD is found at the same normalised reservoir formation offset and that its value is about 0.0017 of the reservoir thickness for the conditions used in the current study. The graph with the absolute value of the maximum RSD is added to show the magnitudes in meters for the three different cases.

The finding that the normalised maximum RSD is determined by the normalised formation offset and the depletion level implies that Figure 8.7 is applicable for any reservoir thickness. For the current model (Chapter 2) the maximum RSD remains smaller than 0.002 of the reservoir thickness. The different slip conditions, labelled (1) through (5) is the same as described in section 7.3.

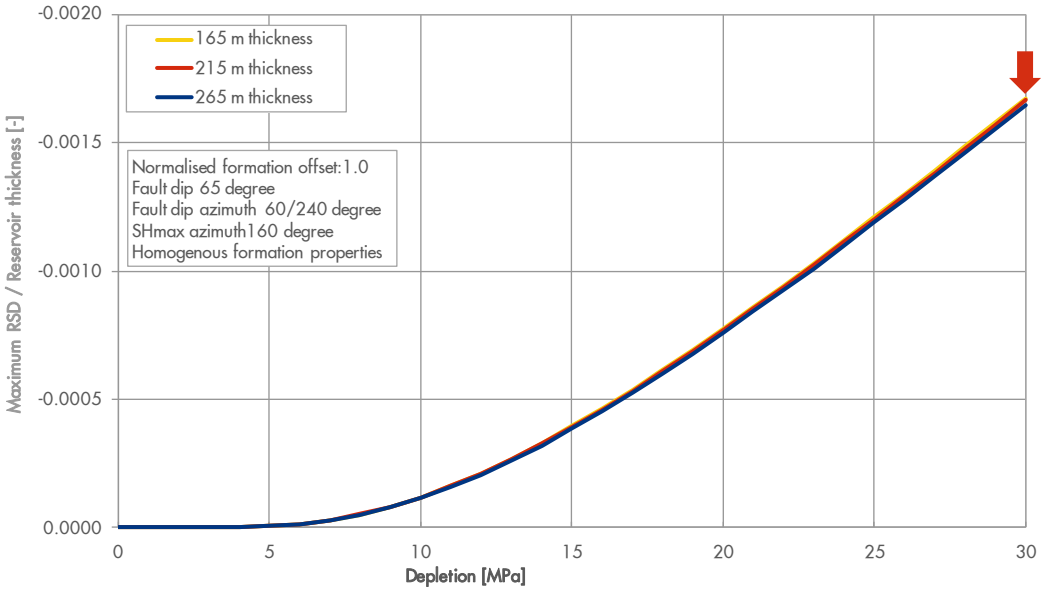

Figure 8.5: Normalised maximum Relative Shear Displacement [-] as a function of reservoir depletion [MPa] for a normalised formation offset of 1.0. The red arrow indicates the depletion level plotted in Figure 8.6.

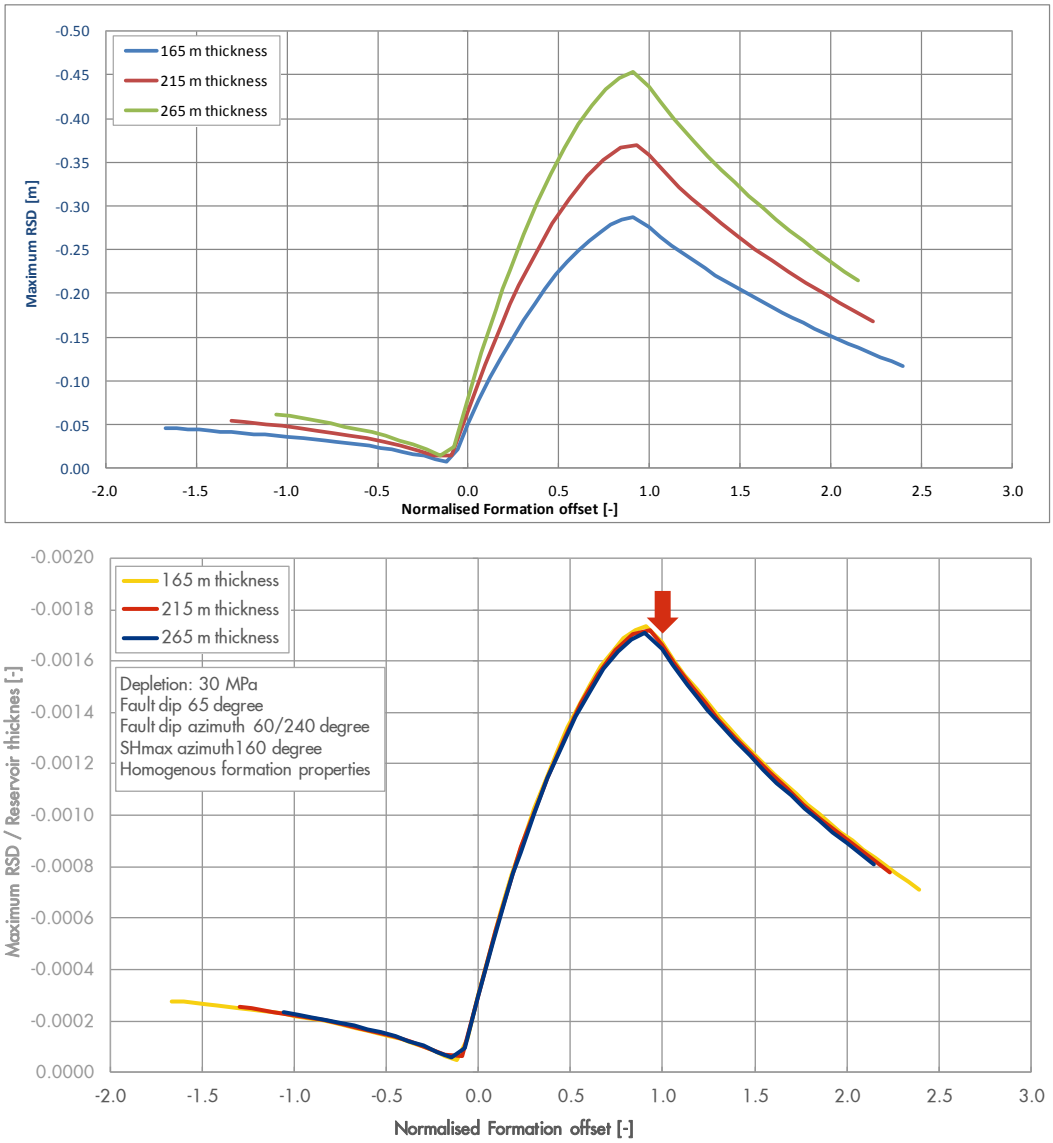

Figure 8.6: **The absolute (top) and normalised (bottom) maximum Relative Shear Displacement as a function of normalised formation offset [-] under 30 MPa (300 bar) reservoir depletion. The red arrow indicates the normalised offset plotted in Figure 8.5.**

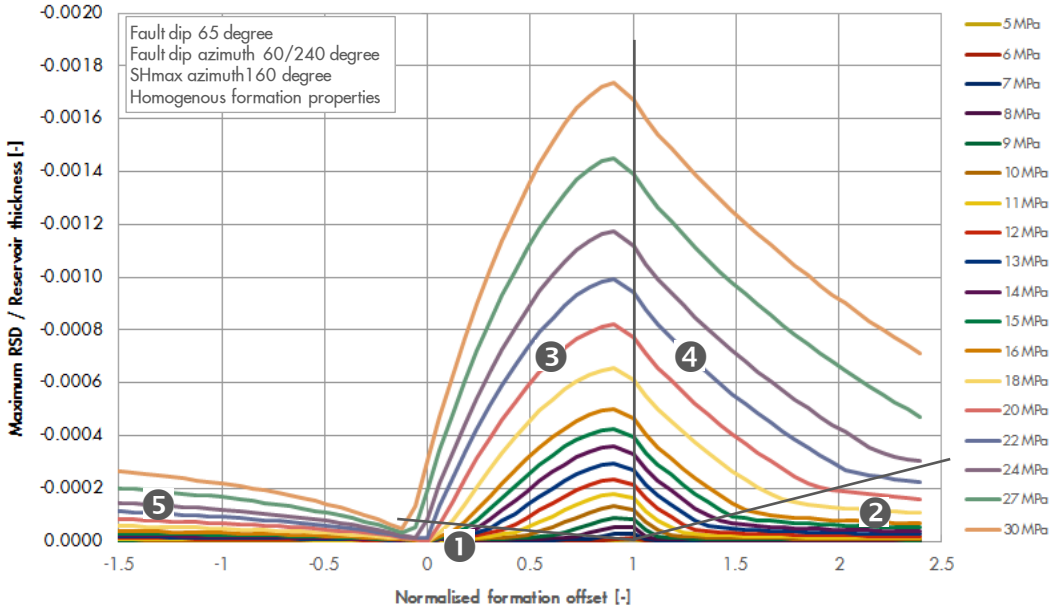

Figure 8.7: Normalised maximum Relative Shear Displacement [-] as a function of normalised formation offset [-] for various depletion levels [MPa]. See section 7.3 for a description of the labels (1) through (5).

8.4. Dissipated energy by fault slip

The dissipated energy by fault slip is calculated as the product of the shear stress, the relative slip displacement (RSD) and the area (length) of the slip patch. The previous sections show that both the RSD and the total length of the slip patches are proportional with the reservoir thickness. This suggests that the dissipated energy by fault slip is proportional with the reservoir thickness to the power two. This is confirmed by Figure 8.8 and Figure 8.9 which show the dissipated energy divided by the square of the reservoir thickness on the vertical axes. It is seen that the dissipated energy normalised for the reservoir thickness of 165, 215 and 265 m is very similar for a given depletion level and normalised formation offset. This implies that Figure 8.9, showing the normalised dissipated energy by fault slip as a function of the normalised formation offset is applicable for any formation thickness.

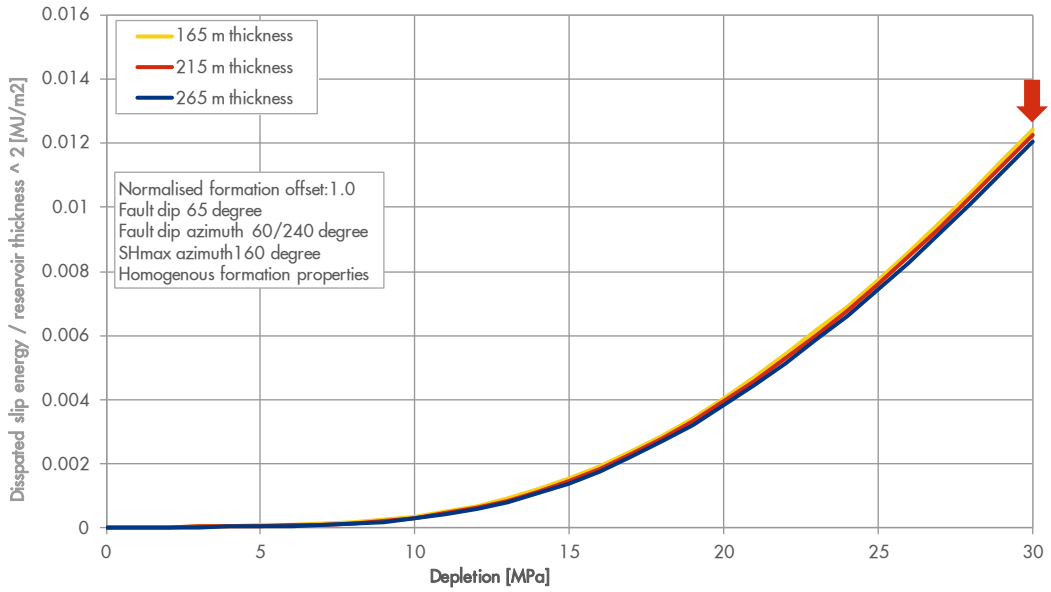

Figure 8.8: **Dissipated fault energy normalised for reservoir thickness [MJ/m²] as a function depletion [MPa] for a normalised formation offset of 1.0. The red arrow indicates the depletion level plotted in Figure 8.9.**

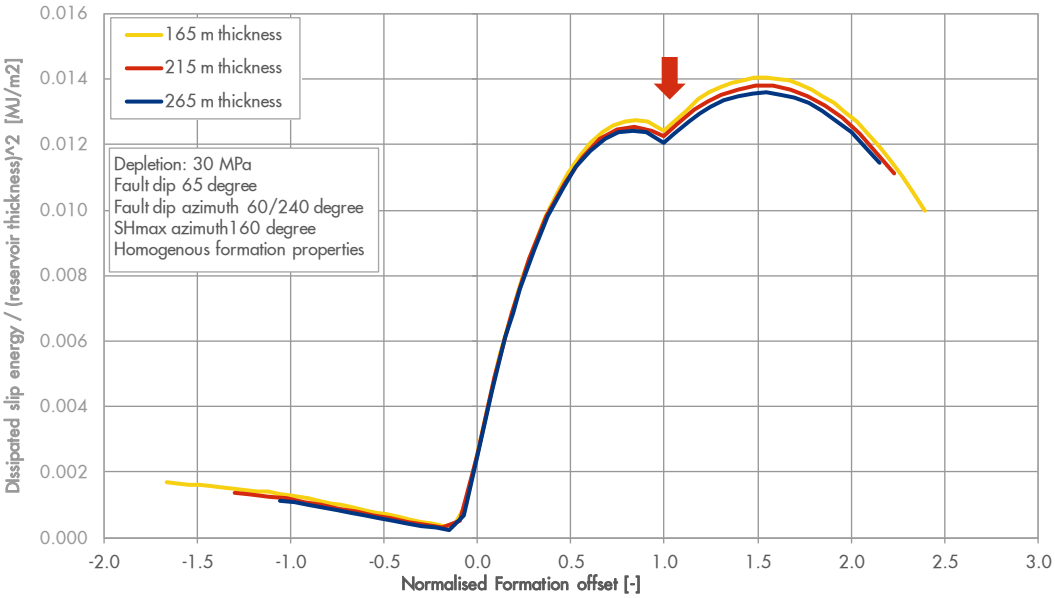

Figure 8.9: **Dissipated fault energy normalised for reservoir thickness [MJ/m²] as a function of normalised formation offset [-] under 30 MPa (300 bar) reservoir depletion. The red arrow indicates the normalised offset plotted in Figure 8.8.**

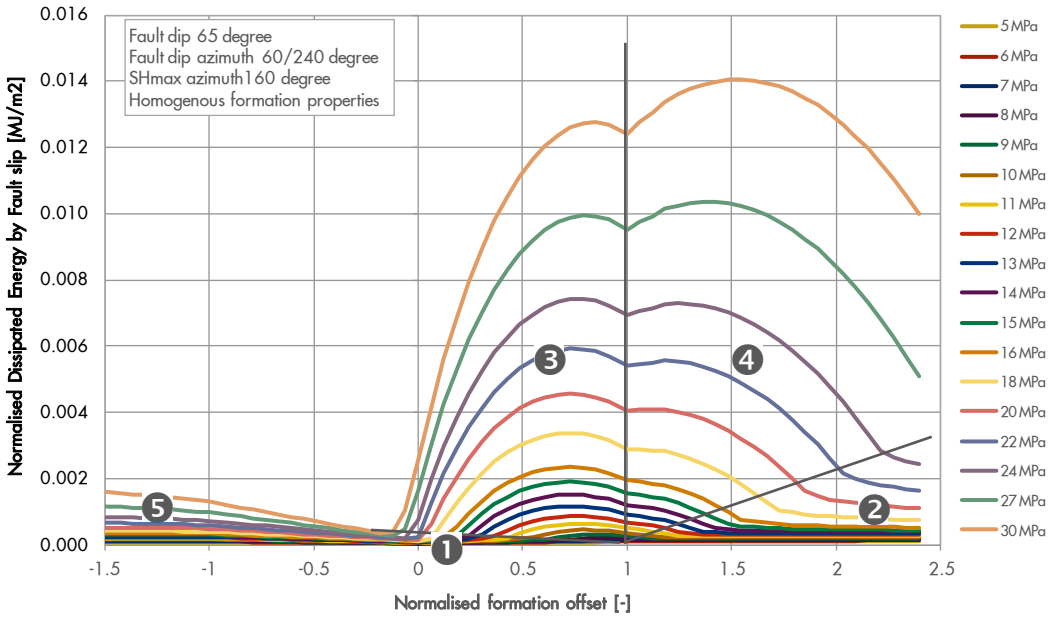

Figure 8.10: Normalised dissipated fault energy [MJ/m²] as a function of normalised formation offset [-] for various depletion levels [MPa].

8.5. Summary of the findings

In this chapter it is found that

- The depletion at the onset of fault slip is marginally influenced by the reservoir thickness;
- The total length of the slip patches is proportional with the reservoir thickness;
- The maximum Relative Shear Displacement is proportional with the reservoir thickness;
- The dissipated energy by fault slip is proportional with the square of the reservoir thickness.

Therefore, it is important to accurately account for the reservoir thickness in the assessment of the RSD and particularly the dissipated energy by fault slip.

9. Influence of fault orientation

The influence of the fault dip angle β_{dip} and the fault dip azimuth angle γ_{dip} relative to the maximum horizontal in-situ stress azimuth γ_{SH} is evaluated in combination with formation offset in this chapter. The influence of these parameters for the case without offset is discussed in Chapter 3 and Chapter 6. The fault dip azimuth has been varied between -20 to 160 degrees (from North to East) in steps of 5 degrees, while the azimuth angle of the maximum horizontal stress is not varied (160 degrees). Furthermore, the fault dip angle has been varied between 65 degrees to 85 degrees with the horizontal axis in steps of 5 degrees. This range of dip angles is most common to the Groningen field.

The onset of fault slip, the normalised total length of the slip patch, the normalised Relative Shear Displacement (RSD) and the faction of dissipated energy by fault slip are evaluated have been evaluated for a formation offset of 0, 80, 215, 300 and 440 meter and a reservoir thickness of 215 meter. All other model parameters are according to the Base case described in Chapter 2.

9.1. Results for 80 m formation offset

The onset of fault slip as a function of fault dip angle β_{dip} is plotted in Figure 9.1, and as a function of fault dip azimuth angle in Figure 9.2. As expected, fault planes oriented perpendicular to the minimum horizontal stress direction, i.e. 90 degrees with SHmax, allow the lowest depletion at the onset of slip. Furthermore, it is seen that vertical faults with a dip angle of 90 degrees with the horizontal allow a substantially higher depletion pressure to become instable than faults dipping under 65 degrees. A similar dependency has been found for faults without throw (section 6.3), in which case a dip angle larger than about 69 degrees does not cause onset of fault slip up to 30 MPa reservoir depletion. Numerical values are summarised in Table 9.1.

Table 9.1: Allowable depletion pressure at the onset of fault slip for a formation offset of 80m (see chapter 2 for all other model assumptions)

	Dip angle	
Azimuth angle	65 degree	90 degree
0 degree	8.7 MPa	18.2 MPa
90 degree	6.0 MPa	17.2 MPa

The fault dip angle has a larger impact on the depletion level at the onset of fault slip than the azimuth angle. This is explained by the relatively small difference between the two horizontal in-situ stress components which differ only 7% for the cases considered here (see Table 2.2 in Chapter 2). The difference between the maximum horizontal and the vertical stress component is 25%. The fault dip angle has a larger impact on the onset of fault slip, because it influences the exposure of the fault plane to the larger vertical stress component.

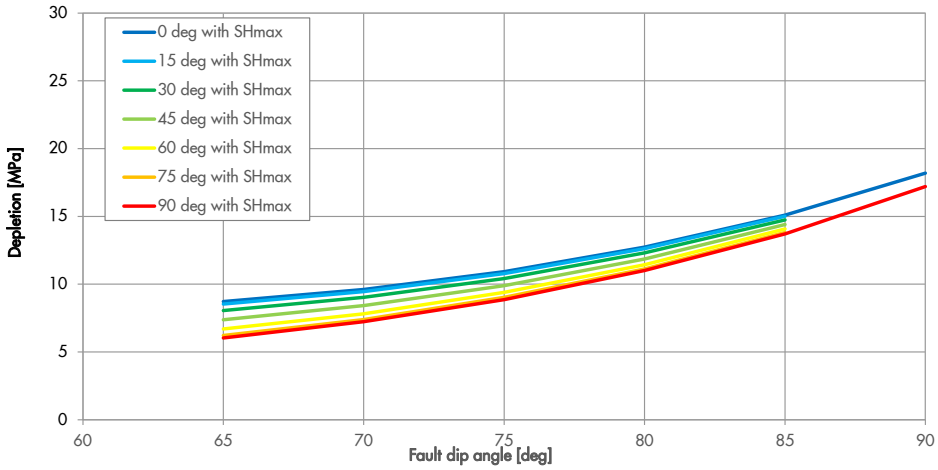

Figure 9.1: **Reservoir depletion pressure [MPa] at the onset of fault slip as a function of fault dip angle (with horizontal) for various angles between the fault dip azimuth and the maximum horizontal stress and for a formation offset of 80 m.**

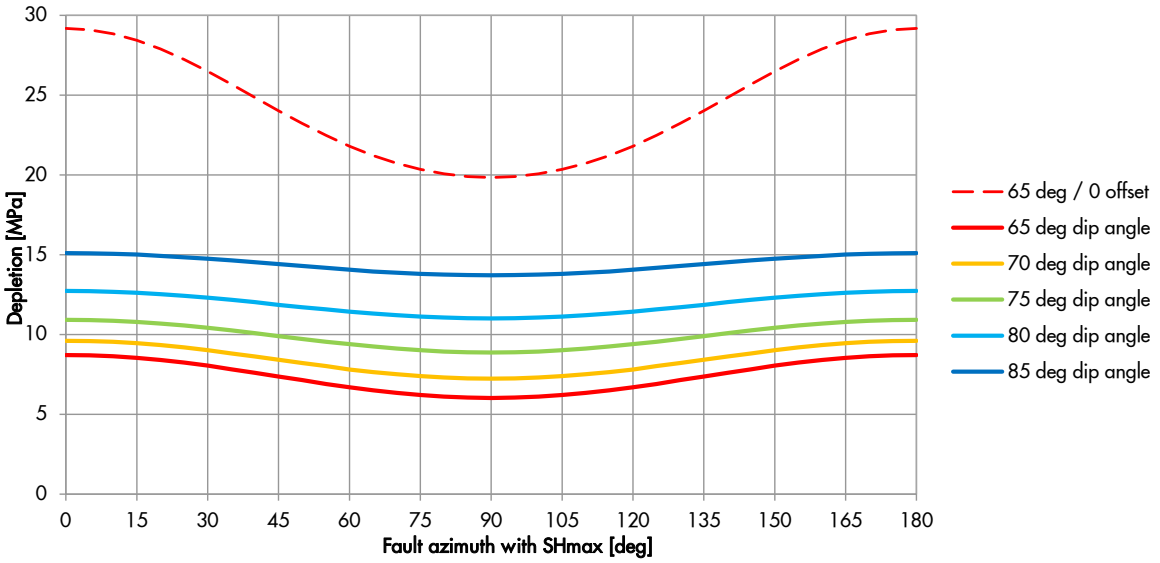

Figure 9.2: **Reservoir depletion pressure [MPa] at the onset of fault slip as a function of fault dip azimuth angle for various fault dip angles and a formation offset of 80 m. The results for the Base case with no formation offset (Chapter 3 and Chapter 6) is also given, with the notification that no onset of fault slip is found up to 30 MPa reservoir depletion for a dip angle steeper than 65 degree.**

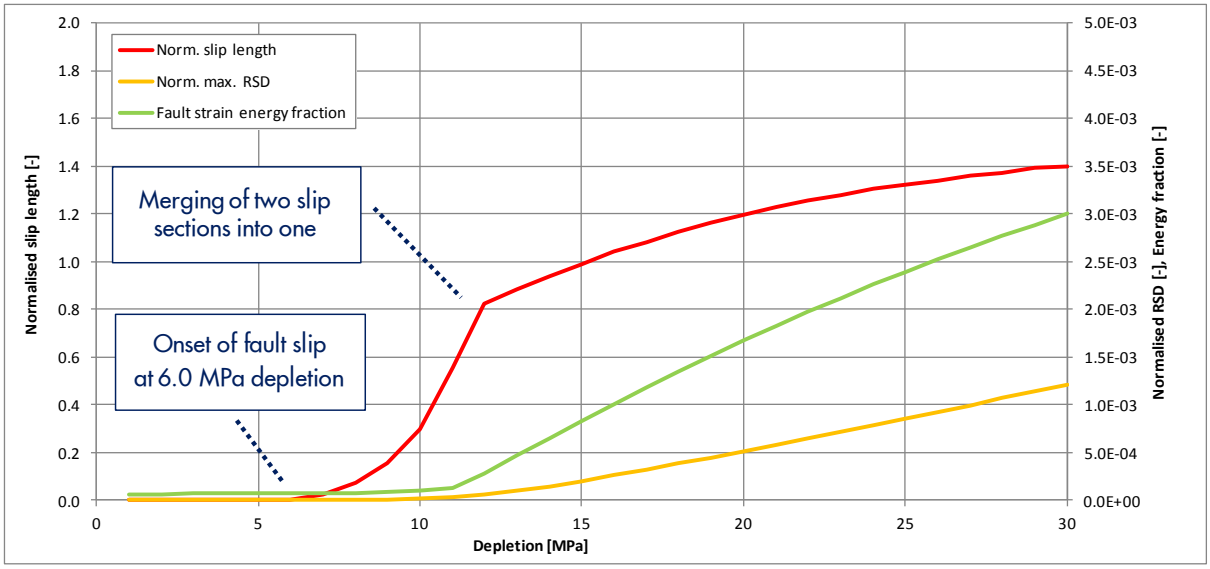

Figure 9.3: Development of the normalised slip patch (red, left-hand scale), the normalised RSD (yellow, right-hand scale) and the dissipated energy fraction by fault slip (green, right-hand scale) as function of the depletion level for a formation offset of 80 m, a fault dip angle of 65 degrees and a fault dip azimuth perpendicular to SHmax ($\gamma_{dip} - \gamma_{SH}$ = 90 degrees).

Figure 9.3 shows the total length of the slip patches and the Relative Shear Displacement (RSD) normalised for the reservoir thickness as well as the fraction of the gravitational energy that is dissipated by fault slip as a function of depletion for the most critical fault orientation in Table 9.1. That is, the fault dip azimuth is in the direction of the minimum horizontal in-situ stress, and the fault dip angle is 65 degrees. The total length of the slip patches is very similar to the relationship plotted in Figure 7.5. The only difference is the azimuth angle between the fault dip and the maximum horizontal stress, which are 80 degrees in Figure 7.5 and 90 degrees in Figure 9.3. Therefore, the onset of fault slip starts at a slightly lower depletion level in Figure 9.3 (6.0 MPa instead of 6.1 MPa) and also the inflection point at 12 MPa depletion that marks the merging of the two slip patches occurs at a slightly lower depletion level. It is found that the normalised RSD is $1.2 \cdot 10^{-3}$ and the energy fraction dissipated by fault slip is $3.0 \cdot 10^{-3}$ after 30 MPa depletion.

The larger impact of the fault dip angle compared to the fault azimuth angle on the fault slip response is also reflected in the energy fraction dissipated by fault slip (Figure 9.4). The red lines are the same case as shown in Figure 9.3 (green line). It is noted that the dissipated energy by fault slip remains relatively small as long as the two slip patched haven't merged. Again, it is seen that the dissipated energy develops at a higher depletion level if the fault is oriented more vertically or perpendicular to maximum horizontal stress.

Finally, Figure 9.5 shows the impact of the azimuth angle on the normalised total length of the slip patches, the normalised RSD and the energy fraction dissipated by fault slip. All three show a sinusoidal relationship with a maximum at an azimuth angle of 90 degrees with the maximum horizontal stress. For the current modelling assumptions (Chapter 2) and a fault dip angle of 65 degrees under 30 MPa depletion, it is found that the normalised length of the slip patch varies between 1.2 and 1.4, that the normalised RSD varies between $0.8 \cdot 10^{-3}$ and $1.2 \cdot 10^{-3}$, and that the energy fraction varies between $1.9 \cdot 10^{-3}$ and $3.0 \cdot 10^{-3}$.

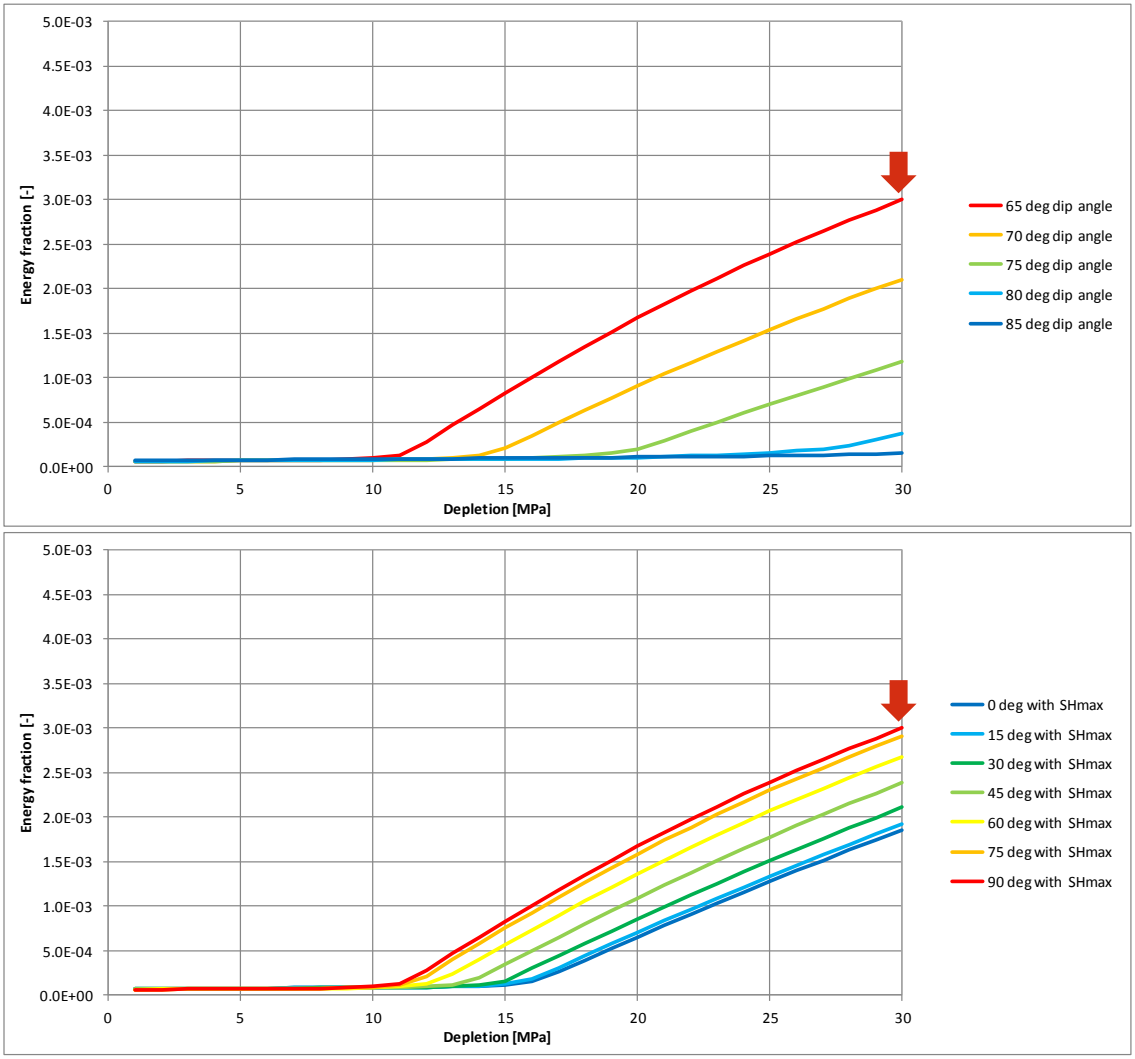

Figure 9.4: **Dissipated energy fraction by fault slip as function of the depletion level for different dip angles (top) and azimuth angles (bottom) and a formation offset of 80 m. The red arrows refer to the same worst case as plotted in Figure 9.3.**

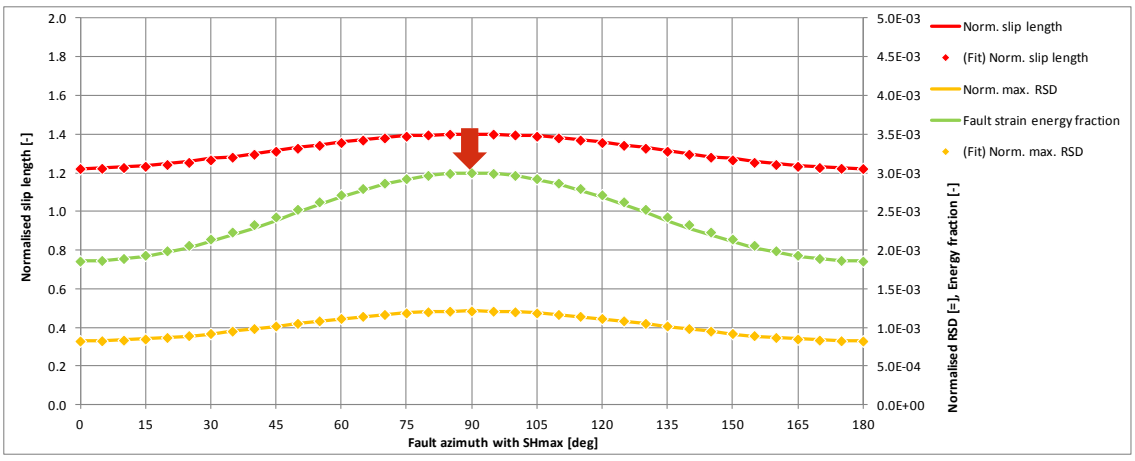

Figure 9.5: **Fit of $\bar{l}_{slip,\min}$ (red, left-hand scale), $\overline{\delta}_{\min}$ (yellow, right-hand scale) and $\overline{E}_{slip,\min}$ (green, right-handed scale) as a function of fault dip azimuth angle for a fault dip angle of 65 degrees under 30 MPa reservoir depletion. The red arrow refers to the same dissipated energy fraction shown by the red arrows in Figure 9.4.**

The reservoir depletion pressure ΔP at which onset of fault slip is calculated (Figure 9.2) shows a sinusoidal function of the fault azimuth angle. This is explained by the linear elastic response of the model and the Cauchy stress theorem [17]. However, also the post-failure responses in Figure 9.5 show a sinusoidal relationship: the normalised length of the slip patch $\bar{l}_{slip}$, the normalised Relative Shear Displacement $\bar{\delta}$ and the energy fraction dissipated by fault slip $\bar{E}_{slip}$. To prove the sinusoidal relationship, the following expressions are used to fit the results in Figure 9.5:

$$\Delta P = \left[\frac{\Delta P_{\max} + \Delta P_{\min}}{2}\right] + \left[\frac{\Delta P_{\max} - \Delta P_{\min}}{2}\right]\cos\left(2\cdot(\gamma_{SH} - \gamma_{dip})\right). \tag{9.1}$$

$$\bar{l}_{slip} = \left[\frac{\bar{l}_{slip,\max} + \bar{l}_{slip,\min}}{2}\right] - \left[\frac{\bar{l}_{slip,\max} - \bar{l}_{slip,\min}}{2}\right]\cos\left(2\cdot(\gamma_{SH} - \gamma_{dip})\right). \tag{9.2}$$

$$\bar{E}_{slip} = \left[\frac{\bar{E}_{slip,\max} + \bar{E}_{slip,\min}}{2}\right] - \left[\frac{\bar{E}_{slip,\max} - \bar{E}_{slip,\min}}{2}\right]\cos\left(2\cdot(\gamma_{SH} - \gamma_{dip})\right). \tag{9.3}$$

$$\bar{\delta} = \left[\frac{\bar{\delta}_{\max} + \bar{\delta}_{\min}}{2}\right] - \left[\frac{\bar{\delta}_{\max} - \bar{\delta}_{\min}}{2}\right]\cos\left(2\cdot(\gamma_{SH} - \gamma_{dip})\right). \tag{9.4}$$

Herein, $\Delta P_{\max}$ is found if γ_{dip} is parallel to the maximum horizontal stress direction, and $\Delta P_{\min}$ is found if γ_{dip} is at 90 degrees with γ_{SH} under the assumed normal stress condition. Similarly, the minimum value $\bar{l}_{slip,\min}$, $\bar{E}_{slip,\min}$ and $\bar{\delta}_{\min}$ are found if γ_{dip} is parallel to the maximum horizontal stress direction, and the corresponding maximum values are found if γ_{dip} is at 90 degrees with γ_{SH} under the assumed normal stress condition.

9.2. Influence of formation offset

Identical analyses have been conducted for a formation offset of 0, 215, 300 and 440 meter. In Figure 9.6 the depletion level at the onset of fault slip is shown as a function of fault azimuth angle for various formation offsets along the fault plane. This graph shows that for all cases with formation offset the impact of the azimuth angle of the fault with the maximum horizontal in-situ stress is relative limited compared to parameters discussed in previous chapters. This is caused by the small difference between the minimum and maximum horizontal in-situ stress in the current case (Section 2.3). The impact of the azimuth angle is larger in the case without formation offset, but remains within a range of about 8 MPa. It is noted that the same results are retrieved from Figure 7.3, which shows the onset of slip as a function of dip angle at an azimuth angle of 80 degrees.

The length of the slip patch monotonically increases with formation offset (Figure 9.7). Also, the impact of azimuth angle becomes more pronounces with increasing formation offset. A single slip patch has developed after 30 MPa reservoir depletion for all cases show, i.e. the slip patch length is larger than the reservoir thickness in all cases.

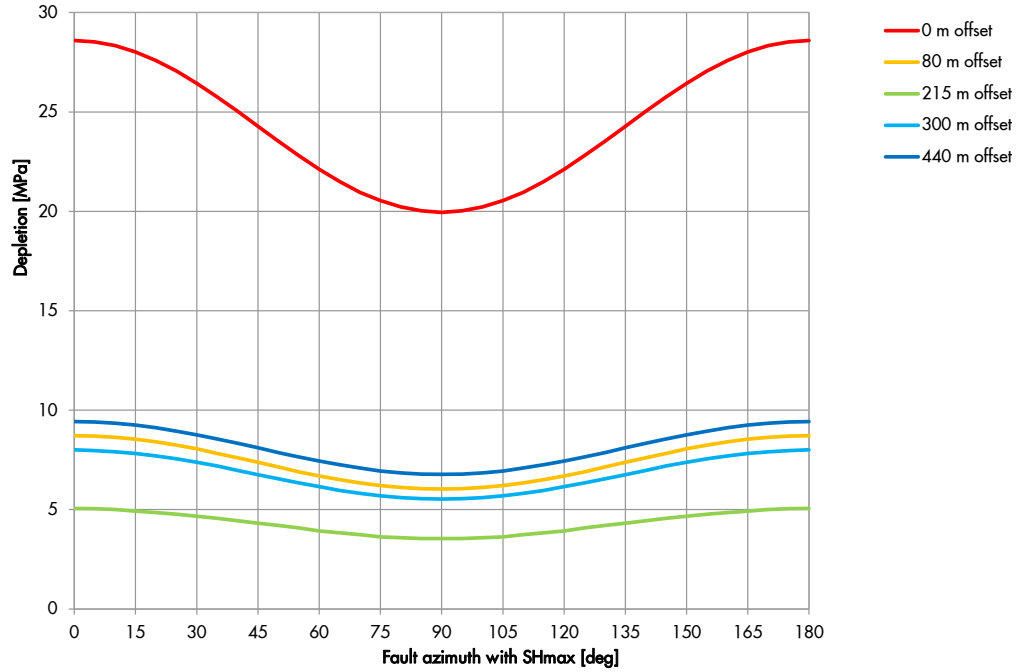

Figure 9.6: **Reservoir depletion pressure [MPa] at the onset of fault slip as a function of fault azimuth angle for a fault dip angle of 65 degrees under 30 MPa reservoir depletion for a different formation offsets.**

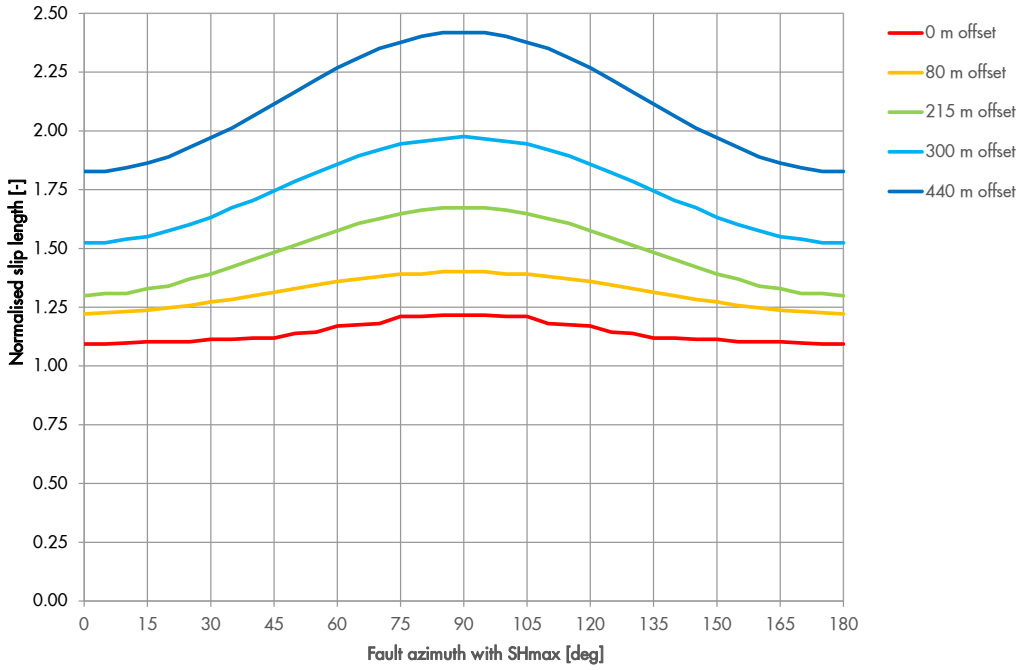

Figure 9.7: **Length of the slip patch normalised for reservoir thickness [-] as a function of fault azimuth angle for a fault dip angle of 65 degrees under 30 MPa reservoir depletion for a different formation offsets.**

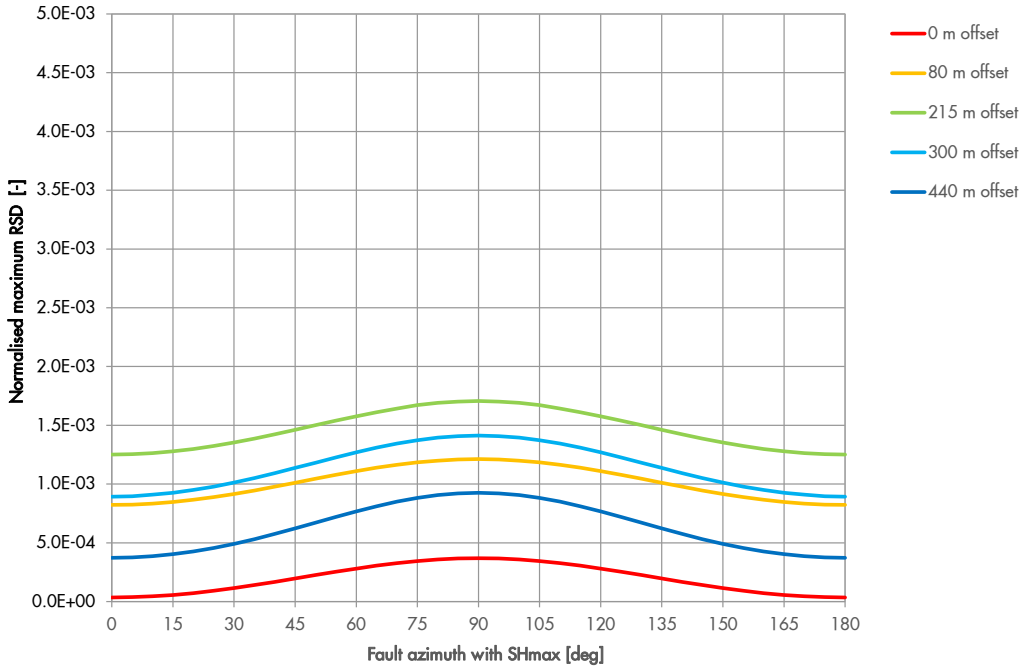

Figure 9.8: **Maximum RSD normalised for reservoir thickness [-] as a function of fault azimuth angle for a fault dip angle of 65 degrees under 30 MPa reservoir depletion for a different formation offsets.**

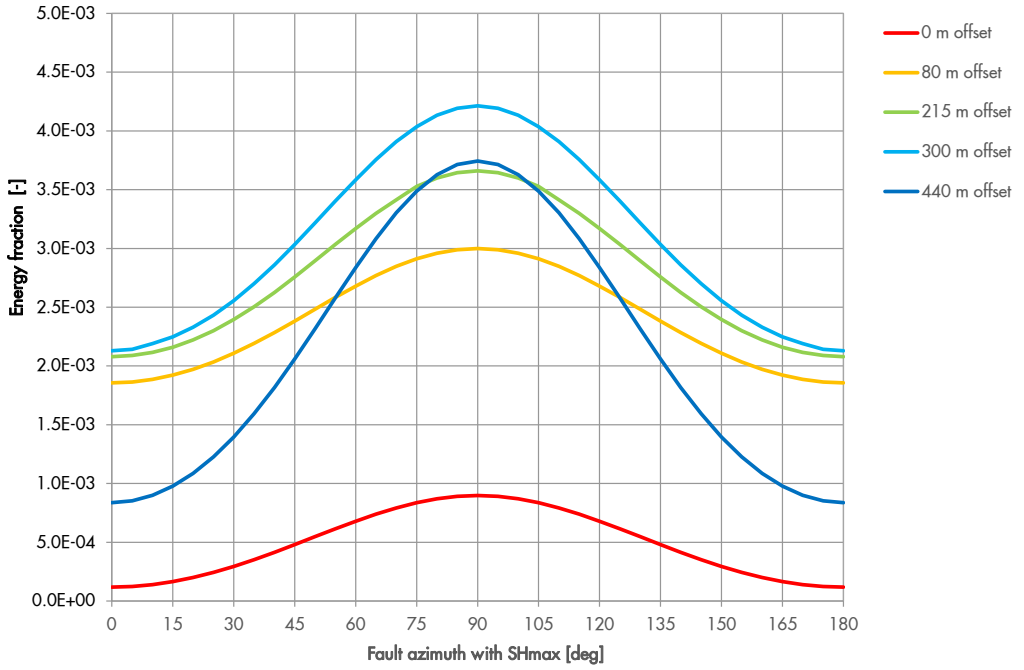

Figure 9.9: **Energy fraction dissipated by fault slip [-] as a function of fault azimuth angle for a fault dip angle of 65 degrees under 30 MPa reservoir depletion for a different formation offsets.**

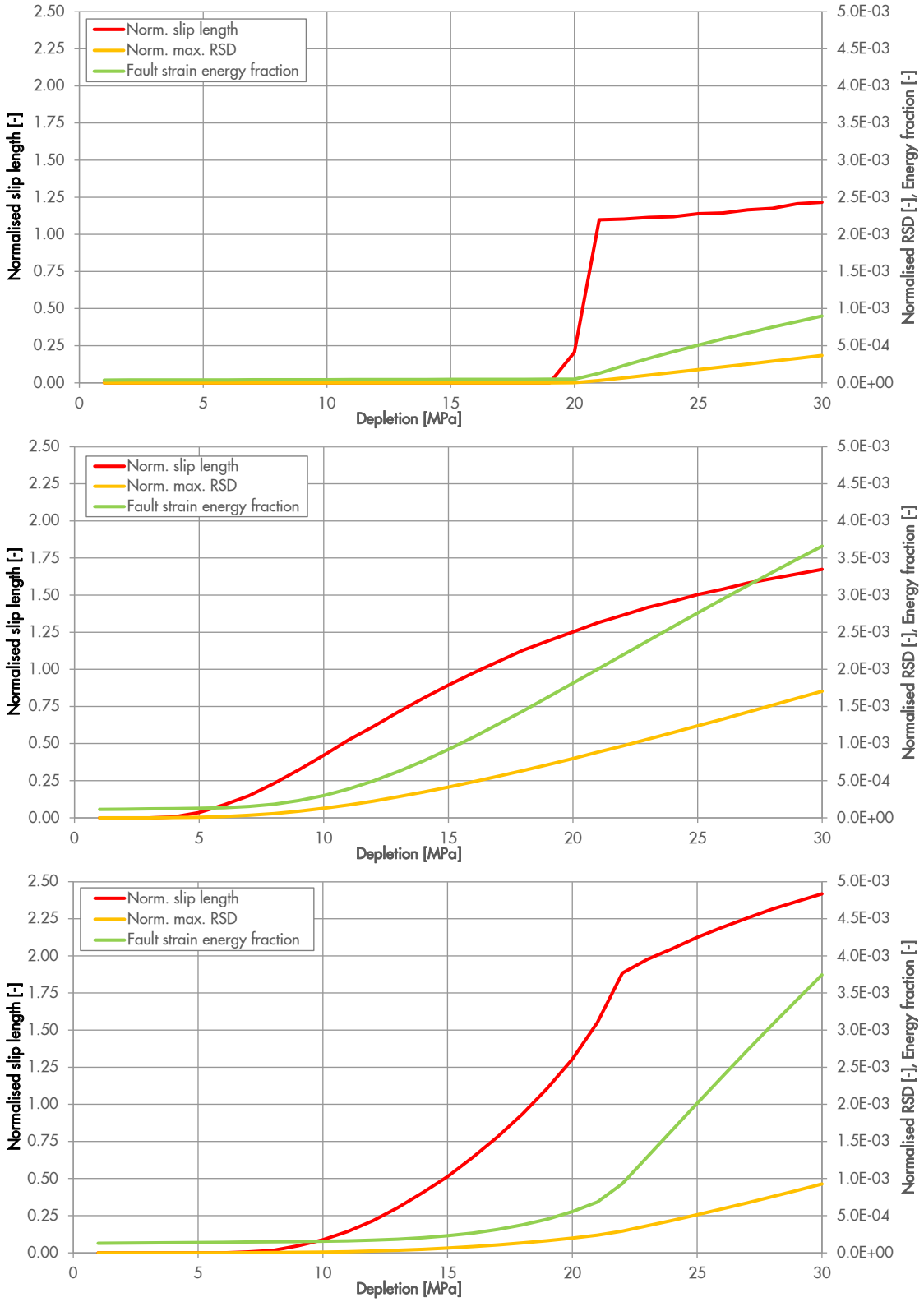

Figure 9.10: **Development of the normalised slip patch (red, left-hand scale), the normalised RSD (yellow, right-hand scale) and the dissipated energy fraction by fault slip (green, right-hand scale) as function of the depletion level for a formation offset of 0 m (top), 215 m (middle) and 440 m (bottom), and a fault dip angle of 65 degrees and a fault dip azimuth perpendicular to SHmax ($\gamma_{dip} - \gamma_{SH}$ = 90 degrees).**

For the cases considered, the maximum RSD is largest if the formation offset is equal to the reservoir thickness (215 m), see Figure 9.8. In Chapter 7, it is shown that the RSD is largest for an offset slightly smaller than the reservoir thickness. The maximum RSD is 0.17% of the reservoir thickness for a fault under 90 degree with the maximum horizontal stress and a throw equal to the reservoir thickness (green line).

The energy dissipated by fault slip is proportional with the length of the slip patch and Relative Shear Displacement and is therefore more influenced by azimuth angle than by the constituent parts (Figure 9.9). The increasing dependence on azimuth angle with increasing formation offset is inherited from the slip patch length.

Finally, in Figure 9.10, the normalise slip patch length, the maximum RSD and the energy fraction dissipated by fault slip are shown together for three cases.

9.3. Summary of the findings

The main finding in this chapter is that

- The depletion level at onset of fault slip, the slip patch length, the maximum RSD and the dissipated energy by fault slip show a sinusoidal function of the fault azimuth angle also for a non-zero formation offset
    - under the conditions specified in chapter 2, which include an ideal plastic friction law for fault slip.

The other finding is that

- the impact of the fault dip angle is larger than the dip azimuth angle because of the larger difference between vertical and horizontal in-situ stress than between the two horizontal stress components.

10. Summary and Discussion

First, the features of two of the applied methods are briefly discussed, namely the analytical approach and the use of the energy balance equation. Next, the findings are summarised related to the onset of fault slip and related to the subsequent post-failure slip behaviour.

Analytical versus finite-element approach

The analytical approach (based on an evaluation of the Mohr circle) provides fundamental insight in the role of various model parameters on the onset of fault slip. It is shown (section 6.2) how the virgin Mohr circle is influenced by the minimum and vertical effective stress in the subsurface, and how the fault dip and dip azimuth angle determine the location of the virgin stress point on the Mohr circle (section 6.3). The location of the virgin stress point on the Mohr circle reflect the normal effective and shear stress level in the virgin reservoir conditions. Using a Mohr circle representation for the state of stress on the fault plane helps to understand and quantify the impact of uncertainties of the mentioned modelling parameters.

The Mohr circle representation is also helpful describing the stress path due to reservoir depletion (section 4.2). It is found that Poisson's ratio strongly determines the stress path in the Mohr-circle representation whereas Young's modulus does not. Poisson's ratio can be related to the Stress-Path Coefficients as defined in section 2.7 in case of uni-axial compaction, which is generally a good approximation for major parts of large depleting fields.

The onset of fault slip calculated by the analytical approach is the same as calculated by the 2D finite-element model in the case of a fault located in a uniform linear-elastic subsurface and a uniformly depleting reservoir without offset. The post-failure response can of course not be captured by the analytical approach. Nevertheless, the approach can be a fast alternative for a finite-element analysis, while taking into account its limitations.

Energy balance equation

The consideration of the energy balance equation brings clarity in the driving force behind the fault slip process and the distribution of energy over different modelling components. Obviously, the calculated energy distribution is dependent on the components included in the model. The assumption of a linear-elastic subsurface in the current 2D model implies that no energy is dissipated by material failure in the subsurface formations. The static equilibrium assumption of the finite-element model implies that no kinetic energy is considered. Furthermore, no energy terms are included related to mass flow (of fluid and gas) and temperature. Despite these limitations, this study shows (section 3.1) that the release of gravity energy of the subsurface determines the energy available for re-distribution, and that it is proportional with the uni-axial compressibility of the depleting reservoir formations (Chapter 4).

The energy balance equation also makes clear that formation strain energy and energy dissipated by fault slip are in competition for the same energy source, which is the change of gravity energy of the subsurface. In the current study, the formation is not releasing strain energy because of the assumed ideal plastic fault slip behaviour. Further work should reveal how the magnitude of strain energy that may be released from the formations relates to the change of gravity energy of the subsurface. Also, further work is required into the distribution of available energy over fault slip and released seismic energy in relation to the post-failure behaviour of the fault. New insights may help to constrain the partitioning factor [23] that is used in the seismic hazard analysis. The energy balance equation shows that energy dissipated by fault slip or stored in any of the other energy components cannot be released as seismic energy.

The onset of fault slip

Formation offset of the depleting reservoir across the fault has a significant impact on the onset of slip. It is shown (Chapter 7) that the largest reservoir depletion to trigger fault slip is required for the configuration without formation offset. A configuration with an offset equal to the reservoir thickness requires the least depletion pressure to trigger fault slip, and can be less than a quarter compared to the case without formation offset. Furthermore is shown that a configuration with reservoir depletion on one side of the fault does not provide the lowest allowable depletion pressure at the onset of fault slip.

The consequences of depletion on the onset of fault slip can be described effectively by the followed stress path that describes the change of the (effective) normal and shear stress of a particular point on the fault plane. It is shown (section 6.2 and 6.3 and chapter 9) that the fault orientation in relation to the virgin in-situ stress condition determines the starting point of the stress path. In particular, the effective vertical and minimum horizontal stress components determine the size and location of the virgin stress circle, whereas the fault orientation (dip angle and dip azimuth) determine the starting point of the stress path on the Mohr circle. Poisson's ratio, the fault dip angle, and in particular the formation offset strongly influences the direction of the stress path as a result of reservoir depletion. Finally, fault cohesion and friction angle determine the end point of the stress path at which onset of fault slip occurs. This is in line with results from previous studies [3].

The starting point and the end point of the stress path are both uncertain, but the occurrence of a seismic event at a location and particular depletion level could be possibly used as an indicator for the stress path. This assumption is used in Section 4.2 and Chapter 6 to develop a relationship between the possible values of Poisson's ratio, fault cohesion and friction angle and virgin minimum horizontal in-situ stress. A seismic event is evidence that failure has occurred and thus could provide information about the stress path followed.

Young's modulus has a limited impact on the onset of fault slip in comparison to the other investigated parameters. Chapter 4 shows that stiffness contrasts across the fault have the largest impact on the onset of fault slip, whereas contrasts in Young's modulus have no impact in a horizontally layered subsurface. This is a different, but not contradicting result compared to previous work [14][15]. In this previous work, stiffness contrasts between the reservoir and overburden is the basis to assume a larger horizontal in-situ stress in the overlying seal prior to hydrocarbon production, thereby causing a larger threshold to the onset of fault slip. Here, it is shown that stiffness contrast in a horizontally layered subsurface has no effect on the onset of fault slip under reservoir depletion conditions. Only stiffness contrasts across the fault have a (geo)mechanical impact.

Reservoir thickness has no significant impact on the onset of fault slip. Virtually the same reservoir depletion is found at the onset of fault slip for a wide range of reservoir offsets. The minor differences found in this study are attributed to the depth difference of the fault slip initiation point.

Fault slip response (after the onset of fault slip)

Only a few promille of the released gravity energy is dissipated by fault slip after the onset of fault slip, and causes a reduced storage of formation strain energy. The fault pressure energy level remains negligible before and after the onset of fault slip in all cases evaluated in this study.

The reduced storage of formation strain energy after the onset of fault slip is recognised by the stress and strain distribution in a zone smaller than one reservoir thickness adjacent to the fault. Before the onset of fault slip, a uniform stress and strain distribution is found across the fault indicating that the fault is able to carry the shear stress induced by reservoir depletion without slipping. After the onset of fault slip, the ideal-plastic slip law employed in this study prescribes that the shear stress carrying capacity remains constant, irrespective of the Relative Shear

Displacement (RSD). This prevents storage of additional formation strain energy next to the fault upon further reservoir depletion. An undisturbed uni-axial stress and strain condition is found at a distance of one reservoir thickness from the fault.

The ideal-plastic slip law causes stable propagation of the slip patch. That is, incremental reservoir depletion is required to propagate fault slip. This is explained by the fact that fault slip dissipates (requires) energy, and that gravity energy in the only source that releases energy. Moreover, (additional) gravity energy is released by (additional) reservoir depletion. For this reason, the simulated fault slip propagates in a stable fashion driven by reservoir depletion.

Fault slip weakening behaviour could lead to unstable and potentially seismogenic fault slip. Slip weakening assumes that the shear stress carrying capacity of the fault reduces (not necessarily to zero) with increasing RSD. It is noted that energy is dissipated (required) by incremental fault slip also in this case. However, fault slip weakening also causes a reduction of stress and therefore causes the release of strain energy from the formation adjacent to the fault. Unstable fault slip occurs if the strain energy released from the formation is larger than the energy required to propagate the slip patch.

In this context, also the shear stress and SCU distribution along the fault plane is important. Fault slip remains stable (driven by depletion) if points on the fault plane adjacent to the slip patch have sufficient shear stress capacity left to carry the shear stress from the parts of the fault that display slip weakening behaviour. This implies that configurations with a more even distribution of the SCU along the fault plane are more vulnerable for unstable slip propagation than configurations with large peak values. The fault friction angle (section 6.1), but particularly fault throw (section 7.1) determine the SCU distribution over the depleting reservoir section of the fault. A more even distribution of the SCU causes a more rapid development of the slip patch length with ongoing depletion, which suggests a larger vulnerability for potential unstable slip propagation. Therefore, the slip patch length or the change of slip length per unit depletion may be a better indicator for seismic events than the onset of fault slip.

Potenial deployment of the static 2D fault model

One of the shortcomings of the finite-element model used in this study is assumption of static equilibrium. Mass acceleration and deceleration characterises a seismic event, and required a dynamic equilibrium analysis that takes into account mass inertia and kinetic energy. However, the subsurface is in static equilibrium just before and just after an earthquake, which marks the transition from one fault slip condition to another in an unstable fashion. The presence of asperities [5] may influence the depletion level at which this change of equilibrium state occurs. However, the current model can calculated change of gravity energy by considering the difference between two fault slip conditions. Also, the absolute length of the slip patch before the seismic event or the incremental slip patch length during the seismic events could use to represent the magnitude of the earthquake.

11. Conclusions and Recommendations

It is concluded that

- The energy dissipated by fault slip reduces the storage of strain energy in the reservoir formation after the onset of fault slip.
    - The reduced storage of strain energy in the reservoir occurs within a zone less than one reservoir thickness from the slipping fault.
    - Release of formation strain energy does not occur under the ideal-plasticity assumption for fault slip employed in the current study
    - The released gravity energy is mainly distributed over formation strain and pressure energy terms before the onset of fault slip
- The current static modelling approach does not account for kinetic energy and for fault slip weakening behaviour as part of the slip process.
    - Kinetic energy is considered an essential additional term to describe the transition from the static equilibrium before and after a seismic event.
    - Slip weakening behaviour is essential to describe the reported stress drop (e.g. [4]) that is observed in earthquakes, and to allow release of strain energy from the formations adjacent to the fault
- Stiffness contrasts of formations across the fault have an impact on the stress path during reservoir depletion, while the impact of stiffness contrast between horizontal layers formation layers is very limited.
    - The impact of stiffness contrasts on the occurrence of seismic events reported elsewhere [14][15] is caused by an implied difference of the horizontal stress between reservoir and overburden.
- Distinctly different fault slip behaviour is found for faults with a throw smaller than the reservoir thickness, a thrown larger than the reservoir thickness and for up-thrown blocks.
    - Depletion at the onset of fault slip is
        - Lowest for faults with a throw equal to the reservoir thickness
        - Largest for faults without throw
    - Depletion at one side of the fault is not most critical for the onset of fault slip
    - The slip patch length is accelerating most with depletion for faults with small throws and for throws much larger than the reservoir offset. These configurations are expected to be most vulnerable for instable, potentially seismogenic, fault slip propagation.
- The direction and the length of the stress path at the most critical point on the fault plane determine the depletion level required to cause the onset of fault slip. The number of uncertain model parameters to describe the onset of fault can be a number of modelling parameter
    - Fault orientation, virgin in-situ stress, fault cohesion and friction angle in conjunction with the depletion pressure influence the length of the stress path
    - Poisson's ratio and formation offset influence the direction of the stress path of any material point on the fault plane
- The RSD and the slip patch length are proportional to the reservoir thickness. The dissipated energy by fault slip is proportional with the square of the reservoir thickness, whereas the onset of fault slip is not dependent on the reservoir thickness.
- The analytical Mohr-circle approach does not provide a conservative estimate of the fault stability condition in petroleum industry applications, because it provides an upper bound for the depletion pressure required to cause onset of fault slip.

The following hypotheses can be articulated based on the results of this study:

1. The onset of fault slip (calculated by a static 2D model) can be correlated to the occurrence of a seismic event taking into account realistic fault orientation, formation offset and reservoir pressure data.
2. The length of the slip patch (calculated by a static 2D model) can be correlated to the occurrence of a seismic event taking into account realistic fault orientation, formation offset and reservoir pressure data.
3. The incremental length of the slip patch with depletion (calculated by two static 2D models) can be correlated to the occurrence of a seismic event taking into account realistic fault orientation, formation offset and reservoir pressure data.
4. The stress path length and/or stress path direction can be correlated to the available seismic event data taking into account realistic fault orientation, formation offset and reservoir pressure data.
5. Faults with a reservoir formation offset about equal to the reservoir thickness are less vulnerable for unstable fault slip propagation (potential seismic events) than faults wih a small or large formation offset (smaller than a third, or larger than 3 time the reservoir thickness) and therefore should correlate better with observed seismic event data.

The following work is required to test these hypotheses:

1. Map available seismic event data on known faults and determine possible fault locations that could have facilitated the seismic event and retrieve fault orientation, reservoir formation offset and reservoir depletion pressure in the neighbourhood of the observed event locations.
2. To estimate the uncertainty of in-situ stress under virgin and depletion conditions by 3D model evaluations that are calibrated against historical subsidence data and incorporate
    - formation offset in detail
    - salt creep behaviour
3. Develop a method that determines stress path direction and length from virgin in-situ stress (incorporating results of point 2), fault orientation, formation offset and reservoir pressure data. This may include a probabilistic version of 2D model to allow a quantified assessment of the uncertainties of the various modelling parameters.
4. Prepare dedicated statistical methods and test the articulated fault-based hypotheses.

Further work is required to articulate additional and potential more promising hypotheses that relate the release of gravity energy, the energy stored in formation strain and/or the energy dissipated by fault slip using the current 2D model to the seismic moment of historical events. This effort builds further on the work under points 1 and 3 above and includes:

5. Comparison of the energy terms of two stable fault slip conditions, namely one before and one after an unstable fault slip event, for a large range of fault configurations (formation offset, reservoir thickness, virgin in-situ stress orientation and magnitude).

Also, further work is recommended to articulate potential hypotheses including energy terms that are not included in the current static 2D model, such kinetic energy and energy dissipation by nonlinear and time-dependent behaviour of reservoir and non-reservoir formations.

6. Conduct dynamic 2D fault rupture analysis
    - That account for the kinetic energy during the fault slip process to understand the transition between the different energy terms during the fault slip process
    - That account for fault slip or velocity weakening behaviour to understand the requirements between a stable and an unstable (potentially seismogenic) fault slip process in terms of various modelling options and parameters.
    - To attempt relating modelling parameters for slip-weaking, formation offset, in-situ stress, etc. to the seismic moment.

    - To formulate and test a hypothesis that relate kinetic energy, the energy dissipated by fault slip, and the release of stored formation strain energy to seismic moment.
7. Conduct non-linear 2D sensitivity analyses as reported in this document incorporating:
    - plasticity models for various formation layers
    - salt creep behaviour

Experimental work is recommended to

8. investigate the unloading behaviour of reservoir formations caused by fault slip-weakening behaviour

Finally, it is recommended that

9. The analytical Mohr-circle approach to assess onset of fault slip in petroleum geomechanics should be replaced by an improved, more conservative approach based on the insights of this study.

Aknowledgements

TNO-DIANA is acknowledged for developing the 2D model generator, and the contribution to the specification of the energy balance equation. Rob van Eijs and Rick Wentinck are acknowledged for their fruitful discussions in course of this study and reviewing this report. Clemens Visser (NAM) has been instrumental in providing relevant structural information. Futhermore, Jan van Elk and Dirk Doornhof (NAM) are thanked for supporting this work, and particular providing the space to conduct a study with a longer-term perspective.

References

[1] Bouts, M., Regional horizontal stresses in the Netherlands, NAM doc. 200008100412, September 2000.

[2] Bree, P. de, Status of the differential strain analysis technique for the prediction of in-situ stress and hydraulic fracture orientation, RKGR.87.158.

[3] Glab, M. and Van Eijs. R (2001), Localisation of Sensitive Reservoir Settings for Induced Seismicity using FEM, Report TNO-NITG 00-320-A.

[4] Kanamori, H. (1994), Mechanics of Earthquakes. Annual Rev. Earth Planet Sci., 22, p207-237

[5] Mulders, F.M.M., Modelling of stress development and fault slip in and around a producing gas reservoir, Ph.D. Thesis Delft University of Technology, 2003.

[6] Orlic, B. and Wassing, B.B.T. (2012), Modeling stress development and fault slip in producing hydrocarbon reservoirs overlain by rock salt caprocks, ARMA 12-145, 46th US Rock Mechanics / Geomechanics Symposium, Chicago, USA, 24-27 June 2012.

[7] Roest, J.P.A., Kuilman, W. (1993). Geomechanische Analyse van de lichte aardschokken in het Eleveld reservoir, TU-Delft (In Dutch).

[8] SVS user manual

[9] van den Bogert, P.A.J., Deployment of Linear-Elasticity Theory in Borehole Stability Modelling,

[10] van den Bogert, P.A.J., van Eijs, R. and van der Wall, O. Groningen Fault Stability Assessment using an analytical Mohr-circle approach (in press)

[11] van den Bogert, P.A.J., Lim, K.C. and Schutjens, P., Assessment of shear and tensile failure of the reservoir rock and fault slip induced by depletion an subsequent injection in the St. Joseph field (Malaysia), using analytical and a probabilistic, SR.12.11511, August 2012.

[12] van Eijs, R., Personal communications, Oktober 2014

[13] van Eijs, R. van, Dalfsen, W. van, Borehole observations of maximum horizontal stress orientations in the Dutch upper crust. TNO-NITG – Information, December 2004.

[14] Van Eijs, R.M.H.E., Mulders, F.M.M., Nepveu, M., Kenter, C. en Scheffers, B.C., Correlation between hydrocarbon reservoir properties and induced seismicity in the Netherlands. Engineering Geology, 84, 99-111. 2006

[15] Van Thienen-Visser, K. Nepveu, M., Hettelaar, J., Deterministische hazard analyse voor geinduceerde seismicitiet in Nederland (in Dutch). TNO-rapport 2012 R1-198, 2012.

[16] Veeken, C.A.M., Hertogh, G.M.M. and Hydendaal, H.G.C, Groningen Sand Failure Study Status Report, Part 2: Rock Stress and Rock Strength in Groningen/Annerveen Fields, RKGR.89.201, September 1990.

[17] Verruijt, A., Soil Mechanics, November 2011, http://geo.verruijt.net

[18] Visser, C. (edt.), Groningen Field Review 2012, Static Modelling and Hydrocarbon Volume Determination, Document number: EP201203204663.

[19] Warpinski, N.R. & Teufel, L.W., A viscoelastic constitutive model for determining in-situ stress magnitudes from anelastic strain recovery of core", SPE Prod. Eng., Aug 1989, pp.272-280.

[20] World Stress Map

[21] TNO, Toetsing van de Bodemdalingsprognoses en seismische hazard ten gevolge van gaswinning van het Groingen veld, Report TNO 2013 R11953, December 2013 (In Dutch).

[22] TNO-DIANA bv, DIANA: Finite-Element Program and User Documentation, version 9.4.3, 2011.

[23] Technical Addendum to the Winngingsplan Groningen 2013, Subsidence, Induced Earthquakes and Seismic Hazard Analysis in the Groningen Field, NAM, November 2013.

Appendix 1. Model generator for 2D fault slip simulations

The 2D fault model generator requires a single (ASCII) input file to prepare the input and command files for the DIANA finite-element software and to launch the calculation. Results are made available by a tabulated (ASCII) output file as well as a Femsys results file for further post-processing and analysis. The required input parameters are listed in Table A1.1.

Table A1.1: Input parameters for 2D model generator with fault

Model	Property	Unit
Boundary conditions	Surface Depth (D-surf)	[m]
	Surface load	[MPa/m]
	Model half width	[m]
Model orientation	Azimuth maximum horizontal stress	[deg]
Fault orientation	Fault dip angle	[deg]
	Fault dip azimuth	[deg]
Fault properties		
Shear failure	Cohesion	[MPa]
	Friction angle	[deg]
	Dilatancy angle	[deg]
Pore pressure	Communication with	Hanging wall or Foot wall
Formation properties		
Geometry	Thickness	[m]
Material properties	Young's modulus	[MPa]
	Poisson's ratio	[-]
In-situ stress	Density	[kg/m3]
	K0-max hor stress	[-]
	K0-min hor stress	[-]
Pore pressure	Reference Depth (D-ref)	[m]
	P-ini at D-ref	[MPa]
	P-ini-gradient at D-ref	[MPa/m]
Loading		
Pore pressure change	Layer 2 and Layer 3 Hanging & Foot wall	[MPa]

Appendix 2. Model Validation

A2.1. Stress condition along a vertical fault plane

The model generator has been tested for the case of a vertical fault (dip angle of 90 degrees with the horizontal) and various dip azimuth angles Table A2.2. The fault dip azimuth is defined as the angle between the fault normal vector and the North direction in a horizontal plane, being positive from North to East. Four cases have been run with a fault dip azimuth between 0 and 90 degrees as indicated in Table A2.2. The maximum horizontal stress is oriented in Northern direction for all 4 cases. This means that the normal effective stress on the fault plane should be equal to the maximum effective horizontal stress in Case 1, and equal to the minimum horizontal stress in Case 4.

Homogenous material properties and in-situ stress condition have been assumed for all four cases Table A2.3. The formation thickness and density have been set to match the Groningen field conditions over the Slochteren sandstone as closely as possible. The pore pressure gradient is hydrostatic for layers 1 and 2, and somewhat over-pressured in Layer 4. A gas pressure gradient is assumed in Layer 3 with a Gas-Water Contact (GWC) at 2995, which coincides with the top of Layer 4 in the model.

Table A2.1: Fault and in-situ stress orientation in validation cases 1 through 4

Property	Unit	Case 1	Case 2	Case 3	Case 4
Fault dip angle	[deg]	90	90	90	90
Fault dip azimuth	[deg]	0	30	45	90
Max. Hor. stress azimuth	[deg]	0	0	0	0

Table A2.2: Model parameters for Test Cases 1 through 4

Formations			Layer 1	Layer 2	Layer 3	Layer 4
Geometry	Thickness	[m]	2780	50	165	3000
Material properties	Young's modulus	[MPa]	10000			
	Poisson's ratio	[-]	0.25			
In-situ stress	Density	[kg/m3]	2172	2450	2450	2700
	K0-max hor. stress	[-]	0.795			
	K0-min hor. stress	[-]	0.748			
Pore pressure	Reference Depth (D-ref)	[m]	0	0	2995	2995
	P-ini at D-ref	[MPa]	0	0	35.2	35.2
	P-ini-gradient at D-ref	[MPa/m]	0.0100	0.0100	0.0018	0.0117
Loading						
Pore pressure change	Hanging wall change	[MPa]	0	0	-20	0
	Foot wall change	[MPa]	0	0	-20	0

The pore pressure distribution in the fault under virgin and depleted reservoir conditions is shown in the left-hand side of Figure A2.1. This model assumes a top-seal for Layer 2 and a reservoir unit for Layer 3. The formation horizons are indicated by three short lines on the left

side of the graph, and three on the right side of the graph. These lines are plotted at 2780m, 2830m and 2995m TVD on both sides of the graph, because no formation offset across the fault is assumed in Test Cases 1 through 4. The virgin gas gradient in (reservoir) Layer 3 causes a step-change in pore pressure between Layer 2 and 3. Furthermore, it is seen that the pore pressure is reduced by 20 MPa in Layer 3, while the pore pressure in the fault remains unchanged across the other formation layers.

The effective normal and shear stress distribution along the fault plane under virgin and depleted reservoir conditions is shown in the right-hand side of Figure A2.1. The gas gradient in Layer 3 causes the lowest normal effective stress level to occur at the most shallow point of the reservoir. Furthermore, it is seen that the normal effective stress on the fault increases (becomes more negative) under depletion conditions. It is highlighted that in Case 1 no vertical shear stress component is present under virgin or depleted reservoir conditions, because the fault normal vector is oriented in one of the principal stress directions, namely the maximum horizontal stress direction.

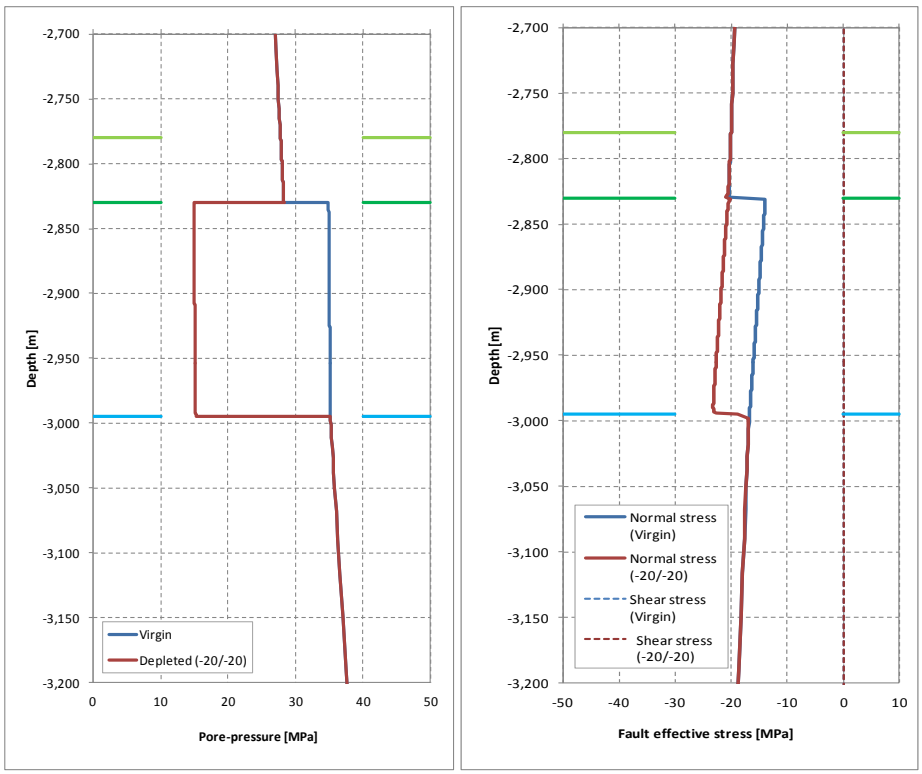

Figure A2.1 **Pore pressure for test cases 1 through 4 (left) and fault effective normal and shear stress distribution as a function of depth for case 1 (right). Compressive stress is negative.**

A2.1.1. Validation of the initial stress condition

The normal and effective stress on a vertical fault plane in Test Cases 1 through 4 is evaluated at 2875 m depth. This evaluation depth was also used in a previous study [10]. The values for the three in-situ stress components and the pore pressure given in Table A2.4 are prescribed by the density and depth values given in Table A2.3. The fault normal effective stress in Test Case 1 is equal to the maximum effective horizontal stress, whereas the fault normal effective stress in Test Cases 2 through 4 is derived by rotation of the in-situ stress tensor σ around a vertical axis using [9]:

$$\bar{\sigma} = \mathbf{R}\sigma\mathbf{R}^T,$$

With R the rotation matrix of the global *XYZ*-coordinate system into a $\overline{XYZ}$ -coordinate system associated with the fault plane. Here, the maximum horizontal stress being σ_{xx} is in the Northing direction, the minimum horizontal stress being σ_{yy} is in the Easting direction, and the vertical stress component being σ_{zz} is in the vertical direction. In case of a rotation γ from North to East around the *Z*-axis, the rotation matrix reads:

$$\mathbf{R_z} = \begin{bmatrix} \cos\gamma & \sin\gamma & 0 \\ -\sin\gamma & \cos\gamma & 0 \\ 0 & 0 & 1 \end{bmatrix}.$$

The numerical values for the normal effective stress along the fault plane correspond within 0.4% from the analytical solution Table A2.5. The fault normal effective stress is equal to the minimum horizontal stress in Test Case 4, in which γ =90 degree. Shear stress is present on the fault plane in Test Cases 2 and 3 where the fault normal vector makes an angle of 30 and 45 degrees with the maximum horizontal stress respectively. However, this shear stress component works in the direction perpendicular to the modelling plane, and therefore does not develop a shear stress that is captured by the interface elements. This leads to the (trivial) conclusion that the current 2D model is not capable of simulating strike-slip behaviour.

Table A2.3: Total and effective initial stress condition at a reference depth of 2875m TVD based on the density values given in Table A2.3. The maximum horizontal stress is in Northing direction.

Virgin in-situ stress	Total stress [MPa]	Effective stress [MPa]
Vertical	-61.51	-26.53
Maximum horizontal	-48.90	-13.92
Minimum horizontal	-46.01	-11.03
Pore pressure	-34.98	

Table A2.4: Analytical and model results for the fault effective normal stress under initial stress conditions at a reference depth of 2875m TVD for the cases 1 through 4.

Normal stress	Case 1	Case 2	Case 3	Case 4
Analytical [MPa]	-13.92	-13.20	-12.47	-11.03
Model [MPa]	-13.87	-13.15	-12.43	-10.98
Deviation	-0.4%	-0.4%	-0.3%	-0.4%

A2.1.2. Validation of the depleted stress condition

The vertical and – in particular – the horizontal stress magnitude changes in the reservoir formation due to depletion, although the shear stress remains negligible along the vertical fault plane (Figure A2.1). This is because the fault normal vector is and remains oriented in the direction of one of the principal stress components. The change of total principal stress ΔS_i (i=1, 2 or 3) can be related to the change of pore pressure ΔP_p according to [10] :

$$\Delta S_i = \gamma_i \Delta P_p .$$

The so-called stress-path coefficient γ_i may be different in each principal direction, which coincides with the vertical, the minimum and maximum horizontal stress directions in the current cases. For a uniaxial deformation condition in the 2D plane-strain model, the change of effective horizontal stress $\Delta\sigma_{xx}$ can be related to the change of effective vertical stress $\Delta\sigma_{zz}$ and Poisson's ratio ν, according to

$$\Delta\sigma_{xx} = \frac{\nu}{1-\nu}\Delta\sigma_{zz}.$$

The same relation holds for the other horizontal stress component, $\Delta\sigma_{yy}$. This leads to equal stress-path coefficients in two horizontal directions [ref]:

$$\gamma_h = 1 - \frac{\nu}{1-\nu} = \frac{1-2\nu}{1-\nu}.$$

When considering a poro-elastic formation response, this expression generalises to December 2013 (In Dutch) [22]

$$\gamma_h = \alpha\left(\frac{1-2\nu}{1-\nu}\right),$$

in which α is Biot's coefficients. The horizontal stress-path coefficient γ_h is 2/3 if Biot's α is 1 and Poisson ratio is 0.25 as specified in Table A2.3.

The total horizontal and vertical stress condition for Case 1 calculated at 2875 m TVD in the continuum element of the finite-element model are plotted in Figure A2.2. The horizontal x-coordinate runs from the left boundary of the model to the fault in the centre of the model at about x=0. A similar uniform stress distribution can be drawn at any depth in the reservoir. The horizontal stress coefficient is plotted as a function of depth in Figure A2.3. The calculated stress-path coefficient is 0.6675 in both horizontal directions except from the peaks at the top and bottom of the depleting reservoir layers, while the analytical value is 2/3. It is therefore concluded that a uniaxial compaction condition is calculated in the depleting formation layers.

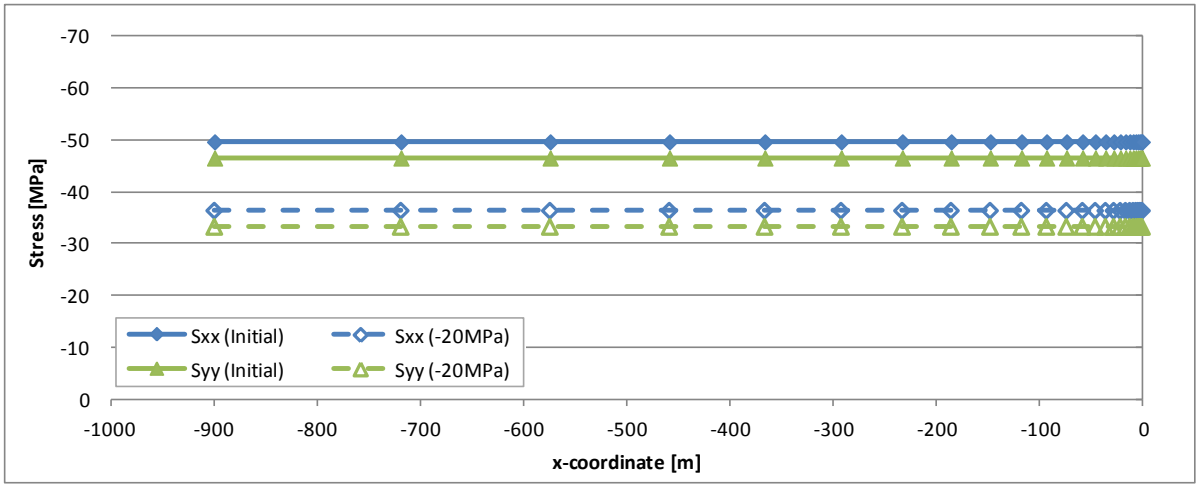

Figure A2.2 **The total horizontal stress distribution along a horizontal line at 2875 m depth for Case 1 under initial conditions and under a depletion of -20 MPa in formation Layer 3. In Case 1, S_{xx} is equal to the maximum horizontal stress and S_{yy} is equal to the minimum horizontal stress.**

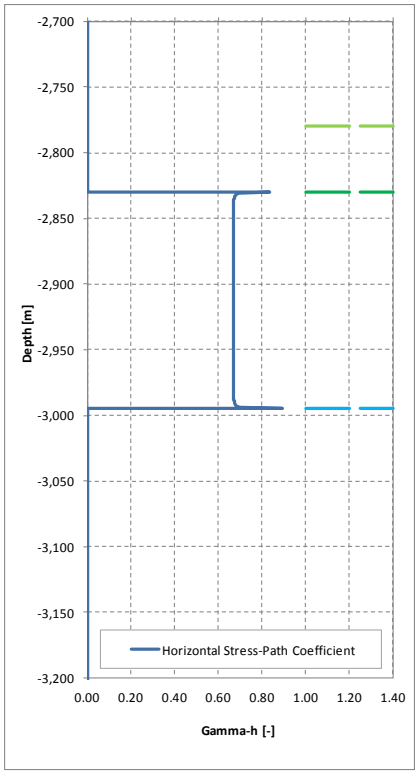

Figure A2.3 The horizontal stress-path coefficient derived from the fault total normal stress under initial and -20 MPa depletion conditions. Results are the same in the two horizontal directions and for cases 1 through 4.

A2.2. Stress condition along a dipping fault plane

The same runs from the previous section have been repeated for a fault dip angle of 75 degree with the horizontal as cases 11 through 14 (Table A2.6). All other model parameters have been kept the same and are given in Table A2.3. The pore pressure distribution is the same as for the vertical fault discussed in the previous section and is shown in Figure A2.1 (left-hand side).

Table A2.5: Fault and in-situ stress orientation in validation cases 11 through 14

Property	Unit	Case 11	Case 12	Case 13	Case 14
Fault dip angle	[deg]	75	75	75	75
Fault dip azimuth	[deg]	0	30	45	90
Max. Hor. stress azimuth	[deg]	0	0	0	0

A vertical shear stress component is present on the fault plane under initial stress conditions, because of the fault's dip angle (Figure A2.4). The normal and shear stress components can be derived analytically by transformation of the initial stress from the global XYZ-coordinate system in to a coordinate system that is aligned with the fault normal vector using the fault azimuth and dip [9].

The comparison between the analytical and model results are given in Table A2.7. The model results show an underestimation of the fault effective normal stress of 0.42% maximum, and an underestimate of the shear stress component of 0.52% maximum.

The analytical stress condition under depletion conditions is derived from the initial stress condition in Table A2.4 and the uniaxial stress-path coefficient γ_h according to equation 2.9. The total vertical stress is not changed due to depletion. The resulting stress condition is transformed into the fault coordinate system subsequently. The comparison between the analytical and model

results is given in Table A2.8. The model results show an underestimation of the fault effective normal and shear stress components of 0.4% maximum.

The right-hand side of Figure A2.4 shows the SCU distribution as function of depth under initial and depleted reservoir conditions. The SCU is the ratio between the actual shear stress τ and the shear stress carrying capacity τ_{max}. The SCU is 1 at the onset of failure [9].

For cases 11 through 14, the SCU has been calculated based on the normal and shear stress results given in Table A2.7 and Table A2.8 and using a Coulomb friction law for τ_{max}. For the current validation runs, the cohesion and friction angle has been set to the values used initially in the Groningen fault stability assessment [10]. That is, a cohesion of 7 MPa and a friction angle of 10 degree.

The initial SCU increases slightly with depth under the initial stress condition and shows a small jump from 0.29 to 0.32 between formation Layer 2 and 3. This is caused by the lower fault effective normal stress due to the gas column in the reservoir formation in Layer 3. The lower normal stress causes a lower τ_{max} and therefore a higher SCU. Furthermore, it is seen that the SCU increases almost uniformly over the formation layer as a result of reservoir depletion.

The model derived Shear Capacity Utilisation (SCU) underestimates of the analytical results by 0.41% maximum (Table A2.8). The deviation of the SCU is in the same order of magnitude as the normal and shear stress components, as could be expected. In most cases, no difference is noticed if the SCU is rounded to 2 decimal places.

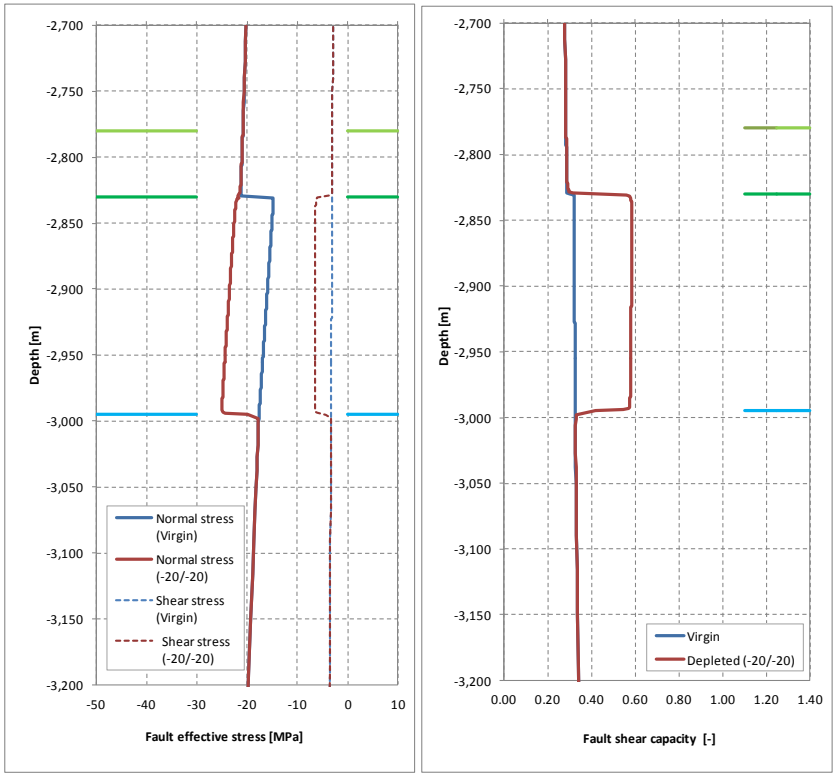

Figure A2.4 **Fault effective normal and shear stress distribution as a function of depth for Case 11 (left) and the Shear Capacity Utilisation (right).**

Table A2.6: **Analytical and model results for the fault effective normal and shear stress under initial stress conditions at a reference depth of 2875m TVD.**

Normal stress	Case 11	Case 12	Case 13	Case 14
Analytical [MPa]	-14.74	-14.09	-13.42	-12.07
Model [MPa]	-14.71	-14.04	-13.36	-12.02
Deviation	-0.4%	-0.4%	-0.4%	-0.4%

Shear stress				
Analytical [MPa]	-3.15	-3.33	-3.51	-3.88
Model [MPa]	-3.15	-3.33	-3.51	-3.88
Deviation	0.5%	0.5%	0.5%	0.4%

Table A2.7: Analytical and model results for the fault effective normal and shear stress under 20 MPa depletion conditions at a reference depth of 2875m TVD.

Normal stress	Case 11	Case 12	Case 13	Case 14
Analytical [MPa]	-22.32	-21.65	-20.98	-19.63
Model [MPa]	-22.25	-21.58	-20.90	-19.56
Deviation	-0.3%	-0.3%	-0.4%	-0.3%
Shear stress				
Analytical [MPa]	-6.49	-6.67	-6.85	-7.21
Model [MPa]	-6.46	-6.64	-6.82	-7.18
Deviation	0.4%	0.4%	0.4%	0.4%

Table A2.8: Analytical and model results for the Shear Capacity Utilisation (SCU) under initial and 20 MPa depletion conditions at a reference depth of 2875m TVD. A cohesion of 7 MPa and a friction angle of 10 degrees have been assumed.

virgin SCU	Case 11	Case 12	Case 13	Case 14
Analytical [MPa]	0.33	0.35	0.38	0.42
Model [MPa]	0.33	0.35	0.37	0.42
Deviation	-0.41%	-0.41%	-0.36%	-0.32%
Depletion SCU				
Analytical [MPa]	0.59	0.61	0.63	0.68
Model [MPa]	0.58	0.61	0.63	0.68
Deviation	-0.3%	-0.3%	-0.3%	-0.2%

Appendix 3. Impact of Young's modulus on Strain

A3.1. Formation stress and strain distribution

The vertical (compaction) strain is shown in Figure A3.1 as a function of the normalised horizontal coordinate. The vertical strain has been normalised for the uni-axial compaction strain according to equation 3.1 given in section 3.1. Table A3.1 gives the compaction strain values used for normalisation. It is found that the far-field vertical strain is proportional to the uni-axial compaction strain, and that it's distribution is not impacted by a uniform change of Young's modulus in all formations (Serie 1).

The vertical strain is disturbed in a zone around the fault smaller than 1 reservoir thickness. As found in Chapter 3, the vertical compaction strain does not increase after the onset of slip on one side of the fault at 19.9 MPa reservoir depletion. After 30 MPa depletion, the deviation from the uni-axial compaction strain is about 40% at the top and bottom of the reservoir formation. In the center of the reservoir formation, a reduction of less than 8% from the uni-axial compaction strain is found on both sides of the fault. This suggests that on average the vertical strain in the reservoir is smaller in the vicinity of the slipping fault compared to the (undisturbed) uni-axial compaction conditions. Furthermore, this implies that the energy dissipated by fault slip is at the expense of the energy storage in the reservoir strain and pressure components in the vicinity of the fault (section 3.1).

Table A3.1: Uni-axial compaction strain calculated using equation 3.1 for different values for Young's modulus under 30 MPa reservoir depletion

	Young's modulus		
	1 GPa	10 GPa	100 GPa
Vertical strain	$25.0 \cdot 10^{-3}$	$2.50 \cdot 10^{-3}$	$0.250 \cdot 10^{-3}$

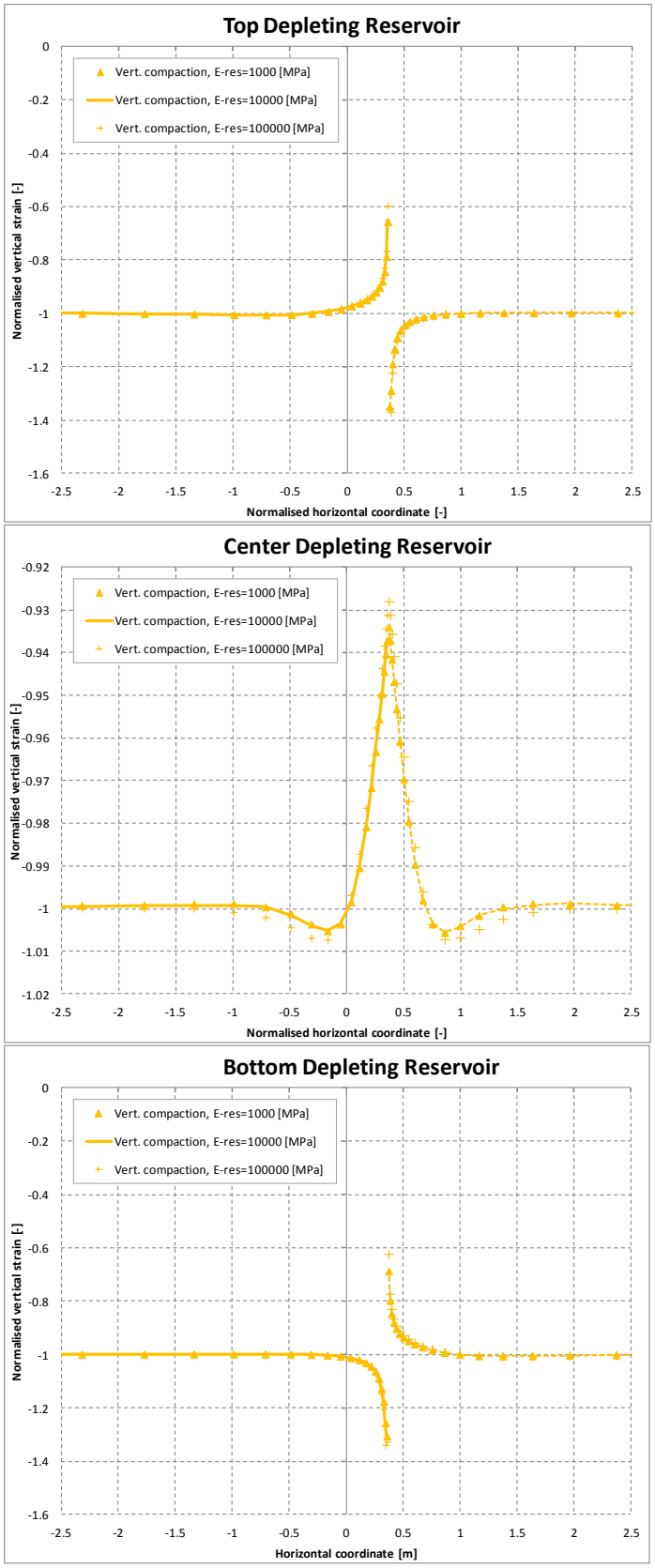

Figure A3.1: **Normalised vertical compaction strain as a function of the horizontal coordinate normalised for the reservoir thickness at the top, centre and bottom of the reservoir under 30 MPa reservoir depletion and for a uniform Young's modulus of 1, 10 and 100 GPa (Series 1). Negative values indicate compaction.**

Appendix 4. Results for 215m and 440m formation offset

This appendix contains similar results as presented in section 7.1 for a formation offset of 215m, which is equal to the thickness of the depleting reservoir formation, and for an offset of 440m, which is slightly more than twice that thickness.

Figure A4.1 shows the pore pressure distribution, the RSD, the effective normal and shear stress distribution and the SCU as a function of depth for an offset of 215m. In comparison with the case of 80 m offset discussed in section 7.1, it is seen that a larger part of the fault is exposed to reservoir depletion. Onset of fault slip starts after 3.6 MPa depletion at the bottom of the foot wall (right-hand side) and at the top of the hanging wall (left-hand side). This is recognised by the location where the SCU is equal to 1. The RSD distribution shows a peak value at the same location at the fault. The slip patch growths gradually with reservoir depletion, both upwards and downwards, under gradual increase of the maximum RSD.

Figure A4.2 shows the same results for an offset of 440m, about twice the reservoir thickness. Two parts of the fault are exposed to reservoir depletion, with equal length to the case of 215m offset. Onset of fault slip occurs after 7.0 MPa depletion at the bottom of the foot wall (right-hand side) and at the top of the hanging wall (left-hand side). This seen from the yellow line in the SCU distribution after 10 MPa depletion. The two slip patches grow upwards and downwards upon further depletion, until they merge after about 23 MPa reservoir depletion (see also section 7.2).

Furthermore, it is noted that the magnitude of the resultant shear stress changes sign at the most shallow point and at the deepest point of the fault that is exposed to reservoir depletion (Figure A4.1c and Figure A4.2c).

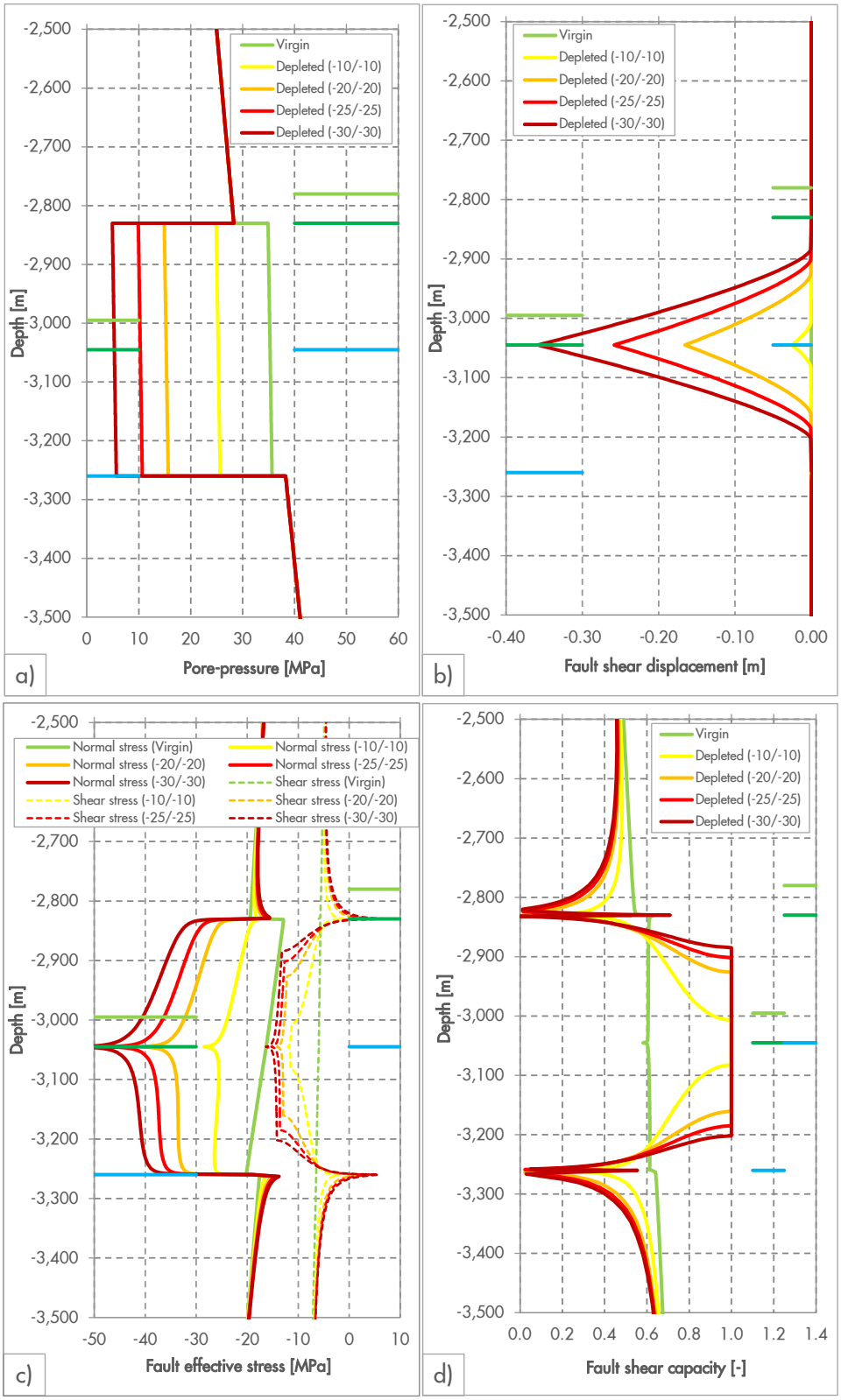

Figure A4.1: **a) Pore pressure, b) Relative Shear Displacement (RSD), c) Effective normal and shear stress, and d) the Shear Capacity Utilisation as a function of the depth for a throw of 215 meter, under virgin and 10, 20, 25 and 30 MPa depletion conditions**

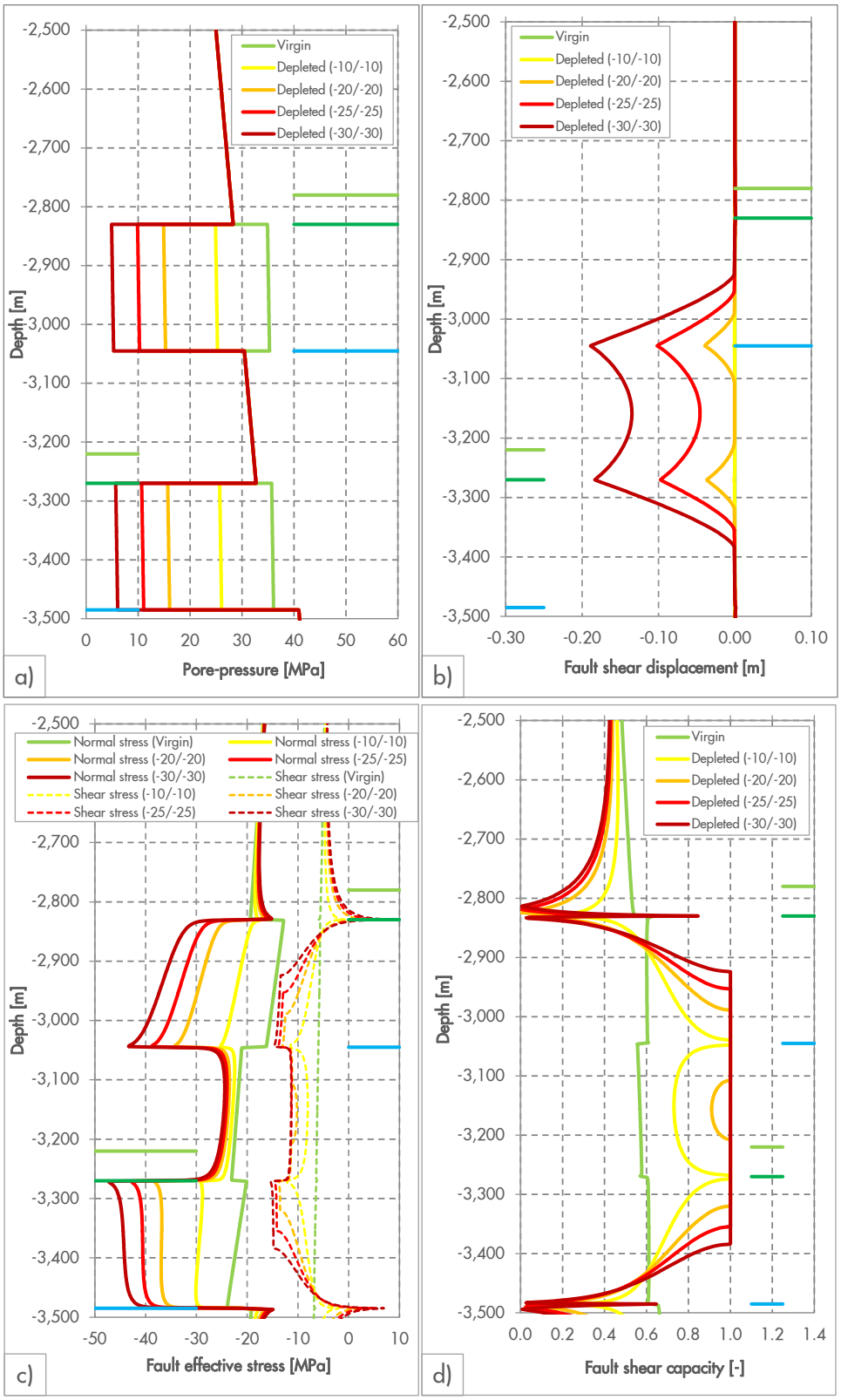

Figure A4.2: **a) Pore pressure, b) Relative Shear Displacement (RSD), c) Effective normal and shear stress, and d) the Shear Capacity Utilisation as a function of the depth for a throw of 440 meter, under virgin and 10, 20, 25 and 30 MPa depletion conditions**

Bibliographic information

Classification	Restricted
Report Number	SR.15.11455
Title	Impact of various modelling options on the onset of fault slip and fault slip response using 2-dimensional Finite-Element modelling
Author(s)	P.A.J. van den Bogert (GSNL-PTU/E/Q)
Keywords	Netherlands, Groningen, Fault Stability Phase 3, Fault slip, Mohr-Coulomb, Mohr-circle analysis, Energy-balance equation, Induced seismicity, Geomechanics, Finite-Element method, Groningen
Date of Issue	July 2014
Period of Work	July - December 2014
US Export Control	Non US - Non Controlled
WBSE Code	ZZPT/015656/010124
Approved by/Content owner	D. Doornhof (NAM-PTU/E/Q)
Sponsoring Company / Customer	NAM
Issuing Company	Shell Global Solutions International B.V., Rijswijk P.O. Box 60 2280 AB Rijswijk The Netherlands

Report distribution

Electronic distribution (PDF)

Name, Company, Ref. Ind.	*PDF*
PT Information Services, PTT/TIKE, PT-Information-Services@Shell.com	Word + PDF
van den Bogert, Peter AJ GSNL-PTU/E/Q	PDF
Doornhof, Dirk NAM-PTU/E/Q	PDF
van Elk, Jan F NAM-UIO/T/DL	PDF
van Eijs, Rob MHE NAM-PTU/E/Q	PDF
van der Wal, Onno NAM-PTU/E/Q	PDF
Visser, Clemens A NAM-UIO/T/DG	PDF
Mallik, Jyotirmoy NAM-PTU/E/F	PDF
van der Molen, Ide NAM-PTU/E/F	PDF
Solano Viota, Jose L NAM-UIO/T/DG	PDF
Romijn, Remco NAM-UIO/T/DL	PDF
Maron, Karel P NAM-UIO/T/DL	PDF
Wentinck, Rick M GSNL-PTI/RC	PDF
Bierman, Stijn M GSNL-PTD/TASE	PDF
Bourne, Stephen J GSNL-PTI/RC	PDF
Oates, Steve J GSNL-PTU/E/S	PDF
Droujinine, Alexander GSNL-PTI/ET	PDF
ten Kroode, Fons PE GSNL-PTI/ET	PDF
Davison, Mark M GSUK-PTU/E/Q	PDF
Yuan, Roger S GSNL-PTU/E/Q	PDF
Hertogh, Gerard MM GSNL-PTU/E/Q	PDF
Fokker, Peter A PTIN-PTU/E/Q	PDF
Hindriks, Kees OH GSNL-PTI/RC	PDF
Schutjens, Peter GSNL-PTU/E/Q	PDF
Kraaijeveld, Famke GSNL-PTI/RC	PDF
Cid Alfaro, Marcela V GSNL-PTI/RC	PDF
Mossop, Antony P GSNL-PTI/RC	PDF
de Borst, Karin GSNL-PTI/RC	PDF
De Vries, Sijtze SD PDO-USR4	PDF
Collins, Charles L SEPCO-UAD/T/T	PDF
Wong, Sau-Wai SIEP-PTI/U	PDF
Richard, Pascal D GSNL-PTU/E/R	PDF
Naruk, Steve J SIEP-PTI/EG	PDF
Tare, Uday A SIEP-PTU/E/Q	PDF

Van Der Weiden, Raphic M SIEP-PTU/E/Q	PDF
Guida, Assia NORSKE-PTU/E/Q	PDF